DESIGN AND SIMULATIONS OF RADIO-FREQUENCY QUADRUPOLE AND ACCELERATING CAVITIES FOR DEUTERON LINEAR ACCELERATOR

BY

JASON JIN

Submitted in partial fulfillment of the
requirements for the degree of
Master of Science in Physics
at the Illinois Institute of Technology

Approved _____
Adviser

Chicago, Illinois
May 2025

© Copyright by

JASON JIN

2025

ACKNOWLEDGMENT

My greatest thanks go to my research advisor Dr. Brahim Mustapha, whose work, guidance, and patience made this project possible. I also am deeply grateful for the tireless guidance of my IIT advisor Prof. Pavel Snopok for his expertise and assistance throughout the whole graduate school process. Much thanks to Dr. Yuri Batygin for his excellent USPAS class on linear accelerators and willingness to answer my inquiries about RFQ codes. Thanks as well to Romuald Duperrier and CEA DACM for their development of, documentation of, and permission to use the RFQ Designer and Toutatis codes. Finally, thanks to my mom and dad, my sister, and my friends for their unwavering support.

This work was funded through grant number DE-SC-0020379 of the Chicagoland Accelerator Science Traineeship, which is supported by the US Department of Energy, Office of Science, and Illinois Institute of Technology, Lewis College of Science and Letters.

AUTHORSHIP STATEMENT

I, Jason Jin, attest that the work in this thesis is substantially my own.

In accordance with the disciplinary norm of physics (see IIT Faculty Handbook, Appendix S), the following collaborations occurred in the thesis:

Dr. Brahim Mustapha from Argonne National Laboratory's Physics Division was the principal research advisor for this thesis. He provided the majority of guidance regarding the scope and content of this project.

Professor Pavel Snopok from the Illinois Institute of Technology's Department of Physics was also an advisor for this thesis. He provided the majority of administrative guidance regarding this document itself, in addition to some guidance on research questions.

TABLE OF CONTENTS

Page

ACKNOWLEDGMENT iii

AUTHORSHIP STATEMENT iv

LIST OF TABLES vii

LIST OF FIGURES viii

ABSTRACT xiii

CHAPTER

1. INTRODUCTION 1

2. RADIO-FREQUENCY QUADRUPOLE 2

2.1. Principles 2
2.2. Design software 6
2.3. RFQ beam simulations 13
2.4. Building the RFQ in CST 20
2.5. CST simulation 25
2.6. Comparison of CST field with Toutatis field 34

3. ACCELERATING SECTION 38

3.1. Half-wave resonator principles 38
3.2. Design software 39
3.3. Optimization of cavity geometry 40
3.4. Cavity beam simulations 47

4. CONCLUSION 53

APPENDIX 54

A. SCREENSHOTS OF TOUTATIS INTERFACES 54

B. VBA MACRO USED FOR GENERATION OF RFQ CELLS IN CST STUDIO 56

C. DETAILS OF RFQ MODELS FROM CST STUDIO SUITE . . 65

D. DETAIL OF CAVITY MODELS FROM CST STUDIO SUITE . 67

E. TRACK.DAT FILE FOR CAVITY ENERGY GAIN SIMULATION 74

F. BETA CURVES OF INDIVIDUAL CAVITIES 77
BIBLIOGRAPHY 82

LIST OF TABLES

Table Page

3.1 Optimization of Q factor and fine-tuning frequency for the low-β cavity using the geometric parameters RW, EWP, and IOR. The peak surface electric field, peak surface magnetic field, resonant frequency, and cavity Q are displayed as calculated by CST simulation. The final row shows the result of having achieved the resonant frequency to within 100 kHz while having recovered a significant amount of Q factor. 44

3.2 Fine-tuning the high-β cavity for the desired resonant frequency of 325 MHz. Also shown is the number of tetrahedrons used in the CST simulations for each set of geometric parameters. In this case the results were achieved by only changing the IOR, due to a favorable set of values of peak surface fields and Q factor to begin with. . . . 44

3.3 Table of energy gains for the first 20 cavities, comprising all the low- and medium-beta geometry cavities. The geometry switches at the point where the left and middle curves intersect in Figure 3.4. . . . 51

3.4 Table of energy gains for the next 21 cavities, comprising all of the high-beta geometry cavities. The geometry switches at the point where the middle and right curves intersect in Figure 3.4. 52

LIST OF FIGURES

Figure Page

2.1 The modulation period of the RFQ is $L = \beta \cdot \lambda$, shown here as measured along the z axis from two adjacent points where the horizontal vanetips' distance are minimal (corresponds to bottom-left of Figure 2.2). The quantity L should not be confused with the cell length, which is half of this ($\frac{L}{2}$). 4

2.2 Above: a cross-sectional view of the RFQ at the $z = 3491.838\,\text{mm}$ slice looking straight down the z axis, along with the instantaneous electric field arrows projected on the xy plane for when the horizontal vanetips have negative polarity and the vertical vanetips have positive polarity. Below: structure parameters for the RFQ at three different points along the RFQ—when the vertical vanetip distance is maximal ($z = z_0 - \frac{\beta\lambda}{4}$), when the vertical and horizontal vanetip distances are equal ($z = z_0$), and when the horizontal vanetip distance is maximal ($z = z_0 + \frac{\beta\lambda}{4}$). 7

2.3 The vanetips of a single RFQ cell, having length $\frac{L}{2} = \frac{\beta\lambda}{2}$. 8

2.4 The *Constraints* tab of RFQ Designer, as well as the *Results* panel. 11

2.5 The *Objectives* and *Simulation* tabs of RFQ Designer. 12

2.6 A screenshot of the starting interface in Toutatis. 14

2.7 A screenshot of the "RFQ Geometry" tab in Toutatis. 15

2.8 A screenshot of the "Beam" tab in Toutatis. 16

2.9 A screenshot of the simulation output in Toutatis. 16

2.10 A screenshot of the output graphic right-click and export menu in Toutatis. 17

2.11 A screenshot of the output graphics for x (upper) and y (lower) beam envelopes in Toutatis, with input parameters $\alpha_{x,y} = 0.5$ and $\beta_{x,y} = 3.0\,\text{cm/rad}$. In the plot of the beam's x envelope, the RFQ vanetip surface is also shown, in red. The vanetip surface is not depicted in the lower plot, which is at the same scale. The transmission within $\pm 2.5\%$ of 1.3 MeV was 91.90%. 18

2.12 The same plot as above, with the y scales of both plots magnified. Note the significant secondary oscillations, resulting from a mismatch of the beam's parameters to the RFQ's parameters at the entrance. 18

2.13 A screenshot of the output graphics for x (upper) and y (lower) beam envelopes in Toutatis, with input parameters $\alpha_{x,y} = 1.0$ and $\beta_{x,y} = 3.75\,\text{cm/rad}$. The transmission within $\pm 2.5\%$ of 1.3 MeV was improved to 94.20% over the parameter choice in Figure 2.11. . . . 19

2.14 The same plot as above, with the y scales of both plots magnified. Note the markedly decreased secondary oscillations, due to improved matching of the beam's parameters to the RFQ's parameters at the entrance. . . . 19

2.15 The CST interface in the *3D* tab (bottom left of main panel), showing in the in-progress generation of the RFQ cells by the VBA macro. 24

2.16 The RFQ vanes with a constant +37439 V on the vertical vanes and a constant −37439 V on the horizontal vanes. . . . 25

2.17 A close-up of the RFQ hexahedral mesh with a total of 6,602,770 meshcells. The hexahedral mesh produced a more uniform field than using a tetrahedral mesh. . . . 27

2.18 Subvolume of the RFQ inside of which the E-fields are exported. . 28

2.19 Constructing the cloverleaf resonator shape by subtracting (in red) four cylinders and a square prism from a square prism perfect conductor body (gray). The vanetips can then be attached to the middle of this resonator body. . . . 29

2.20 Equations for the cloverleaf geometry, describing connecting the straight vanetips with circular arcs, shown here for one "leaf." . . 30

2.21 The CST model of the cloverleaf resonator. . . . 30

2.22 Diagonal modes in the RFQ in the high-frequency simulation. These modes are undesired, and their presence in the simulation leads to a disordered field and a differently-shaped field profile than that produced by Toutatis. . . . 32

2.23 The desired RFQ mode, as achieved in the electrostatic simulation. 33

2.24 Cross-section of the breakout geometry. The red angle is known as the breakout angle as mentioned in Section 2.3. . . . 33

2.25 E_z on axis in Toutatis (dashed red) and the electrostatic CST simulation (solid green). . . . 35

2.26 E_z on axis in Toutatis and CST, for approximately the first 20 cells. The mismatch at the entrance is due to the CST model not having a radial matching section, and instead having simply a 90-degree cutoff. Compare the tapered entrance and exit vanes as seen in Figure 2.13 with the 90-degree edges as seen in Figure 2.16. 36

2.27 E_z on axis in Toutatis and CST, for approximately the last 20 cells. 36

2.28 Using a tetrahedral mesh resulted in a less ordered field profile than the hexahedral mesh (compare with Figure 2.26). 36

2.29 E_z on axis for the high-frequency simulation. 37

3.1 From left: the result of the rotation around the z axis of a list of points; the edges blended; the entire shape mirrored to create the pillbox. 40

3.2 From left: the spoke is created by lofting together the top and bottom circular openings with the racetrack-shaped aperture section; the entire spoke is subtracted from the pillbox; the single-spoke cavity is complete. 41

3.3 The beta curve of the first half of a two-gap cavity (red) compared with the beta curve of the entire two-gap cavity (green). The first half, containing a single RF gap, only has electric fields pointing in the same direction, while the entire cavity has its two halves opposite in phase (π mode). The result is that while a single gap will impart more energy to a particle the faster the particle travels, a two-gap cavity will have a speed at which the energy gain is maximal. . . . 42

3.4 Combined beta curves for the three geometries. The intersections of the low-beta (red circles) and medium-beta (green crosses) curves and the medium-beta and high-beta (blue squares) curves are the two places where the geometries switch in the accelerating section, so that the geometry used is always the one with the highest energy gain for that beta. 43

3.5 The peak surface electric field and resonant frequency for different values of certain parameters. The physical meanings of the parameters are depicted in the next two figures. 45

3.6 Some of the geometric parameters used in the optimization process: he spoke base radius (SBR), the spoke base height (SBH), the end wall position (EWP), the iris outer radius (IOR), and the racetrack thickness (RT). 46

3.7 One of the geometric parameters used in the optimization process, the racetrack width (RW). 46

3.8 Exporting a subvolume of the cavity for TRACK simulation, shown with the medium-beta cavity. 50

A.1 A screenshot of the "Simulation" tab in Toutatis. 55

A.2 A screenshot of the "Cells" tab in Toutatis. 55

C.1 Top: full RFQ 3D model in the electrostatic solver. Bottom: energy density near the exit. The peak energy density on the RFQ is $6271.23\,\mathrm{J/m^3}$. 66

D.1 Detail of low-beta cavity in CST. Top-left: 274,632 tetrahedrons mesh. Top-right: Peak surface currents, occurring at $\frac{n\pi}{2}$ phase. The resonant frequency is 325.047 MHz and the maximum surface current on the cavity is 48 kA/m (red, near the top and bottom). Bottom-left: yz plane cutaway showing the peak electric fields, occurring at $n\pi$ phase. Bottom-right: yz plane cutaway showing the peak H-fields, occurring at $\frac{n\pi}{2}$ phase. 68

D.2 Low-beta cavity close-up of electric (top) and magnetic (bottom) fields at peaks on yz plane. The maximum electric field on the cavity is 31.5 MV/m and the maximum H-field on the cavity is 48 kA/m, corresponding to the maximum surface current. Both the maximum electric and maximum magnetic fields occur outside of the depicted cutaway plane. 69

D.3 Detail of medium-beta cavity in CST. Top-left: 254,633 tetrahedrons mesh. Top-right: Peak surface currents, occurring at $\frac{n\pi}{2}$ phase. The resonant frequency is 321.11 MHz and the maximum surface current on the cavity is 25 kA/m (red, near the top and bottom). Bottom-left: yz plane cutaway showing the peak electric fields, occurring at $n\pi$ phase. Bottom-right: yz plane cutaway showing the peak H-fields, occurring at $\frac{n\pi}{2}$ phase. 70

D.4 Medium-beta cavity close-up of electric fields at peaks on yz plane. The maximum electric field on the cavity is 20.4 MV/m (occurs outside of the depicted plane). 71

D.5 Detail of high-beta cavity in CST. Top-left: 297,360 tetrahedrons mesh. Top-right: Peak surface currents, occurring at $\frac{n\pi}{2}$ phase. The resonant frequency is 325.052 MHz and the maximum surface current on the cavity is 21 kA/m (red, near the top and bottom). Bottom-left: yz plane cutaway showing the peak electric fields, occurring at $n\pi$ phase. Bottom-right: yz plane cutaway showing the peak H-fields, occurring at $\frac{n\pi}{2}$ phase. 72

D.6 High-beta cavity close-up of electric fields at peaks on yz plane. The maximum electric field on the cavity is 17.0 MV/m (occurs outside of the depicted plane). 73

D.7 Electric fields on the xy plane at phase zero in the high-frequency simulation (at 165.644 MHz) at cells near the exit. 73

F.1 Beta curve for the first half of a single-spoke cavity. It can be seen that any increase in the particle's incoming speed, above a certain point, will always result in a greater energy gain from the cavity. . 78

F.2 Beta curve for the low-beta cavity, the first geometry of cavity in the accelerating section. The peak efficiency is around $\beta = 0.094$. . 79

F.3 Beta curve for the medium-beta cavity, the second geometry of cavity in the accelerating section. The peak efficiency is around $\beta = 0.145$. 80

F.4 Beta curve for the high-beta cavity, the third and final geometry of cavity in the accelerating section. The peak efficiency is around $\beta = 0.189$. 81

ABSTRACT

A design for an RFQ capable of bunching and accelerating an incoming beam of 20 keV/u deuterons to 1.3 MeV/u was generated using the CEA software RFQ Designer, and beam simulations were carried out using the CEA software Toutatis. The RFQ design was verified using the electrostatic solver of CST Studio Suite. To further accelerate the bunches to 20 MeV/u, three different geometries of accelerating cavities were modeled in CST and optimized using the high-frequency solver. The energy gain of the cavities was simulated using the Argonne National Lab code TRACK.

CHAPTER 1

INTRODUCTION

Particle accelerators, for decades, have had countless wide-ranging applications in science and technology. In particular, linear accelerators, or linacs, have uses from studying subatomic physics to materials science to providing medical therapies. A linear accelerator generally refers to any particle accelerator where the particles pass through each component only once, and in theory any charged particle, from electrons to protons to heavier ions, can be accelerated through a linac. The demand for deuteron ($^2_1H^+$) beams is evident for producing particles as light as neutrons for materials research of fusion reactor components [1], to as heavy as nuclides with mass number over a hundred for medical radionuclide research [2]. A multi-purpose, variable-energy proton and deuteron linac design has been described for plans at the Soreq Applied Research Accelerator Facility (SARAF) [3], using radio-frequency quadrupole (RFQ) and superconducting cavity acceleration. The incoming beam emittance and current for the project described in this thesis were based on the beam characteristics of the SARAF design, since they were representative of a well-described design using an RFQ and superconducting cavities. The purpose of this project was to demonstrate a working design of a linac for deuterons, which have the challenge of having a charge-mass ratio of $\frac{1}{2}$, making the required force to accelerate them twice as much as for protons and much more than as for electrons. Also, this project aims to bridge the gap between simulations and modeling: oftentimes when simulating accelerators, the components are abstracted into numbers or code, to the point where it is hard to visualize what is happening in a physical sense. On the other hand, some of the tools designed for creating life-like models of accelerator equipment may not be well-suited for running precise beam simulations. Thus, my goal was to use multiple pieces of software to faithfully produce both simulations and models of accelerator components.

CHAPTER 2

RADIO-FREQUENCY QUADRUPOLE

2.1 Principles

We consider a low-energy continuous beam of charged particles, which we would like to turn into a high-energy beam that is bunched without increasing the beam size too much. In essence, we need to perform three tasks on the beam: longitudinal acceleration, longitudinal bunching, and transverse focusing. The radio-frequency quadrupole (RFQ) is able to do all three simultaneously, increasing the space- and cost-efficiency of the accelerator as a whole compared to using dedicated components for each task.

The RFQ is a combination of radio-frequency (RF) accelerating cavities with electric field transverse focusing. RF accelerating cavities can bunch and/or accelerate a beam, but the beam's transverse emittance will grow. Transverse-focusing beam elements like magnetic quadrupoles serve to maintain the beam's emittance, but impart to the beam no kinetic energy. By combining transverse focusing with RF acceleration, the RFQ can increase the beam energy while at the same time keeping its transverse parameters in check.

As a convention, let us assume the beam travels in the positive z direction, and the beam enters and exits the RFQ along the z axis, i.e. the design trajectory of a straight-line linac. The RFQ consists of a long (in the z direction), conducting resonator that is essentially mirror-symmetric about the xz plane and the yz plane. Its interior structure varies sinusoidally along the z axis (Figure 2.1). In a "four-vane," "vane-like," "vane-type," etc. RFQ, four vanes protruding from the wall of the resonator from each of the $\pm x$ and $\pm y$ directions inward toward the z axis have the distance between their tips and the z axis modulated along the z axis. In a

"four-rod," "rod-like," "rod-type," etc. RFQ, four conducting rods, with their long axis parallel to the z axis, placed some distance from the z axis in the $\pm x$ and $\pm y$ directions instead have their diameters modulated along the axis, so that the distances between the z axis and the surfaces of the rods vary sinusoidally along the z axis.

Let us consider the vane-type RFQ in more detail. The geometry of the vanetips is determined by the solution of Laplace's equation [4],

$$\frac{\partial^2 V}{\partial r^2} + \frac{1}{r}\frac{\partial V}{\partial r} + \frac{1}{r^2}\frac{\partial^2 V}{\partial \theta^2} + \frac{\partial^2 V}{\partial z^2} = 0 \tag{2.1}$$

in cylindrical coordinates, with the RF-varying electric potential being

$$U(r, \theta, z, t) = V(r, \theta, z) \cdot \sin(\omega \cdot t + \phi), \tag{2.2}$$

where ω is 2π times the RF frequency and ϕ is the initial phase of the potential. For our boundary conditions, we require that the time-independent potential V be mirror-symmetric in both the x and y directions,

$$V(r, \theta, z) = V(r, -\theta, z) = V(r, \pi - \theta, z),$$

and that the time-independent potential V at some location on a vanetip be exactly equal in magnitude and opposite in sign to the time-independent potential V on the orthogonal vane at the location one half-longitudinal-modulation away and the same distance from the z axis, i.e.

$$V(r, \theta, z) = -V\left(r, \theta + \frac{\pi}{2}, z + \frac{L}{2}\right),$$

where $L = \beta \cdot \lambda$ is the length of one full modulation in vanetip distance and is equal to the relativistic beta multiplied by the RF wavelength in free space, as seen in Figure 2.1.

We consider two types of solutions: one type that is independent of z, i.e. the two-dimensional solutions, which represent the cross-sectional (with respect to the z

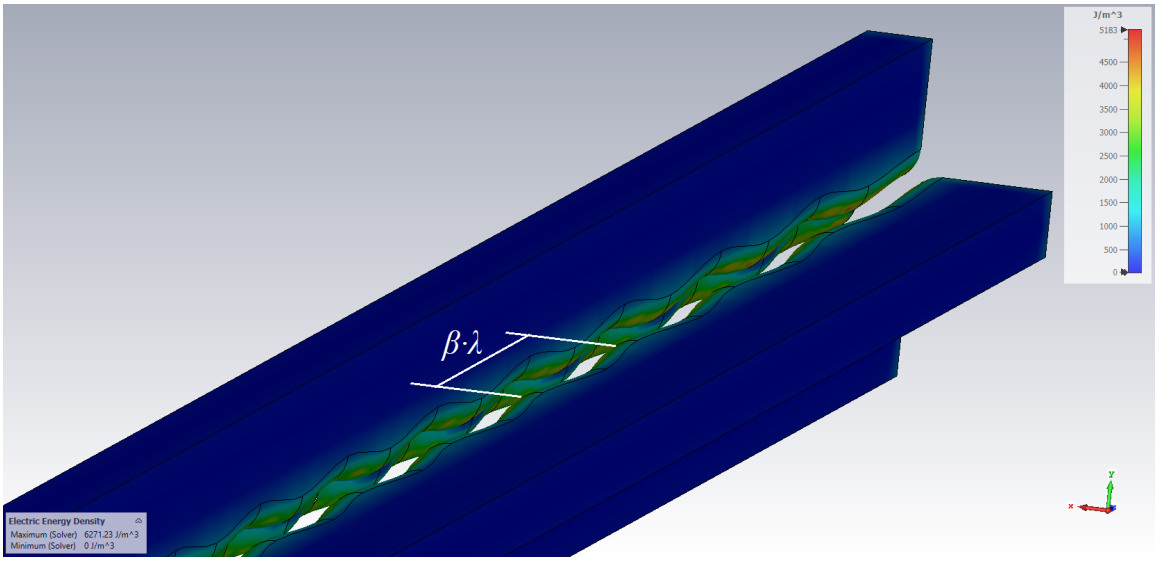

Figure 2.1. The modulation period of the RFQ is $L = \beta \cdot \lambda$, shown here as measured along the z axis from two adjacent points where the horizontal vanetips' distance are minimal (corresponds to bottom-left of Figure 2.2). The quantity L should not be confused with the cell length, which is half of this ($\frac{L}{2}$).

axis) field characteristics, and the other type that does depend on z, i.e. the three-dimensional solutions, which represent the axial modulation of the vanetips. By way of separation of variables, we obtain the general solution:

$$V(r,\theta,z) = \sum_{s=0}^{\infty} A_s r^{2(2s+1)} \cos\left[2\left(2s+1\right)\theta\right] + \sum_{n=1}^{\infty}\sum_{s=0}^{\infty} A_{n,s} I_{2s}(knr) \cos\left(2s\theta\right) \sin\left(knz\right), \tag{2.3}$$

where $k = \frac{2\pi}{L} = \frac{2\pi}{\beta\lambda}$. Equation (2.3) is referred to as the general K-T potential function, after the inventors of the first RFQ in 1969, Kapchinski and Teplyakov [5]. Here, I_a denotes the ath hyperbolic or modified Bessel function of the first kind. In terms of J_a (Bessel functions of the first kind), $I_a(x) = i^{-a} J_a(ix)$.

This general solution, the K-T function, is fairly involved, and, from first glance, constructing a 3D resonator that would produce this field seems difficult or impractical. However, the resonator geometry can be simplified greatly by considering solely a few terms from the general solution and then building the geometry so that the surfaces of the electrodes, i.e., the vanes or rods, conform to the resultant equipotential

surfaces. Let us choose the pure quadrupole term i.e. $s = 0$ from the first summation term and the monopole term i.e. $(s = 0,\, n = 1)$ from the second summation term from the general solution:

$$V(r, \theta, z) = A_0 r^2 \cos(2\theta) + A_{1,0} I_0(kr) \cos(kz). \tag{2.4}$$

This is called the "two-term potential function."

An RFQ can be described cell-by-cell using the parameters of modulation, vanetip radius, aperture radius, and cell length. The RFQ "cell" is defined as one half-period of undulation along the z axis, and thus has length $\frac{L}{2}$, as shown in Figure 2.3. We define the above quantities as follows. Let the $\pm x$ direction, where $\theta = 0, \pi$, be defined as horizontal. Assume the horizontal vanetips' distance to the z axis is at a local minimum at $z = z_0 - \frac{\beta\lambda}{4}$, and let their distance be a, as in Figure 2.2. Then, let the vertical vanetips at the same z location, whose distances to the z axis are at a local maximum, have distance $m \cdot a$ from the z axis. In a similar line of reasoning, the vertical vanetips' distance from the z axis will be at a local minimum at $z = z_0 + \frac{\beta\lambda}{4}$, and all four vanetips' distances from the z axis will be the same, and equal to $r0$, at $z = z_0$. We define m as the "modulation factor" and a as the "minimal aperture distance." These values vary along the z axis from cell to cell, for instance the modulation factor being close to 1 near the entrance and increasing to around 2 or higher at the exit. We define r_0 as the average aperture radius, and ρ as the vanetip radius. It can be imposed on the geometry that the vanetip radius ρ be constant along the entire RFQ, which would simplify the geometry at the cost of a possibly slightly sub-optimal efficiency. It could also be imposed that the average aperture radius r_0 be kept constant throughout the RFQ. The trade-offs between closeness to ideal geometry and simplicity or practicality of construction must always be considered when designing RFQs. As explained in section 2.2, the consideration of these trade-offs resulted in applying some of these constraints while discarding others;

for instance, the vanetip radius in the RFQ design for this project was kept constant, but the average aperture radius was allowed to vary.

2.2 Design software

Many codes exist that are capable of generating RFQ designs. One of the first and most widely-used codes is called PARMTEQ, developed in 1987 at Los Alamos National Lab [6]. More recent codes include DesRFQ, developed at the Institute for Theoretical and Experimental Physics, Moscow [7] and DemirciPro, developed in collaboration with personnel from Ankara University, University of California, Irvine, and other institutions [8]. Finally, RFQ Designer is a code developed at CEA DACM, that can design and optimize RFQs [9], and this code was chosen for use in this project due to other codes not being accessible at the time of the project or not functioning on modern operating systems.

The RFQ Designer program was developed with the goal in mind of allowing a user to generate an RFQ design that achieves a set of desired objective parameters, such as beam exit energy, total RFQ length, peak surface electric field, etc., by calculating the required forces for this predetermined behavior. This direct approach to solving is in contrast to some other RFQ design programs that instead accept a set of design parameters and merely inform the user about the achieved statistics at the end of a simulation. In this sense, RFQ Designer has the characteristic of being able to "reverse-engineer" an RFQ based on a set of desired performance goals, using weighted, multi-parameter optimizations with a comprehensive list of objectives and inputs.

RFQ Designer has three sections that the user interfaces with (Figures 2.4 and 2.5). These are the constraints, objectives, and simulation sections. The first section, the *Constraints* tab, is used to define a set of parameters that are fixed

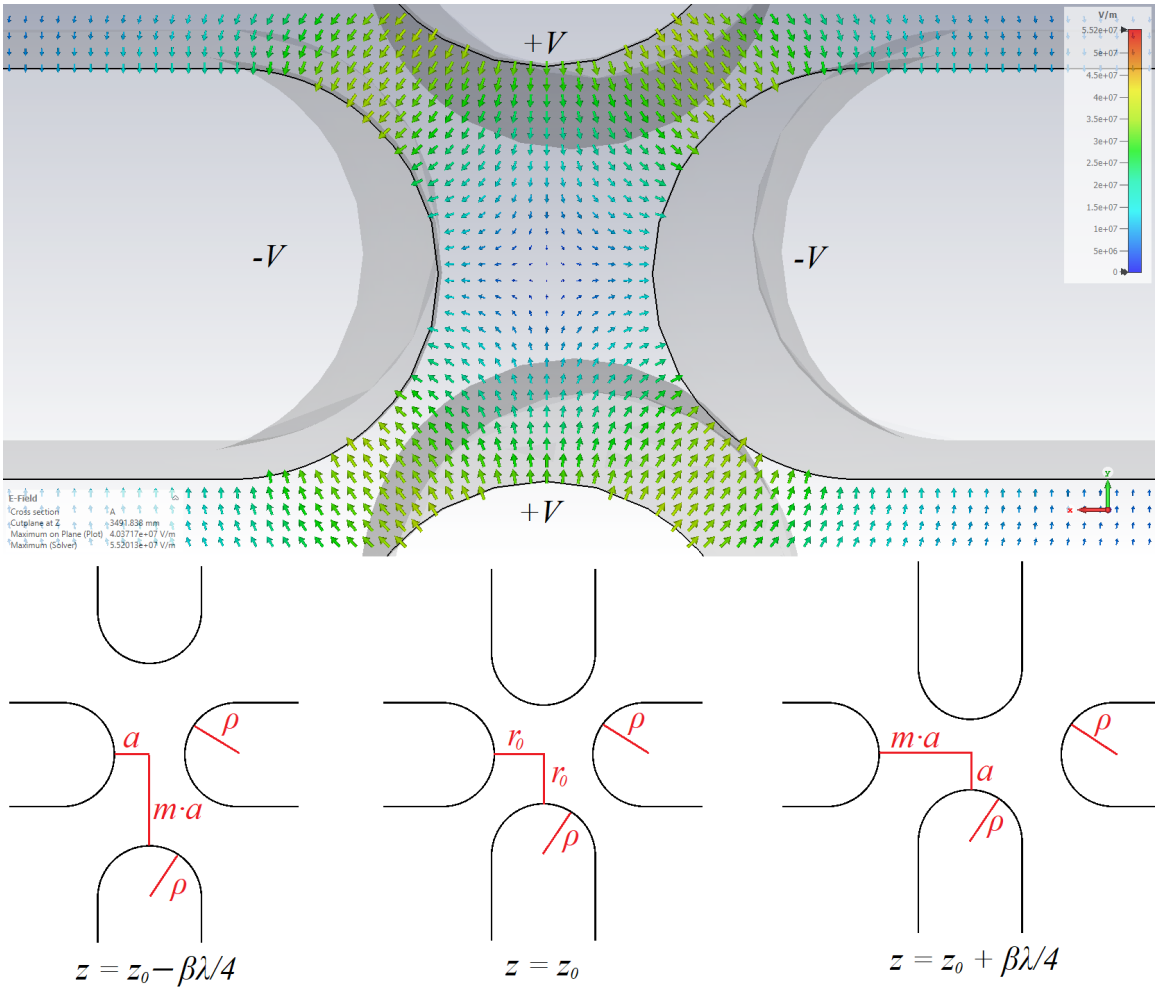

Figure 2.2. Above: a cross-sectional view of the RFQ at the $z = 3491.838\,\text{mm}$ slice looking straight down the z axis, along with the instantaneous electric field arrows projected on the xy plane for when the horizontal vanetips have negative polarity and the vertical vanetips have positive polarity. Below: structure parameters for the RFQ at three different points along the RFQ—when the vertical vanetip distance is maximal ($z = z_0 - \frac{\beta\lambda}{4}$), when the vertical and horizontal vanetip distances are equal ($z = z_0$), and when the horizontal vanetip distance is maximal ($z = z_0 + \frac{\beta\lambda}{4}$).

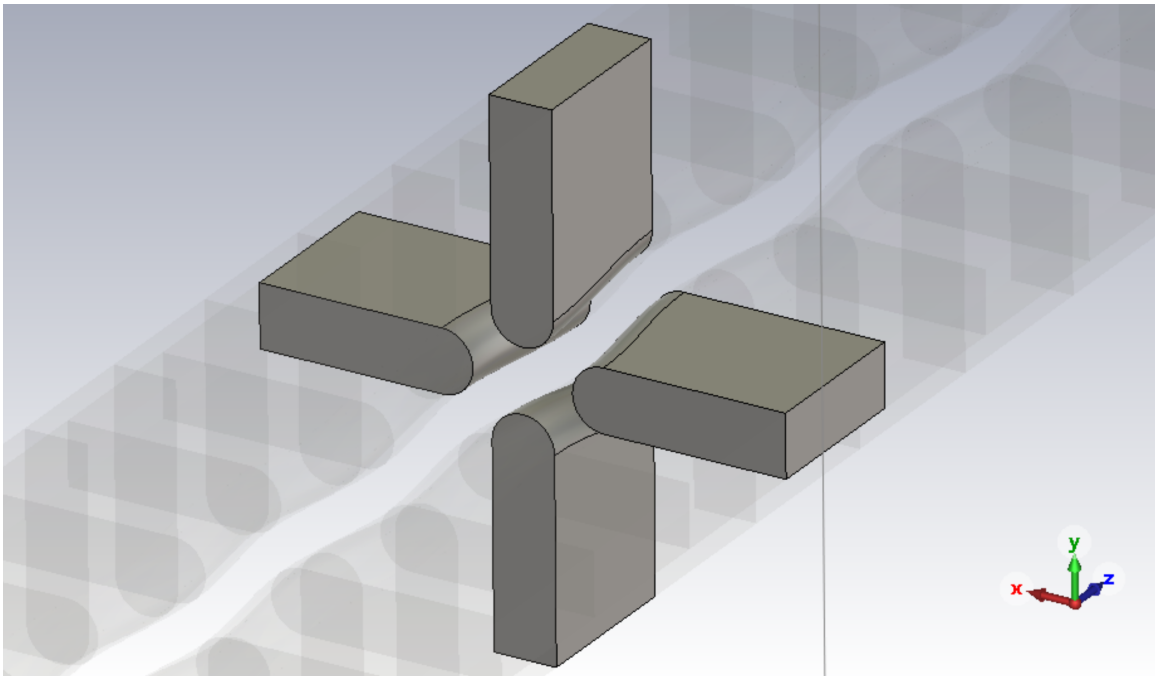

Figure 2.3. The vanetips of a single RFQ cell, having length $\frac{L}{2} = \frac{\beta\lambda}{2}$.

throughout the design process. These include input energy, resonant frequency, particle charge and mass, and characteristics such as whether the RFQ is superconducting or normal conducting, whether the vanetip radius is kept constant, whether the RFQ is rod-type or vane-type, and other such options. For my purposes, the most important quantities are the resonant frequency (162.5 MHz), particle type (deuteron), input current (5 mA), and maximum modulation (2.0). For simplicity of geometry and construction cost reduction, I also opted to keep constant the voltage across the entire RFQ and the vanetip radius (ρ). For the same reasons, I additionally enforced the constraints that the RFQ be normal conducting, have an expressly sinusoidal modulation of the vanetip surfaces along the z axis, and be a vane-type RFQ. A strictly sinusoidal modulation is contrasted with a so-called "2 terms" modulation that includes more terms of the cylindrical harmonics so as to more closely follow the ideal geometry [9]. In this sense, the sinusoidal modulation is akin to a "one-term" modulation function. I opted for a sinusoidal modulation in order to greatly simplify

the geometry so that it can be more easily modeled in a different software. In our case, enforcing a strictly sinusoidal modulation ended up not making any difference whatsoever, since the exact same cells were generated whether or not the "2 terms" modulation was used or not. This indicates that the cells that were generated were optimal for both a sinusoidal and "2 terms" modulation. It should also be noted here that though the vanetips are characterized by a radius, they are actually hyperbolically shaped in the ideal geometry; however in real-life RFQs, the vanetip geometry may deviate slightly from the ideal geometry with only small deviations from the desired field, for the purposes of simplifying the fabrication process and reducing the peak surface fields [4]. Though I kept the vanetip radius constant throughout the RFQ, I allowed the average aperture radius r_0 to vary, because keeping it constant would be too restrictive a constraint and would generate a suboptimal design with little appreciable simplification in the geometry.

The center panel of the *Constraints* tab contains an *Objectives monitor* plot, which shows how close the resultant objectives are to the goals. For quantities like length, power, and peak surface fields, these numbers should be smaller than the goals, and for the desired energy, the amount should be as close to the goal as possible. The central plot in Figure 2.4 has numerous superimposed plots, describing various RFQ parameters as they evolve through the length of the axis. They are: the minimum aperture radius a, shown in solid blue; the average aperture radius r_0, shown in solid red; the vanetip radius ρ, which is set as a constant and shown in solid yellow; the bunch energy W_s, shown in dashed magenta; the modulation factor m, shown in solid green; the peak surface electric field in Kilpatrick units, shown in dashed green; the synchronous phase Φ_s which characterizes how much of the RFQ is accelerating versus bunching, shown in solid magenta; and RFQ-specific factors A and B, which, respectively, score the longitudinal strength (similar to a geometrical shunt impedance), and the transverse strength (for when there is no longitudinal

component), shown respectively as dashed red and dashed blue [9]. Worth noting are some features of the plots of certain quantities. The average aperture radius r_0 decreases to a minimum near the middle cells, then increases slightly. This means that the transverse quadrupole focusing is strongest in the middle, where the vanetips are on average closer together, since a smaller distance with the same intervane voltage will produce stronger fields. The beam energy W_s increases very slowly until the later cells, where it has the highest increase per cell. This means that much of the first part of the RFQ is dedicated to the bunching of the beam, whereas the later part is used for acceleration mostly. This is also reflected in the synchronous phase Φ_s curve. The modulation factor m increases in general along the RFQ, but not monotonically; it decreases slightly for a part in the middle of the RFQ. Although it is not obvious why this behavior manifests in the optimization, it did not preclude a high-transmission RFQ design from being generated. The surface electric fields (dashed green *KP* curve measured in Kilpatrick units in Figure 2.4) are lowest at the entrance and highest in the middle, where the small average aperture radius, local modulation factor minimum, and shorter cell length compared to the end cells combine to produce the highest surface fields.

The second section of the RFQ Designer program's user interface is the *Objectives* tab. In this section the user can set targets for the program to optimize towards. The objective parameters are either beam-related (output emittance, transverse emittance growth, transmission, beam power losses, output energy) or cavity-related (maximum surface electric field, cavity length, peak dissipated RF power, life cycle cost). For each objective, the user can have the program aim for it to be below a certain value (ceiling), above a certain value (floor), maximized, minimized, or as close to a certain value as possible (exact). For each objective, the user can set a weight that determines how important that particular value is to optimize. Based on the optimization method, the weight, the target value, and the resultant value,

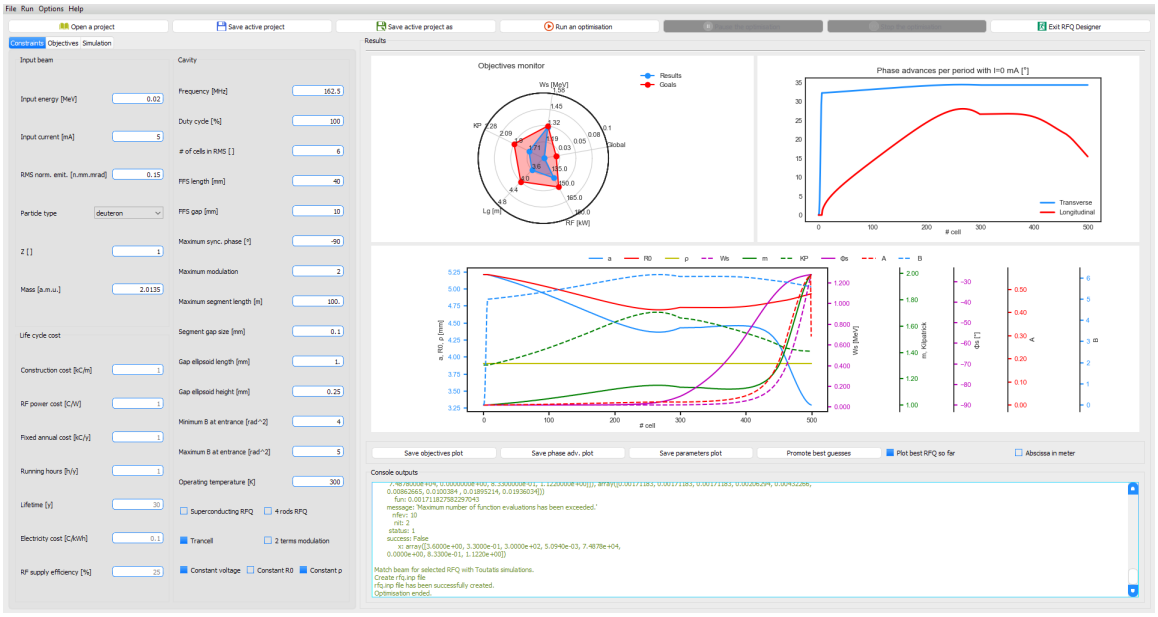

Figure 2.4. The *Constraints* tab of RFQ Designer, as well as the *Results* panel.

the program will output a certain objective optimization value, the sum of which the program will attempt to minimize across all targets.

In the third section, the *Simulation* tab, the user can input first guesses for several RFQ parameters: the average aperture radius at the entrance R_0; the intervane voltage; the difference in intervane voltage from one end of the RFQ to the other, if any; the bunching factor, which is defined as 0 if the beam remains unbunched and 1 if each bunch has infinitesimal longitudinal size; the number of cells to be used for bunching; the total RFQ length; the ratio of the vanetip radius ρ and R_0; and a coefficient for increasing or decreasing the steepness of the modulation factor growth, denoted A.

The *Results* panel shows updates on the optimization progress. Three plots are displayed here. The *Objectives monitor* plot shows how close each optimization variable is to its goal as well as the total objective function. Another plot shows the phase advance in the transverse and longitudinal directions along the RFQ. The third

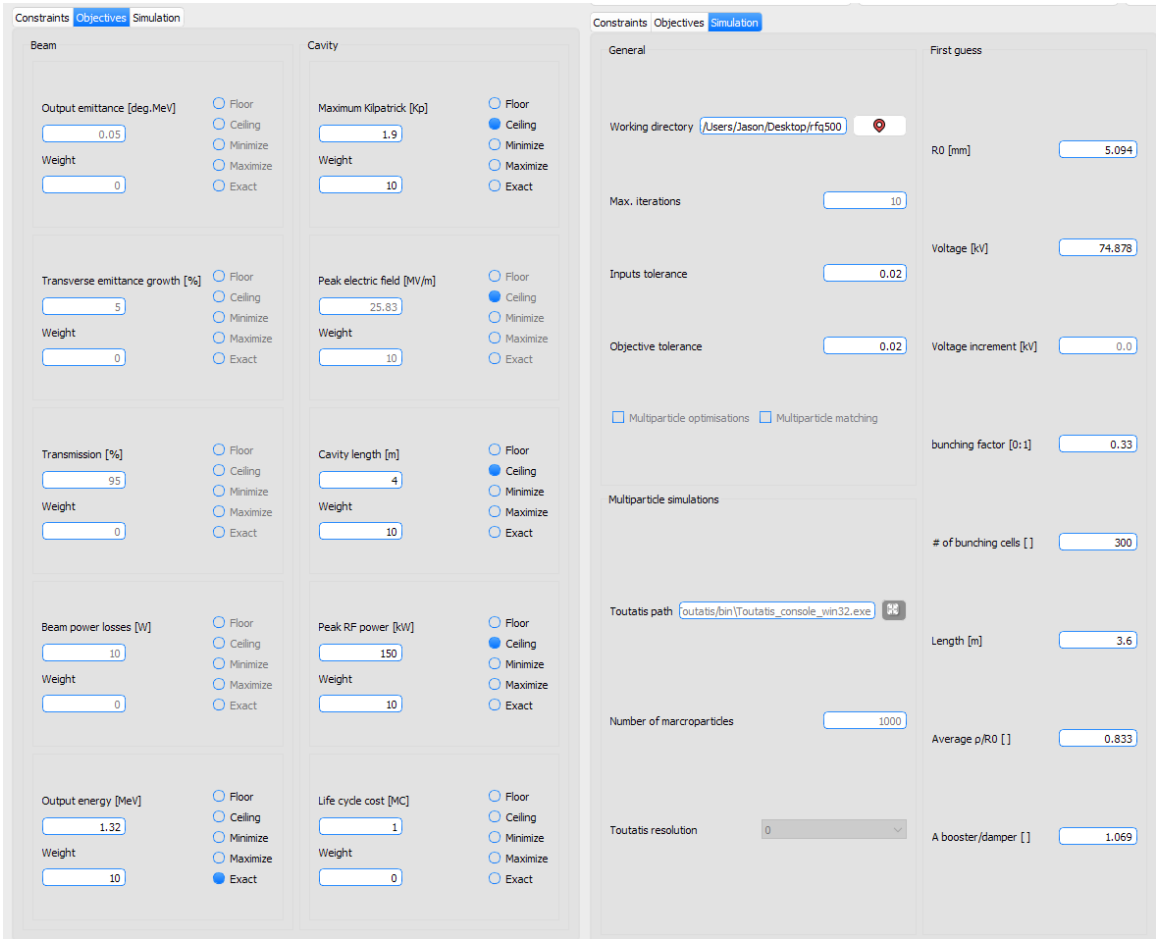

Figure 2.5. The *Objectives* and *Simulation* tabs of RFQ Designer.

plot shows various RFQ parameters along the RFQ. A useful tool in this monitor is the *Plot best RFQ so far* checkbox, which will keep the plots updated according to the RFQ with the best objective function in the optimization.

The optimization may fail to produce an RFQ geometry if the first guesses are too far from describing a physically valid model. Thus, it is productive to enter judicious first guesses. A method to increase the chance of success of producing a viable iteration is to start with the default values given by RFQ Designer when starting the program, and changing the constraints little by little in the direction of the desired constraints. For example, the default RFQ Designer frequency is 88.0525 MHz, so for each optimization run I increased this by a few percent until it reached 162.5 MHz. After each optimization run, the best guesses should be promoted, and the constraints further adjusted. Using this process, the software generated a 500-cell RFQ with high transmission (94.20% transmission within ±2.5% of the goal energy 1.3 MeV). Key parameters of the generated design are an average aperture radius r_0 of 5.094 mm, an intervane voltage of 74878 V, a total length of 3.6 m, and a constant vanetip radius ρ of 0.39 cm.

2.3 RFQ beam simulations

Beam simulations were performed in the Toutatis software, a trial version of which is provided by CEA [10, 11]. RFQ Designer was designed to be used in tandem with Toutatis, which is able to use RFQ Designer project output files as inputs to perform beam simulations on.

Upon launching the software, the first interface that appears allows us to set the working directory and open a project (Figure 2.6). After selecting the *.inp* file generated by the RFQ Designer software, we are now able to run the simulation or edit the input file. In the *Edit input file* interface (the second button from the left as seen

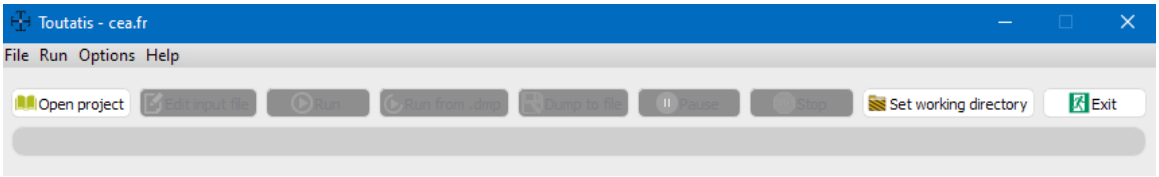

Figure 2.6. A screenshot of the starting interface in Toutatis.

in Figure 2.6, which will be un-grayed upon opening a project), there are four tabs of interest. In the first tab, *Simulation*, the user can adjust the simulation resolution, the filter settings, and the output settings (Figure A.1). Of particular interest to us is the energy filter setting, which I adjust to 0.0325 MeV to collect statistics about particles within 2.5% of the target energy (1.3 MeV). We can also request the software to produce an output file containing electric field values in a 3D grid along the RFQ. This is useful for comparing the Toutatis simulation to a simulation in CST Studio Suite (CST) or possibly other codes. The 3D grid parameters can be adjusted in the *Outputs* section. In our case, I requested a transverse size of 2 by 2 mm with a transverse density of 25 points in each direction, i.e. a grid point every 0.08 mm in the x and y directions, centered on the axis and including the origin. The longitudinal density is automatically set by the Toutatis software, and in our case the longitudinal grid resolution is 1.07 mm.

The second tab, *RFQ geometry* (Figure 2.7), contains information about the cell and vane geometries and a setting for the frequency, which was set at 162.5 MHz, inherited from the RFQ Designer output. We note that the *Breakout angle* is set to 15.0 degrees by default. This is a parameter used in a breakout-type RFQ geometry (Figure 2.24), as opposed to a cloverleaf-type geometry (Figures 2.19, 2.20, 2.21), which does not have this parameter. In Section 2.4 I discuss modeling these geometries in CST.

The *Cells* tab contains cell-by-cell parameters of the RFQ (Figure A.2). This

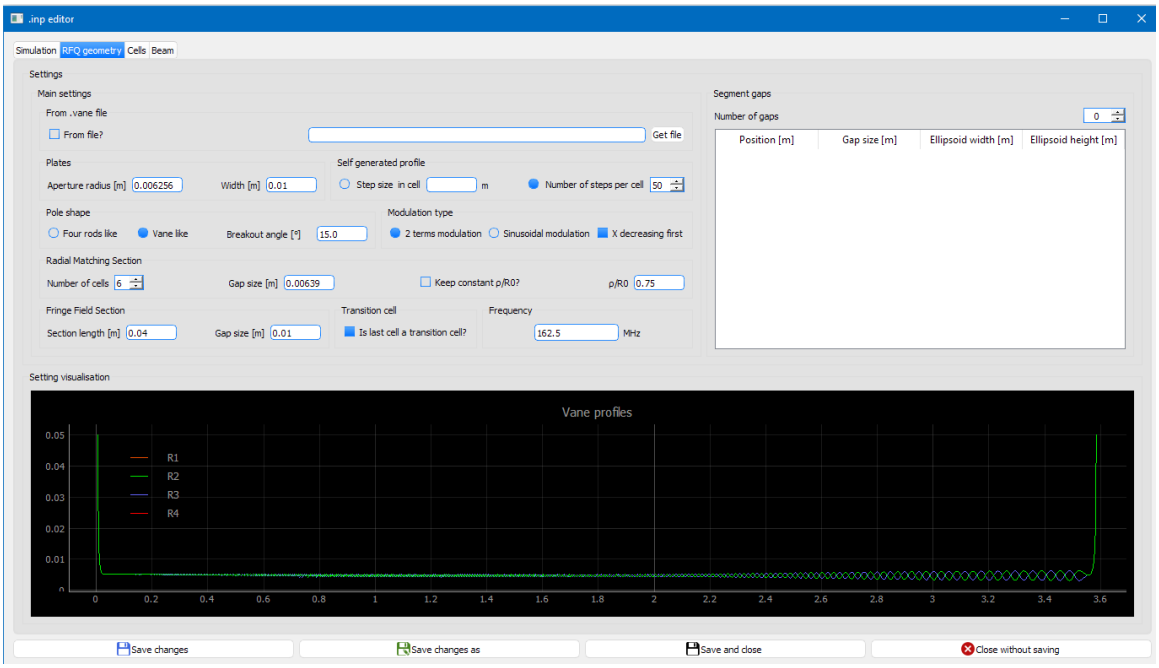

Figure 2.7. A screenshot of the "RFQ Geometry" tab in Toutatis.

data cannot be copy-pasted from this interface, but can be extracted from the *.inp* file for further manipulation—in Excel, for example.

The *Beam* tab (Figure 2.8) contains information and settings about the particle beam to be accelerated by the RFQ. For our purposes, I set the particle type as a 20 keV/u deuteron. The *Transverse Twiss parameters* dictate the initial state of the beam. It may be necessary to manually adjust these to match the RFQ entrance.

When the settings in the various tabs of the input file have been set as desired, the user can save the settings and close the input file editor window. Upon saving the new input file, Toutatis creates a backup version of the old input file in the working directory, to the file name of which it appends the suffix *_OLD* so that the previous settings can be recovered if desired. The simulation can now be run by pressing the *Run* button.

Upon starting the simulation, Toutatis will generate by default several ani-

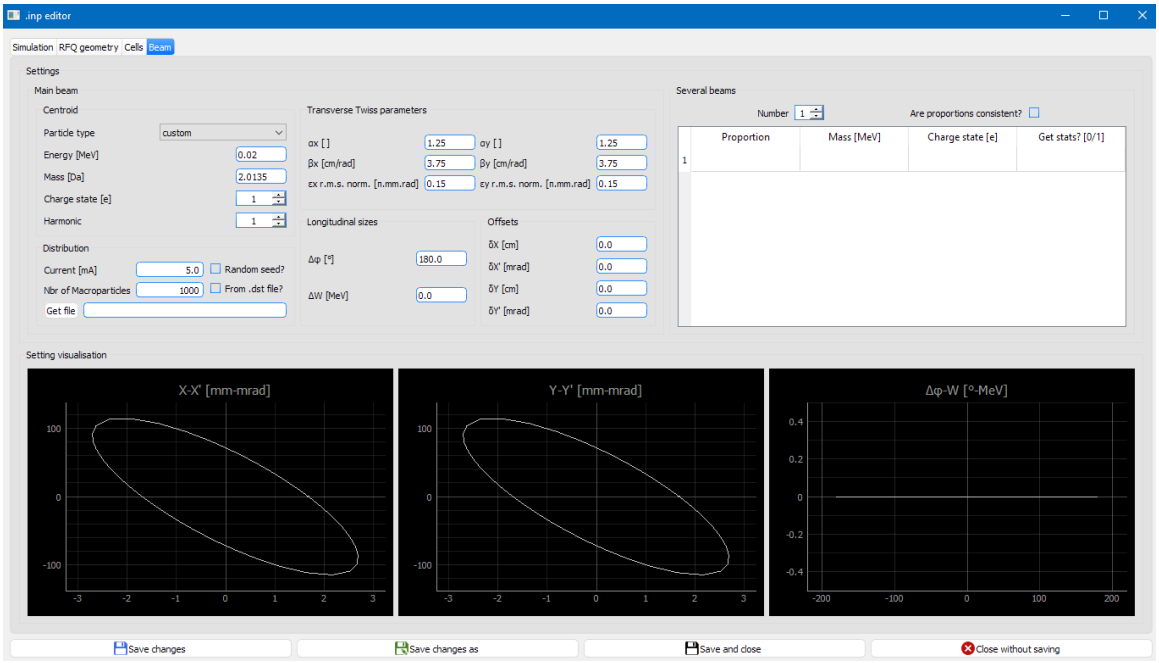

Figure 2.8. A screenshot of the "Beam" tab in Toutatis.

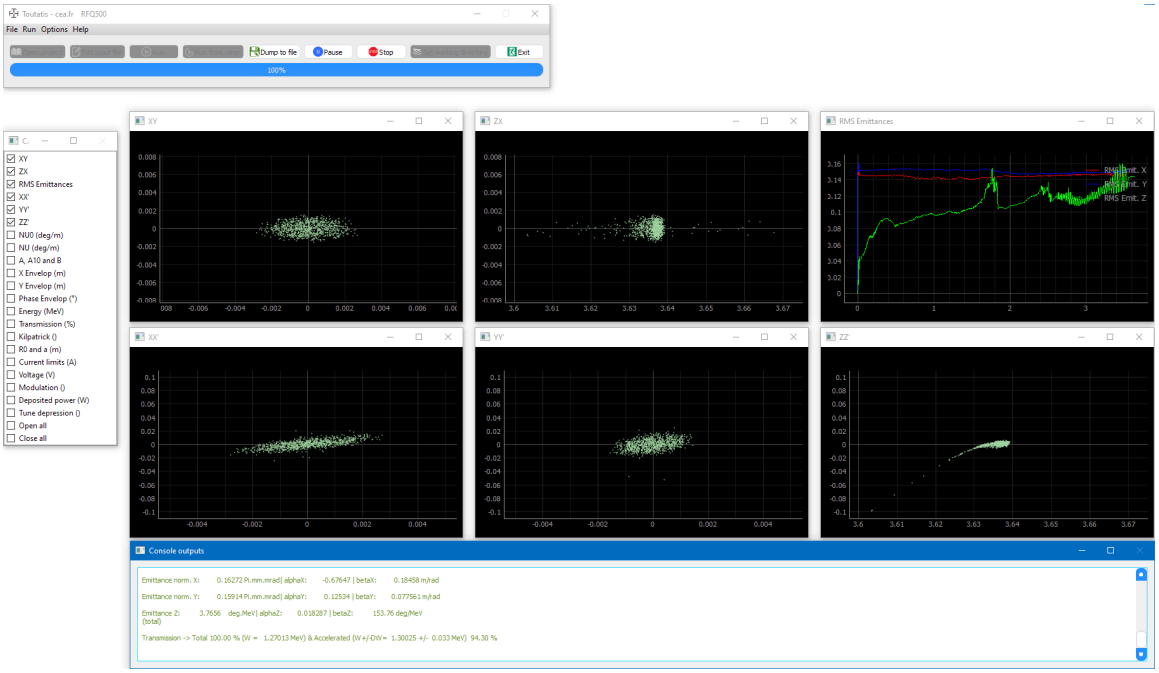

Figure 2.9. A screenshot of the simulation output in Toutatis.

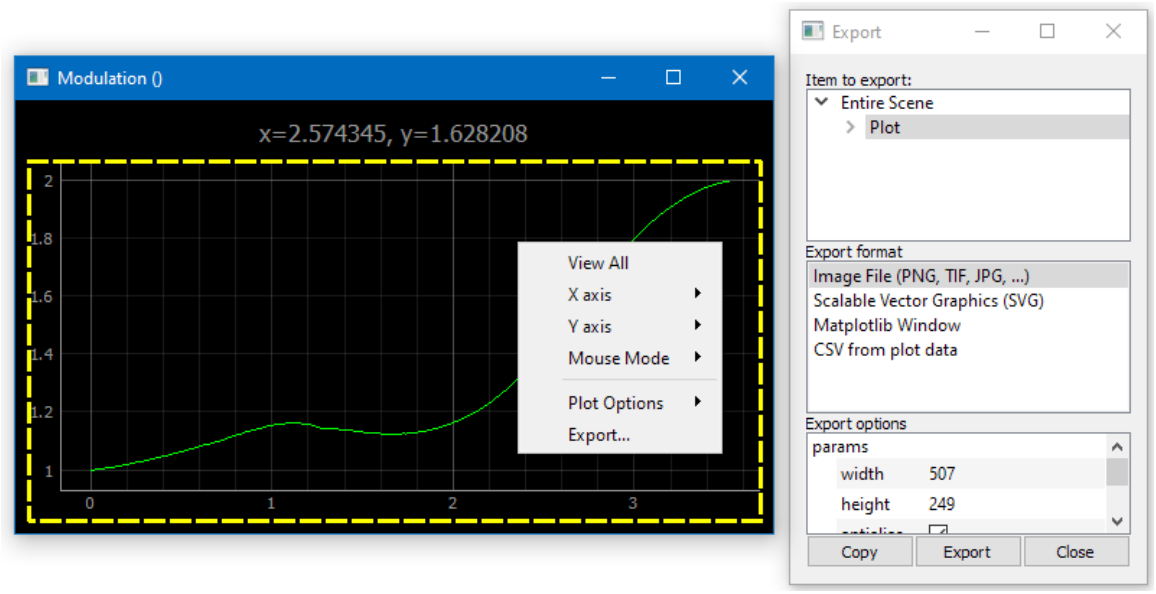

Figure 2.10. A screenshot of the output graphic right-click and export menu in Toutatis.

mated graphics that display the evolution of the xy profile of the accelerated bunch; the zx profile; the RMS emittances; and the xx', yy', and zz' phase profiles. It will also output in text form the resultant beam parameters in the *Console outputs* window, which can be resized. The *Chart list* window on the left can be used to select and de-select certain graphics for display, which can be done while the simulation is in progress. The individual output plot graphics do not have any buttons visible on their interface, but any particular graphic can be exported by right-clicking the body of the plot and selecting *Export...* (Figure 2.10). The plot can then be exported in a variety of file formats.

The *X Envelope (m)* and *Y Envelope (m)* graphics may be useful for manual matching of the beam into the entrance of the RFQ. In Figures 2.11 and 2.12, it can be seen that there are significant secondary oscillations in the transverse beam envelopes, due to a mismatch in parameters between the beam and the RFQ. This mismatch of parameters causes a difference of frequency between the beam's betatron oscillations and the RFQ's betatron oscillations, resulting in a secondary oscillation

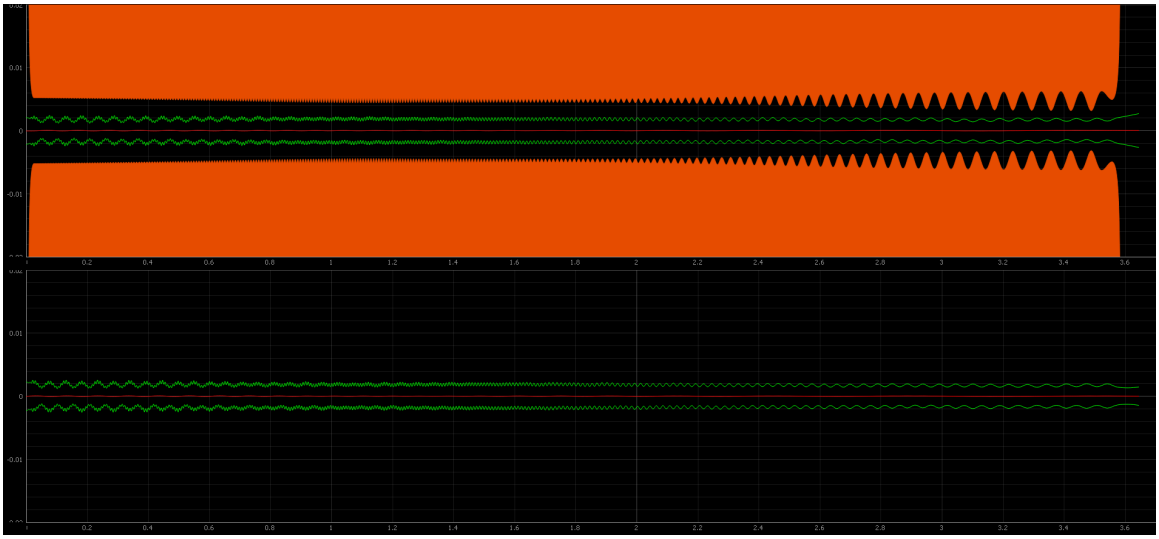

Figure 2.11. A screenshot of the output graphics for x (upper) and y (lower) beam envelopes in Toutatis, with input parameters $\alpha_{x,y} = 0.5$ and $\beta_{x,y} = 3.0\,\mathrm{cm/rad}$. In the plot of the beam's x envelope, the RFQ vanetip surface is also shown, in red. The vanetip surface is not depicted in the lower plot, which is at the same scale. The transmission within $\pm 2.5\%$ of 1.3 MeV was 91.90%.

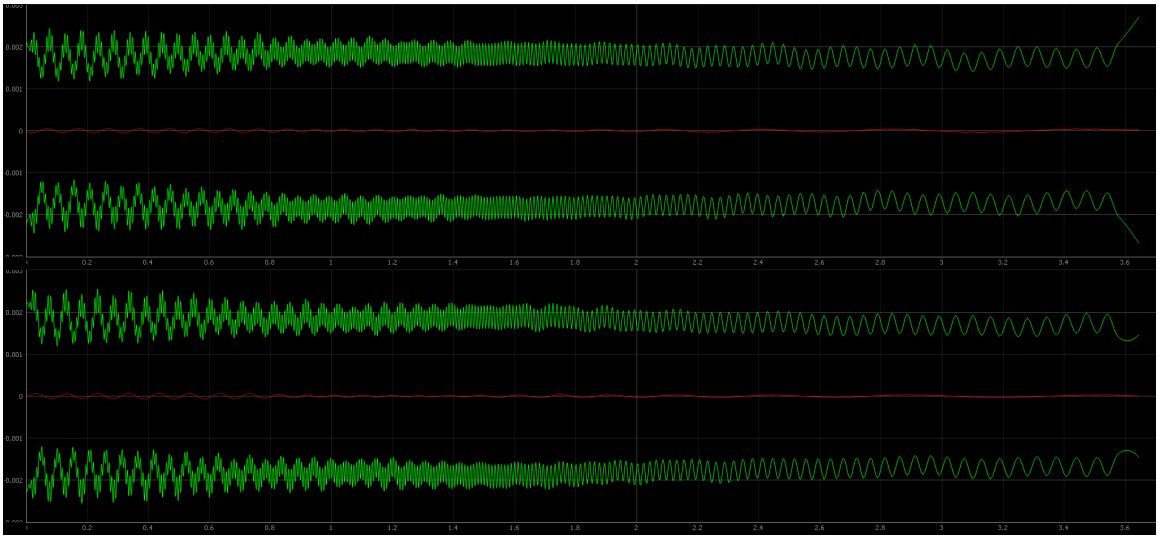

Figure 2.12. The same plot as above, with the y scales of both plots magnified. Note the significant secondary oscillations, resulting from a mismatch of the beam's parameters to the RFQ's parameters at the entrance.

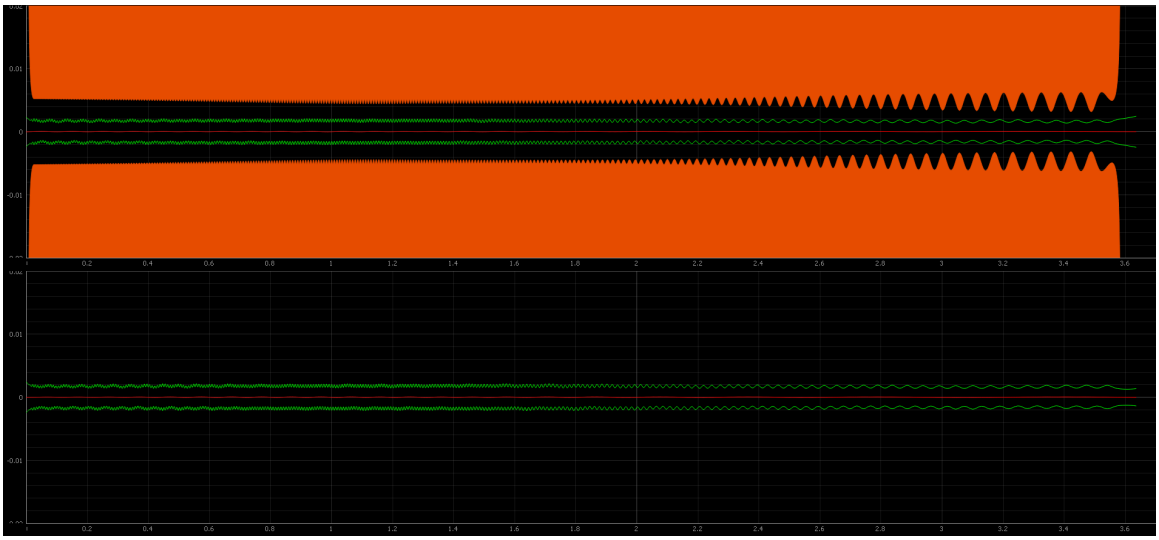

Figure 2.13. A screenshot of the output graphics for x (upper) and y (lower) beam envelopes in Toutatis, with input parameters $\alpha_{x,y} = 1.0$ and $\beta_{x,y} = 3.75\,\mathrm{cm/rad}$. The transmission within $\pm 2.5\%$ of 1.3 MeV was improved to 94.20% over the parameter choice in Figure 2.11.

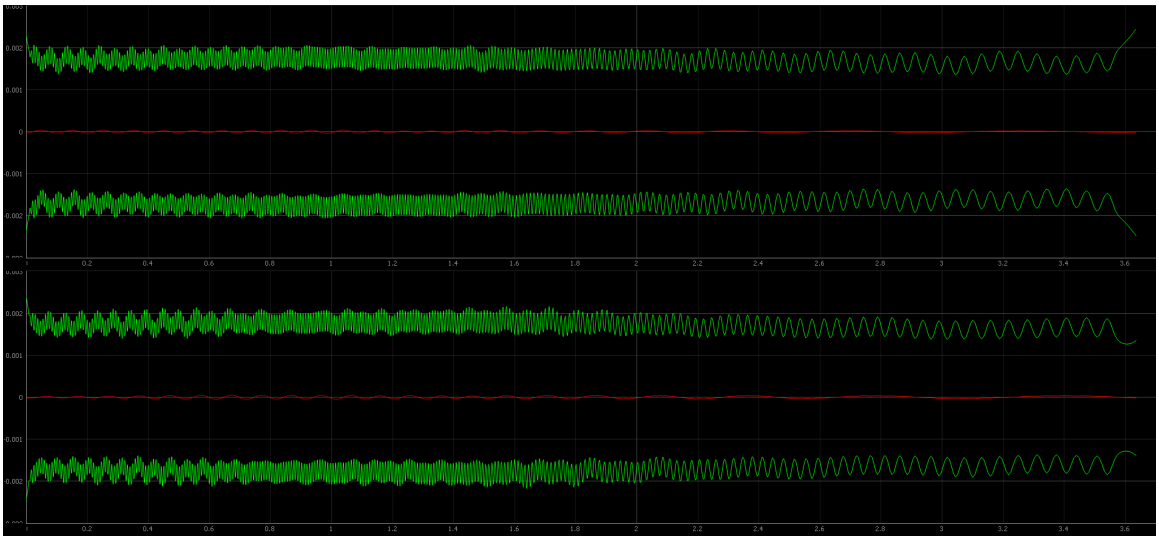

Figure 2.14. The same plot as above, with the y scales of both plots magnified. Note the markedly decreased secondary oscillations, due to improved matching of the beam's parameters to the RFQ's parameters at the entrance.

with the frequency equal to the difference of the two frequencies, which is analogous to the phenomenon in multi-pass accelerators known as a β beat [12]. To reduce these oscillations, the input parameters of $\alpha_{x,y}$ and $\beta_{x,y}$ can be adjusted from the default values. In Figures 2.13 and 2.14, the parameters have been adjusted so that the secondary oscillations are much smaller. When manually matching the beam parameters to the RFQ parameters, i.e. trying different combinations of α and β, attention should be paid to ensure that the parameters are within a reasonable range. The phase ellipse should not be squeezed or stretched too thinly (β should not be too small or too large) and the phase ellipse tilt angle should not be too severe (α should not be too large). In my case, the parameters $\alpha_{x,y} = 1.0$ and $\beta_{x,y} = 3.75\,\mathrm{cm/rad}$ describe a reasonable set of beam parameters and are close to matching the RFQ parameters, eliminating much of the secondary oscillations.

2.4 Building the RFQ in CST

While the RFQ Designer software is able to generate a list of RFQ parameters, and the Toutatis software is able to perform beam simulations on the RFQ, neither software actually gives a physical model of the RFQ that can be examined. In order to do that, I used the software CST Studio Suite (CST) [13]. Creating a simulated 3D model of the RFQ is helpful to visualize the RFQ as it actually would appear in real life, and CST also has the capability to perform electrostatic simulations to check whether the 3D model agrees with the generated RFQ parameters. Having two independent programs agree on the RFQ performance bolsters the credibility of the design by eliminating the possibility that the design is the result of artifacts of a specific implementation, numerical scheme, or software anomaly.

Regarding the equations of geometry of the RFQ cells, the aperture in a particular cell will be either increasing in the x direction and decreasing in the y direction, or decreasing in the x direction and increasing in the y direction. In order to cre-

ate this shape, we vary the aperture width according to a sinusoidal curve, which in general has the form

$$A \cdot \sin\left(B \cdot (x - C)\right) + D. \tag{2.5}$$

We need to create a geometry that is not rotationally symmetric about the z axis and varies along the z axis, so it is not possible to generate the vanetips by rotating a series of connected points about the z axis, nor is it sufficient to extrude a 2D geometry along the z axis. Firstly, let us consider the variation along the z axis. At cell number i, the aperture radius (distance from the z axis to the vanetip)—in the x direction, for instance—should vary from a_i to $m_{i+1}a_{i+1}$. Correspondingly, in the y direction, the aperture radius would vary from $m_i a_i$ to a_{i+1}. This project's RFQ was generated with a sinusoidal, as opposed to "2-terms" modulation, as mentioned in Section 2.2. Thus the vanetip geometry for cell i in the vertical vane should have the form

$$y = \frac{a_i m_i - a_{i+1}}{2} \cdot \left(1 \pm \cos\frac{\pi \cdot z}{\ell_i}\right) + a_{i+1} \tag{2.6}$$

within the bounds $\{z_{i-1} \leq z \leq z_i\}$ where z_i is the z coordinate of the beginning of cell i. The plus/minus sign in Equation (2.6) denotes either a cell whose aperture is decreasing (plus) or increasing (minus).

As mentioned in Section 2.2, my RFQ was generated with the constraint that the vanetip radius be constant along the RFQ, in this case being equal to $\rho = 0.39\,\text{cm}$. The simplification that this affords our CST model proves to be a boon, because otherwise our model would be dramatically more complicated, with each cell possibly having a different vanetip radius. Also, the vanetips were modeled in CST as circular instead of hyperbolic in order to simplify the geometry.

In the transverse cross-section, we should see circular vanetips, with vanetip radius ρ. Thus, we must modify the above equation to include a transverse circular

profile:

$$y = \frac{a_i m_i - a_{i+1}}{2} \cdot \left(1 \pm \cos\frac{\pi \cdot z}{\ell_i}\right) + a_{i+1} - \sqrt{\rho^2 - x^2} + \rho. \tag{2.7}$$

The horizontal (x direction) vanes will have a y variable in the square root and x on the left-hand side:

$$x = \frac{a_i m_i - a_{i+1}}{2} \cdot \left(1 \mp \cos\frac{\pi \cdot z}{\ell_i}\right) + a_{i+1} - \sqrt{\rho^2 - y^2} + \rho. \tag{2.8}$$

Equations (2.7) and (2.8) describe the vanes in the positive x and y directions, and the vanes in the negative directions can be generated by rotating by 180 degrees around the z axis (or equivalently, reflecting through the origin, or across the $x = 0$ and $y = 0$ planes) the entire vane in CST once it has been generated.

This project's RFQ has 500 cells, each with several independent parameters, so manually generating each cell would be prohibitively tedious. Hence, a Visual Basic for Applications (VBA) macro was used to generate the RFQ geometry. VBA is a scripting language for which CST has built-in compatibility, so it can easily be used to control CST. For our purposes, we can use VBA to parse a list of RFQ parameters and output 3D models of cells with those parameters (see Appendix B for the full script). In order to get a list of my RFQ parameters for VBA to translate into shapes, I used Python to compile a list of relevant RFQ parameters from the RFQ Designer file. Specifically, the purpose of Python here is to translate the characteristic format of the RFQ Designer software files into a nicely-formatted list of parameters that will be accepted by CST. Namely, I needed, for each cell numbered i: a minimum aperture *ai*, a modulation *mi*, a cell length *lcelli*, and a position of the cell *zoffseti*. All the other parameters given by RFQ Designer, such as the synchronous phase, acceleration efficiency, and vanetip radius for each cell, are irrelevant for the purposes of generating the 3D CST model (as stated earlier in this section, the vanetip radius was modified to be constant along the RFQ for its CST model). The final (exit) cell

must be altered slightly so as to taper into a four-fold symmetric exit. This is done by setting the final modulation to 1. Also included in the parameter list is the value for the vanetip radius, ρ, and the length of the vanetips *vanelen*. The length of the vanetips should be long enough so as not to have the fringe fields disrupt the fields on the axis, but not so long as to be a detriment to the precision of the simulation. The longer the vanetips are in our model, the larger our entire model is in size, and so we will have to confront the trade-off between how long it takes for simulations to run and how precise or granular the simulations will be. In my case, a vanetip length of 10 times the maximum aperture distance, i.e. 5.2 cm, was long enough to keep the aperture sufficiently isolated from the other end of the vane, and short enough to ensure a high-precision simulation (6,602,770 meshcells) in a reasonable amount of time (less than an hour per run).

The VBA macro was created starting by first manually generating a few solids. Using the *Analytical Face...* feature in the *Modeling* tab, I inputted the vanetip surface geometry equations for the first cell in the $+x$ direction, and then used the *Loft* tool with a flat rectangle to produce a solid vanetip. Then I did the same in the $+y$ direction. The vanetips in the $-x$ and $-y$ directions can be produced by simply rotating the vanetips by π about the z axis, which will be done later to speed up the process. The vanetips we have created so far are, for instance, widening in the x direction and narrowing in the y direction, so we must also create the second set of vanetips (narrowing in the x direction and widening in the y direction) in order to get our periodic structure form. Next I opened the *History List*, clicked *More>>*, highlighted the relevant actions that created the first two cells, clicked *Macro...*, and entered a name for my structure macro (*rfqgen*). This automatically translates our actions into a VBA script. Now we must edit the script into something that loops over the number of cells (in my case, 500) and uses the corresponding geometrical parameters for each cell. This is done by incorporating the parameter list I generated

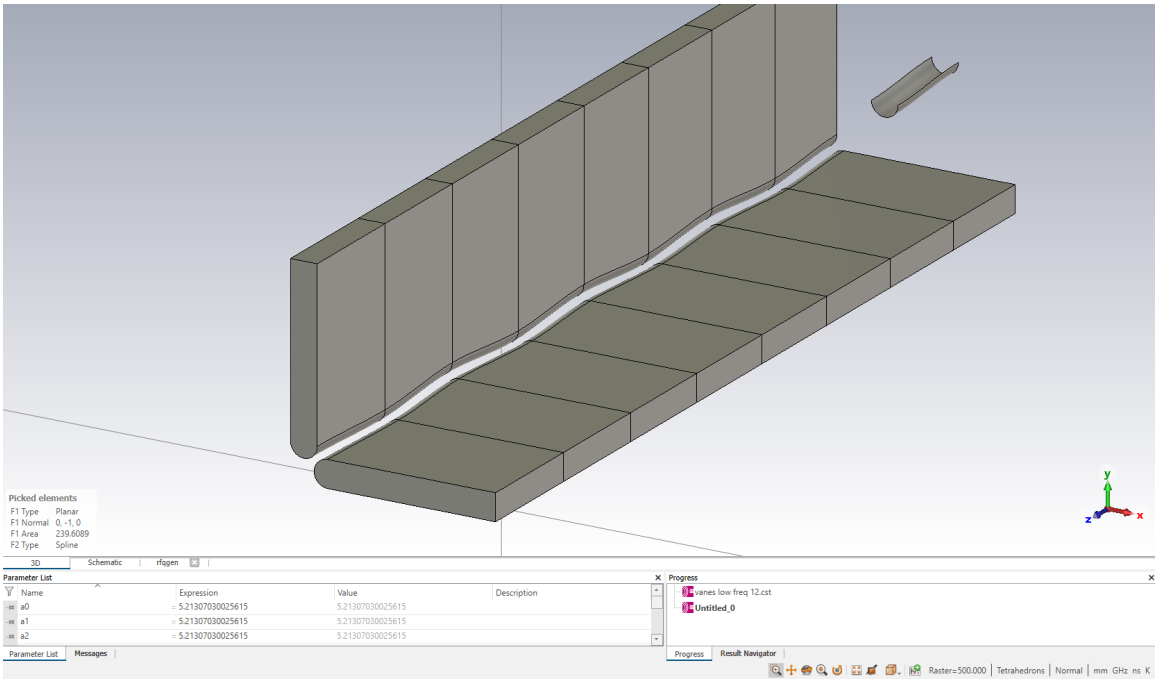

Figure 2.15. The CST interface in the *3D* tab (bottom left of main panel), showing in the in-progress generation of the RFQ cells by the VBA macro.

with Python.

The VBA script takes a few minutes to run. The progress can be tracked by navigating back to the *3D* tab (which can be found in the bottom left of the main panel, as seen in Figure 2.15), as well as expanding the component in the *Navigation Tree*. After the entire macro has executed, I save the file, and this file will be treated as a kind of template file. When running simulations in CST, it will be much faster to copy and paste the structure from this template file into a separate project, instead of editing the original file directly. This is because running the VBA macro does not produce steps in the *History List*, and so if the history list if updated, all the macro-generated solids will disappear and it will be necessary to re-run the macro, taking another several minutes.

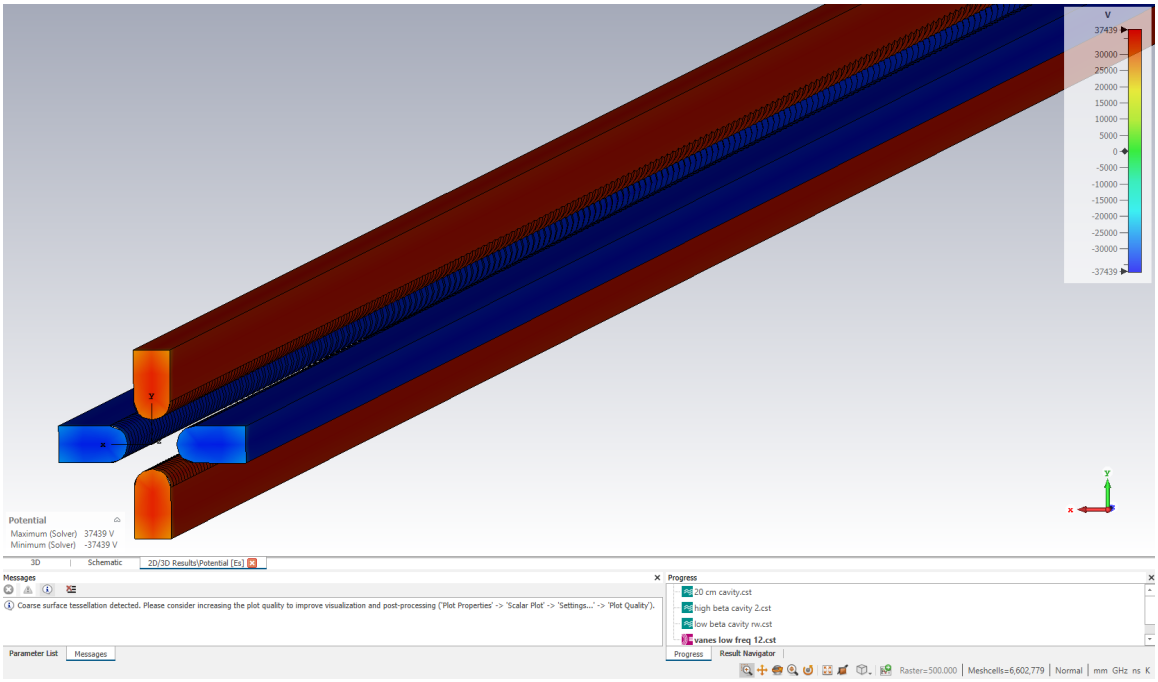

Figure 2.16. The RFQ vanes with a constant +37439 V on the vertical vanes and a constant −37439 V on the horizontal vanes.

2.5 CST simulation

With the model assembled in CST, I simulated the electric field in two different ways. The first was to use the electrostatic solver, which would show me the electric fields resulting from a constant and uniform voltage applied to the vanes (Figure 2.16. To do this, I first created a new low-frequency regime CST project.

In this new project, I ensure that the units are correct, especially millimeters for spatial units. Then I paste in the solids created in my template file. I combine all the solids into one single object by selecting them all and using the *Boolean* addition function. Then I *Transform* the object, rotating it 180 degrees about the z-axis and creating a copy. Thus, I now have two objects: one for the vanes adjacent to the first Cartesian quadrant and one for the vanes adjacent to the third Cartesian quadrant. Next, we need to set the boundary conditions. In the *Simulation* tab, I set the *Boundaries* to *open (add space if)* and use the extra space factor of 0.001. Since we

are not concerned with the field far from the axis, this factor should be small to not add unnecessary complexity. We also need to define a mesh of suitable granularity for the solver. In order to get reasonable precision at the small region around the axis that we are interested in, the number of meshcells should be at least on the order of the ratio of the entire model's volume to the volume of a cube with side length equal to the smallest relevant lengths. In my case, the smallest relevant lengths are smaller than the aperture radius $\rho = 0.39\,\text{cm}$ and the entire model's volume is approximately 3.56 m by 12 cm by 12 cm. Thus the mesh should have at least

$$\frac{3.56\,\text{m} \cdot 12\,\text{cm} \cdot 12\,\text{cm}}{(0.39\,\text{cm})^3} \approx 870000$$

cells. This merely serves as a lower bound, and in reality it would help to have several times this amount, so my final mesh used 6,602,770 hexahedral meshcells (Figure 2.17). The hexahedral meshcell shape resulted in a more ordered and consistent field, compared to using a tetrahedral mesh (Figure 2.28). In the mesh's *Global Properties*, around 500 cells per wavelength in both the model and the background will give around that many meshcells, although using more will in general improve the simulation. The electrostatic simulation runtime is mainly CPU-dependent, as opposed to the eigenmode solver which uses significant RAM and will slow down immensely, to the point of unreasonably slow progress, if the amount of usable RAM is insufficient. This is due to disk speeds being much slower than RAM speeds when using disk swap space as RAM when RAM is at capacity. Thus, using a high number of mesh cells in the electrostatic solver will increase the runtime, but one can be assured that the simulation will, in general, eventually complete. When setting the number of mesh cells, the user can either update the mesh immediately in the dialogue box or generate the mesh when starting the simulation. For the voltage difference between the vanes, I applied an electric potential of $\frac{V}{2}$ on the $+y$ and $-y$ vanes, where V is the intervane voltage and is equal to 71312 V as given by the RFQ Designer optimizer, and an electric potential of $-\frac{V}{2}$ on the $+x$ and $-x$ vanes. These

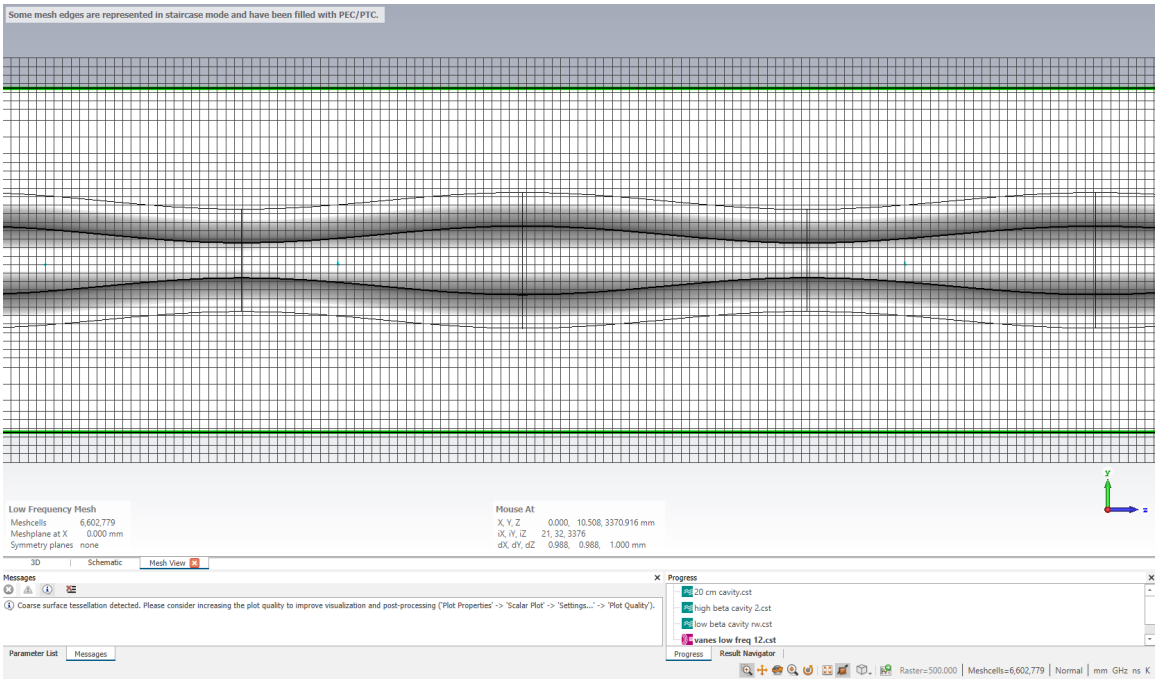
Some mesh edges are represented in staircase mode and have been filled with PEC/PTC.
Low Frequency Mesh
Meshcells 6,602,779
Meshplane at X 0.000 mm
Symmetry planes none
Mouse At
X, Y, Z 0.000, 10.508, 3370.916 mm
iX, iY, iZ 21, 32, 3376
dX, dY, dZ 0.988, 0.988, 1.000 mm
3D
Schematic
Mesh View
Messages
Coarse surface tessellation detected. Please consider increasing the plot quality to improve visualization and post-processing ('Plot Properties' -> 'Scalar Plot' -> 'Settings...' -> 'Plot Quality').
Progress
20 cm cavity.cst
high beta cavity 2.cst
low beta cavity rw.cst
vanes low freq 12.cst
Parameter List
Messages
Progress
Result Navigator
Raster=500.000
Meshcells=6,602,779
Normal
mm GHz ns K

Figure 2.17. A close-up of the RFQ hexahedral mesh with a total of 6,602,770 mesh-cells. The hexahedral mesh produced a more uniform field than using a tetrahedral mesh.

are done by right-clicking on the *Potentials* folder in the navigation tree and selecting the vanes with the mouse by clicking on one of their surfaces.

When starting the simulation, by clicking *Setup Solver* in the *Simulation* tab, a target accuracy can be set by the user. This is the upper boundary for the simulation error, and the simulation will continue taking steps until the error, or residual, is below this value. Also, the user can set a number of mesh refinement passes for the simulation. With each pass, when the simulation has run its course to the desired accuracy level, the solver will pick a certain number of tetrahedrons in the mesh to refine, in order to create a higher-quality and better-suited mesh for the problem. Then the simulation will once again run until the desired accuracy level. For our purposes, I set a target of *1e-12* to get a higher accuracy near the axis, and two passes. Once the number of passes has been completed, one can view the electric field as a 3D visualization in the *2D/3D* section. The field can also be inspected

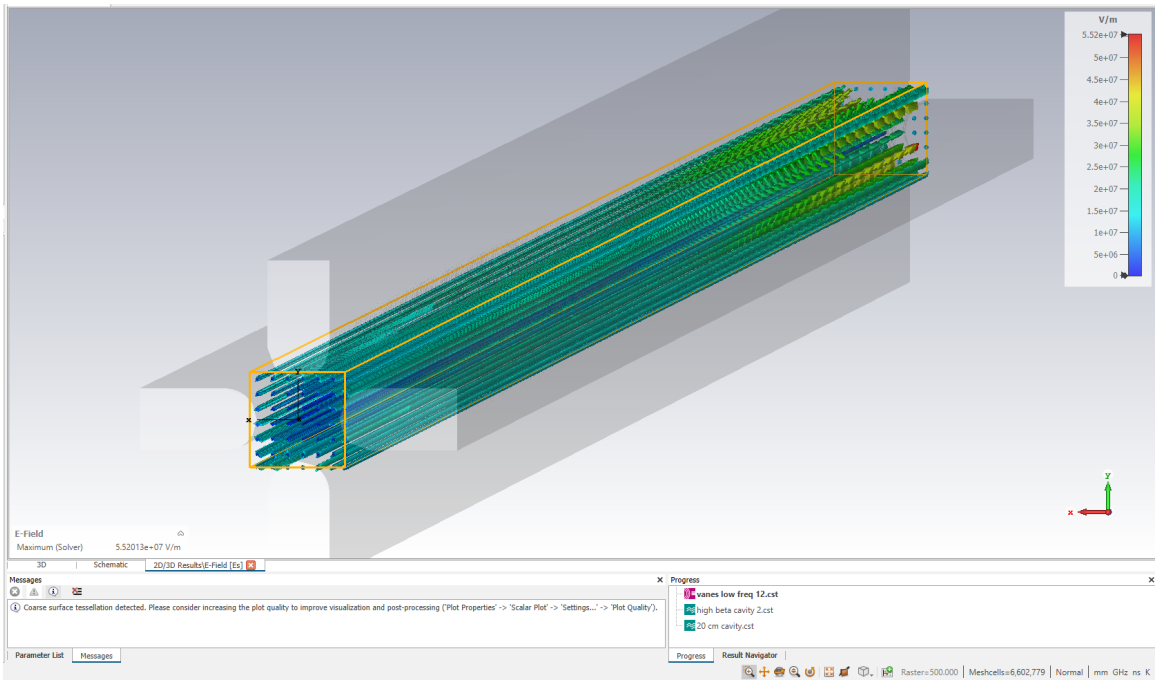

Figure 2.18. Subvolume of the RFQ inside of which the E-fields are exported.

on, and projected on, a cross-sectional plane. For my purposes, the field data must be extracted to compare with the Toutatis simulation. To do this, the *Export as ASCII* option can be selected in the *Post-processing* tab. This will create a text file with the (E_x, E_y, E_z) data. In the subsequent dialogue it is necessary to determine the 3D grid along which data points will be given, as well as a subvolume of the model (Figure 2.18), since we are not interested in the field far from the axis. In our particular RFQ, the maximum aperture radius is around 5 mm, so I chose a subvolume of $[-6, 6] \times [-6, 6] \times [0, l]$ in xyz where l is the length of the RFQ in mm. For the purpose of comparison with the Toutatis output, I exported the fields with 25 points in the x and y directions, and 4001 points in the z direction—enough points longitudinally to get at least 4 longitudinal data locations for even the shortest cells.

I also used the high-frequency CST solver [13] to model the RFQ, to see whether the more realistic behavior of a time-varying field could be replicated in CST as it was simulated in Toutatis. Such an approach has been undertaken by the

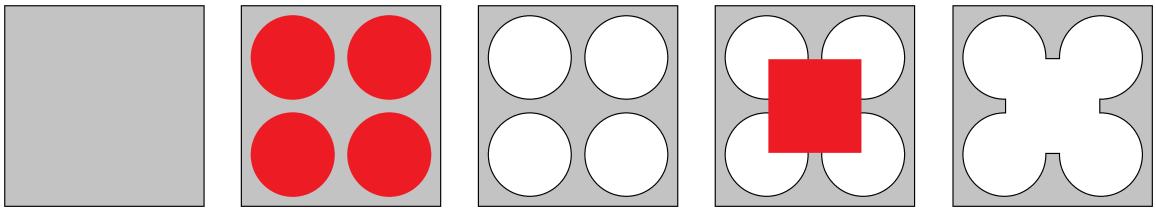

Figure 2.19. Constructing the cloverleaf resonator shape by subtracting (in red) four cylinders and a square prism from a square prism perfect conductor body (gray). The vanetips can then be attached to the middle of this resonator body.

designers of the SARAF RFQ in CST Microwave Studio, for example [14]. In order to produce a high-frequency model, the rest of the resonator must be modeled in CST. I first used a cloverleaf geometry to model the entire resonator (Figures 2.19, 2.20, 2.21). This geometry entails a vanetip of constant width transitioning into a circular resonator quadrant. In CST, this can be achieved by subtracting four cylinders of radius r_c as well as a square prism from a square-prism perfect conductor, which gives the namesake cloverleaf shape (Figure 2.19). As a first guess of the radius of each leaf, I used the capacitance relation [15]

$$\omega_0{}^2 = (L'C')^{-1} = \frac{16}{\mu_0 \left(4 + 3\pi\right) r_C{}^2 C_\ell}, \tag{2.9}$$

where ω_0 is the resonant frequency (162.5 MHz) and C_ℓ is the total capacitance per unit length of the structure, which is suggested to be in the neighborhood of $120 \cdot 10^{-12}$ F/m. Once the resonator was connected to the vanes in CST by using the *Boolean* addition function, I used the eigenmode solver to find out what the resonant frequency of the structure was. The resultant calculation for the cloverleaf radius r_C of 0.54 m ended up giving a resonant frequency that was too low, so it was necessary to decrease the radius in increments until the high-frequency eigenmode simulation showed a resonant frequency close to 162.5 MHz.

To use the high-frequency eigenmode solver in CST, the first step is to set up the conditions for the appropriate simulation of the RFQ. This includes choosing the solver type of the high-frequency regime, setting the solver type to eigenmode,

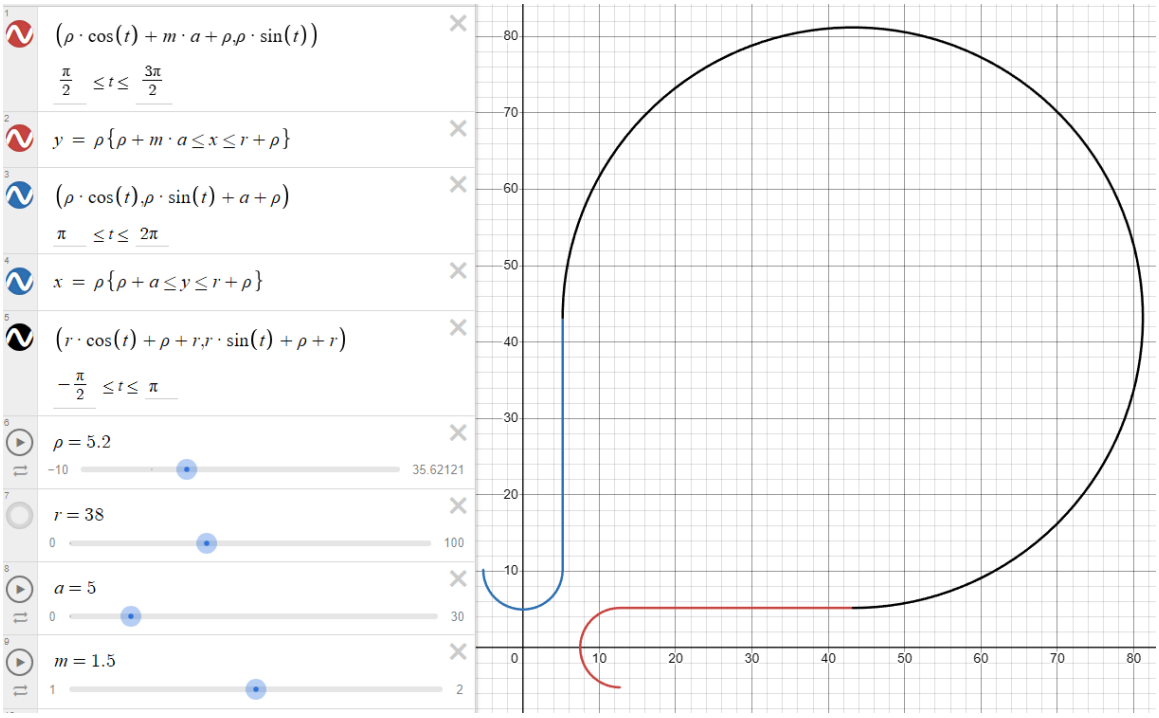

Figure 2.20. Equations for the cloverleaf geometry, describing connecting the straight vanetips with circular arcs, shown here for one "leaf."

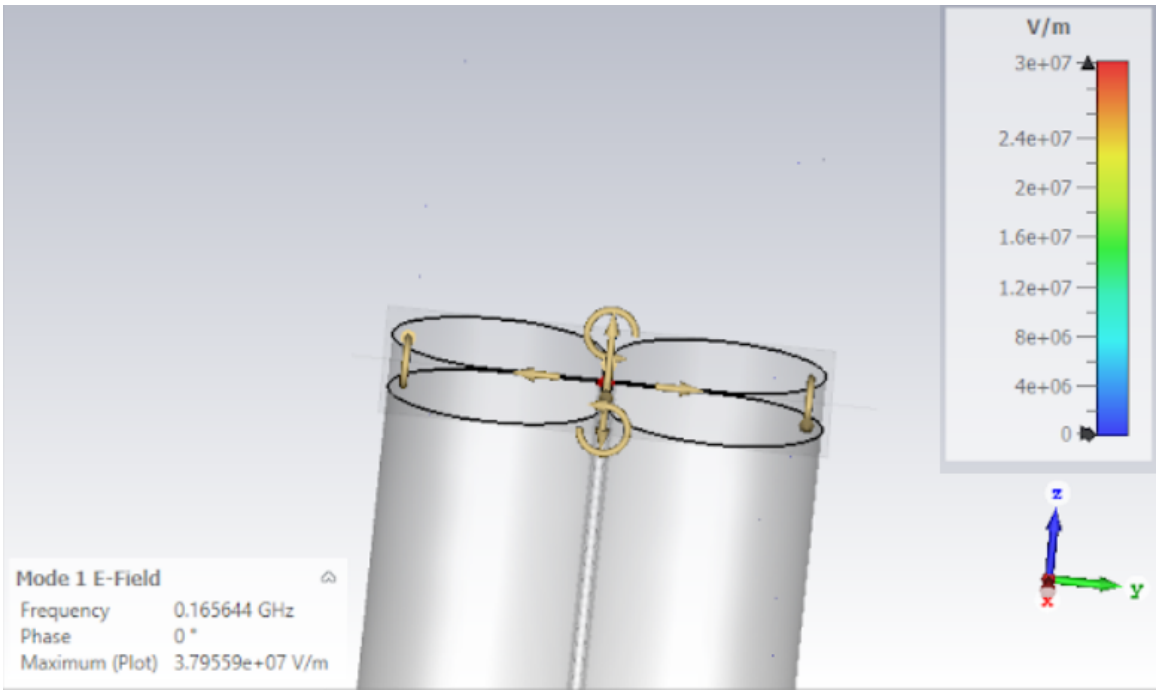

Figure 2.21. The CST model of the cloverleaf resonator.

defining the boundaries as having the electric field be zero at the boundaries of the RFQ, and defining a frequency range appropriate for finding the resonant frequency of the RFQ. The geometric parameters were adjusted to achieve the desired resonant frequency; for the cloverleaf design, the only geometric parameter is the "leaf" radius r_C. By running the solver several times and changing this parameter in between each run, I found that the radius of 90 mm gave a resonant frequency of 165.6 MHz, close to the desired frequency.

When using the high-frequency eigenmode solver, the user can direct the program to output details for a certain number of modes. Depending on how wide the frequency range is set, the first few modes may not be the desired RFQ mode. For example, in the simulation run shown in Figure 2.22, the lowest two modes were diagonal modes, where the adjacent $+x$ and $+y$ vanes had the same polarity and the $-x$ and $-y$ vanes had the same polarity. This differs from the RFQ mode (Figure 2.23), where opposing vanes have the same polarity. In such cases where these unwanted modes appear, either the frequency range must be narrowed to exclude these modes, or the user can prompt the program to include details about more modes—in which case the RFQ mode may appear as, for instance, the third lowest mode or so. Increasing the number of modes investigated by the solver will increase the runtime and may cause the simulation to "fail," that is, take an unreasonable amount of time due to RAM capacity; so in general, it is better to narrow the frequency range by increasing the lower frequency bound.

An alternative to the cloverleaf geometry is the so-called breakout geometry (Figure 2.24). This design involves several straight sections connected by circular arcs. Although both types of resonator designs were modeled in CST, none of the high-frequency simulations matched the quality of results of the electrostatic simulation.

Once the simulation calculations have run their course, an additional feature

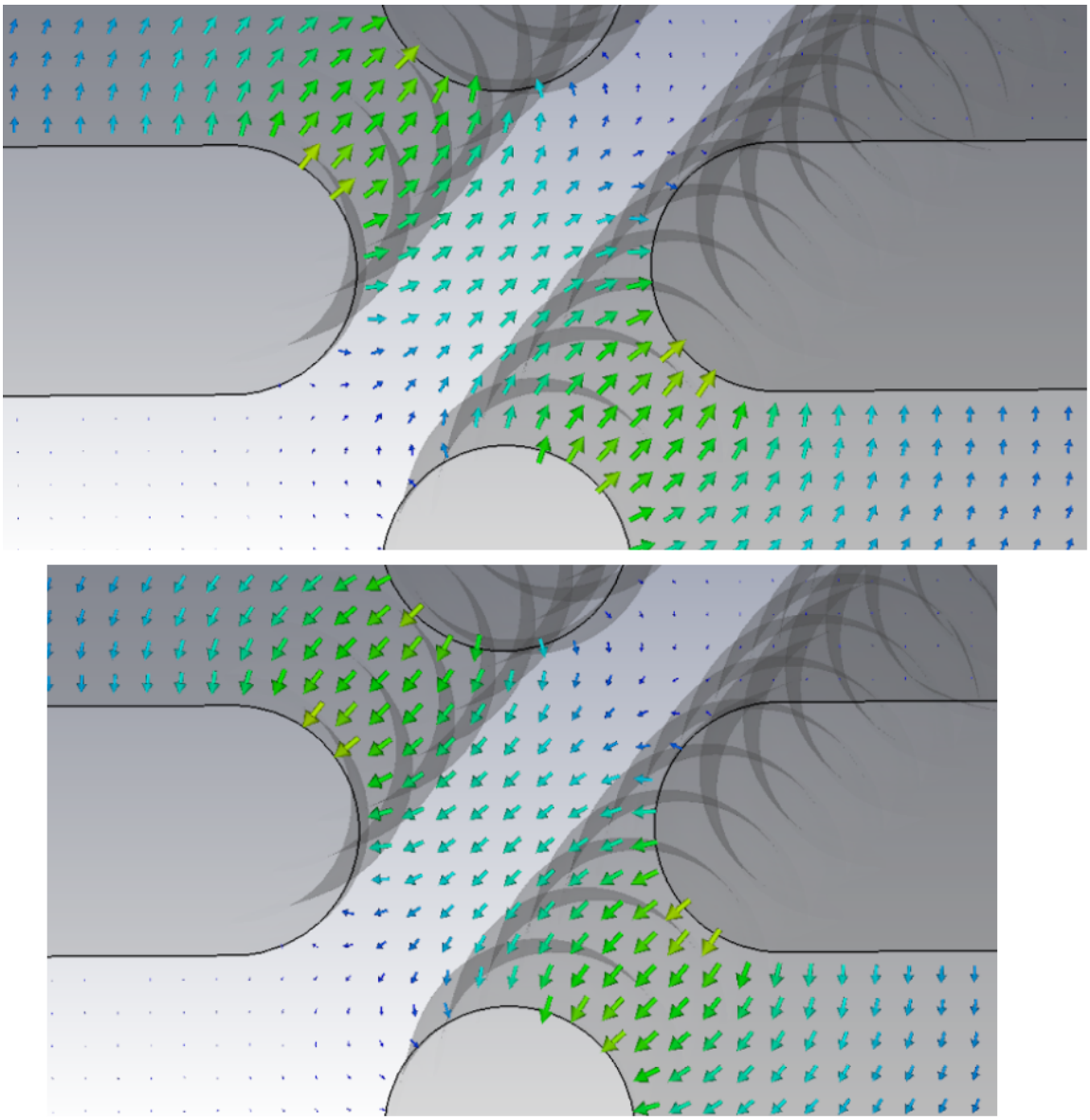

Figure 2.22. Diagonal modes in the RFQ in the high-frequency simulation. These modes are undesired, and their presence in the simulation leads to a disordered field and a differently-shaped field profile than that produced by Toutatis.

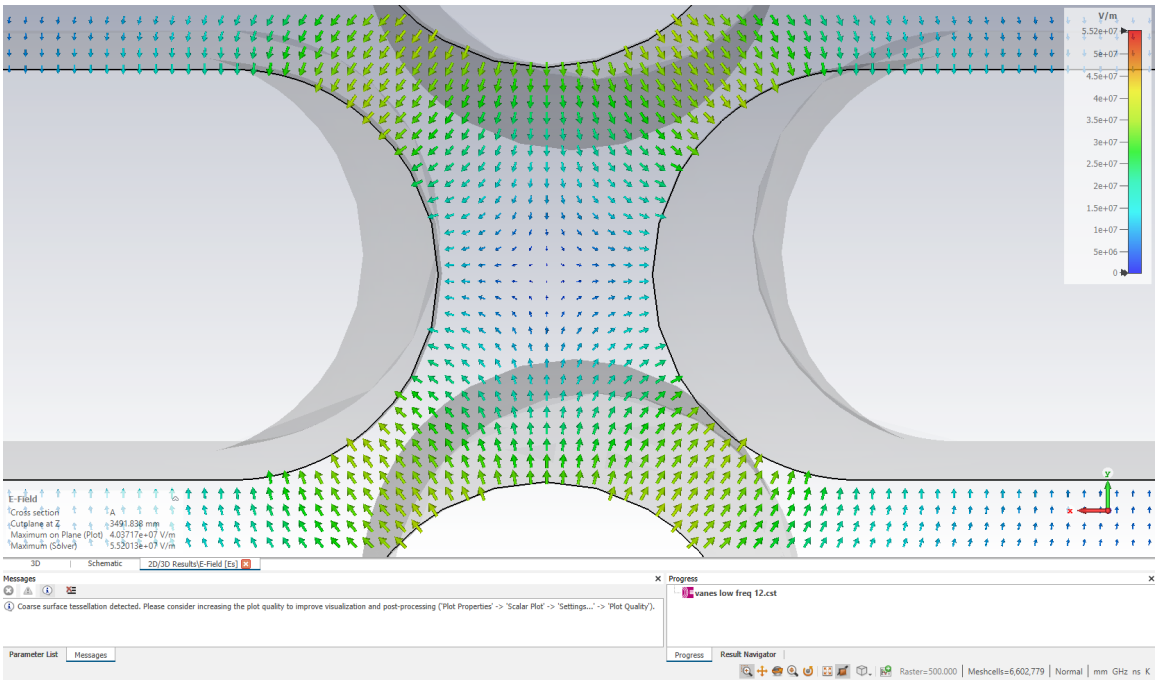

Figure 2.23. The desired RFQ mode, as achieved in the electrostatic simulation.

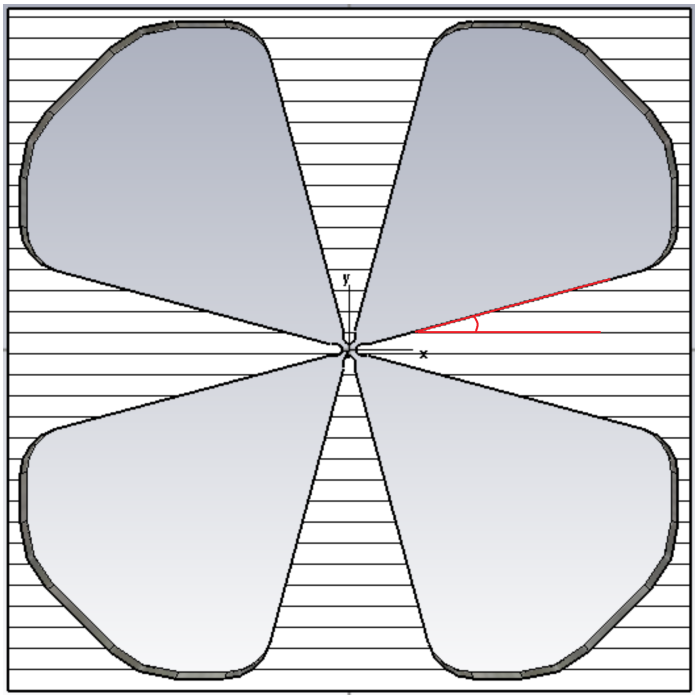

Figure 2.24. Cross-section of the breakout geometry. The red angle is known as the breakout angle as mentioned in Section 2.3.

exists, compared to the electrostatic solver, of viewing the field as an animation. To export the fields, the procedure is the same as described previously in this section (via the *Post-Processing* tab), with the phase set to zero so as to export the fields at their peak.

2.6 Comparison of CST field with Toutatis field

The entire RFQ field as simulated by Toutatis and the electrostatic CST simulation are plotted superimposed in Figure 2.25, with close-ups of the entrance and exit in Figures 2.26 and 2.27. The two field profiles show close agreement, particularly near the exit of the RFQ. Notably, the similarity among the two simulations were achieved despite a number of simplifications/approximations. Firstly, the CST is not a snapshot of a time-varying field but rather a static field. Secondly, only the vanes were modeled, and not the rest of the resonator body. Thirdly, the transverse vanetip geometry was modeled as circular in CST, as opposed to hyperbolic as simulated by Toutatis, for the sake of simplicity. Lastly, the edges of the model that had right angles were kept sharp instead of being blended or tapered, which may have introduced some calculation artifacts at sharp edges (see Figure 2.26).

The results of the cloverleaf resonator model differed greatly from the field produced from the Toutatis simulation. Most notably, when comparing the E_z field on the axis to the Toutatis result as shown in Figure 2.29, the field near the entrance was very disordered, and the field near the exit tapered to zero too quickly, meaning that the geometry of the resonator body is not appropriate for our purposes. The mode mixing of diagonal and other undesired modes likely contributed to the degradation of the RFQ field profile. In essence, it is not productive to attempt to model the RFQ in the high-frequency solver without further, detailed knowledge of the entire resonator body, which was not given by RFQ Designer.

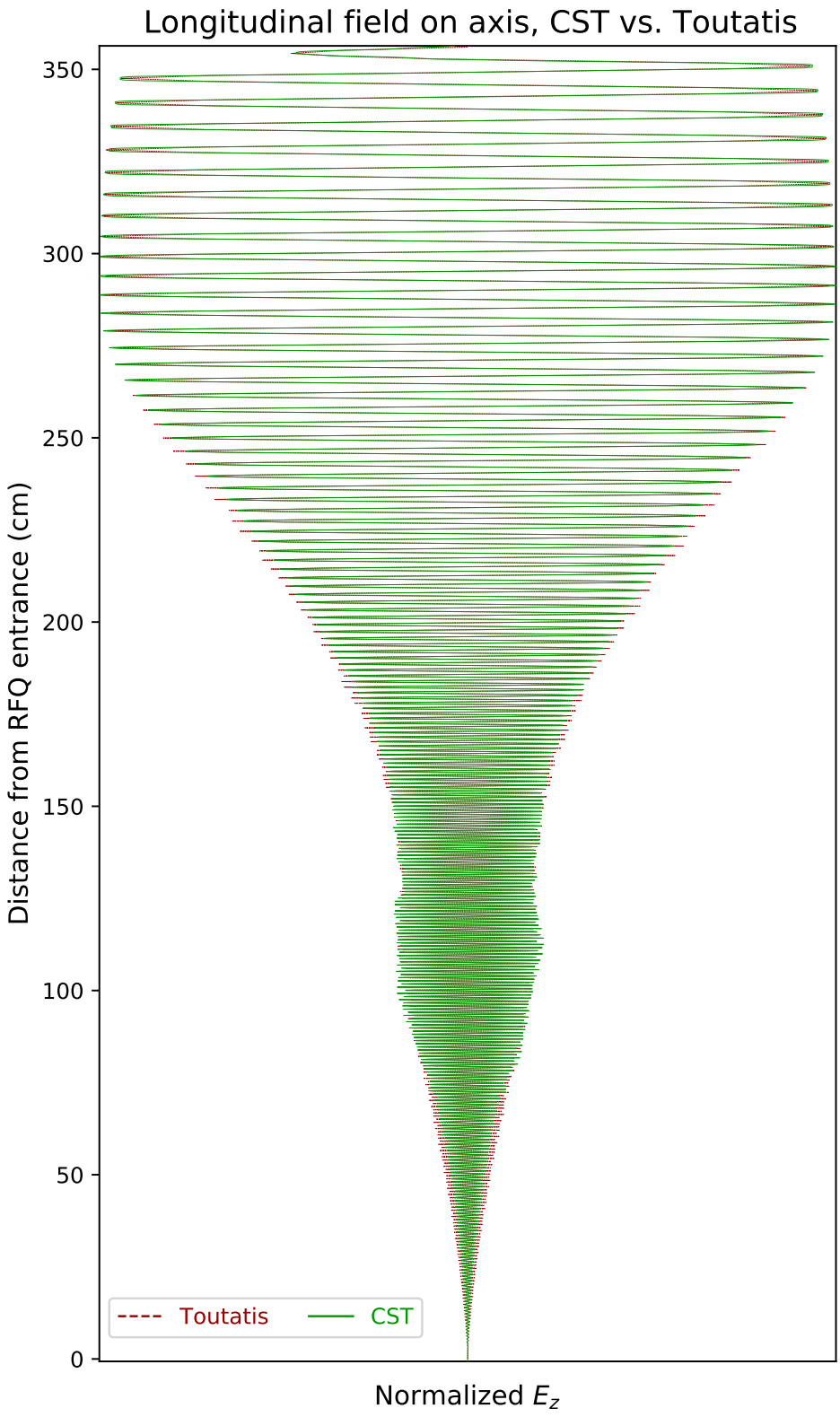

Figure 2.25. E_z on axis in Toutatis (dashed red) and the electrostatic CST simulation (solid green).

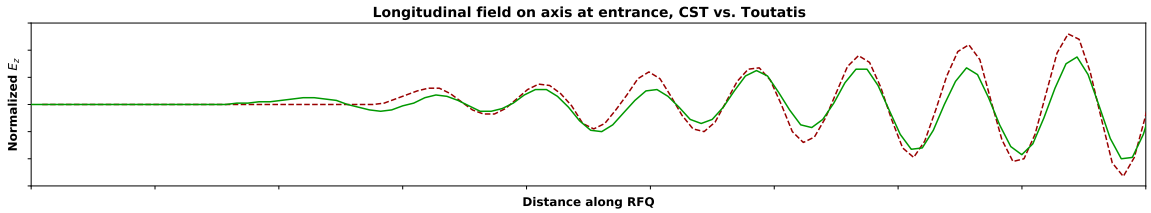

Figure 2.26. E_z on axis in Toutatis and CST, for approximately the first 20 cells. The mismatch at the entrance is due to the CST model not having a radial matching section, and instead having simply a 90-degree cutoff. Compare the tapered entrance and exit vanes as seen in Figure 2.13 with the 90-degree edges as seen in Figure 2.16.

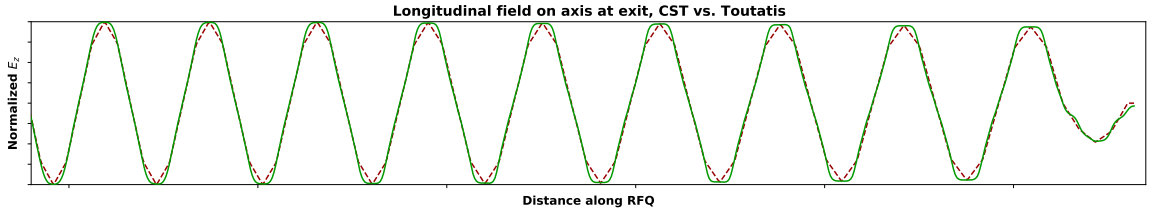

Figure 2.27. E_z on axis in Toutatis and CST, for approximately the last 20 cells.

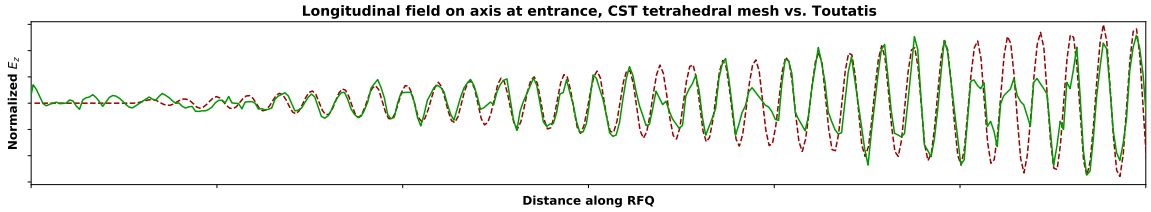

Figure 2.28. Using a tetrahedral mesh resulted in a less ordered field profile than the hexahedral mesh (compare with Figure 2.26).

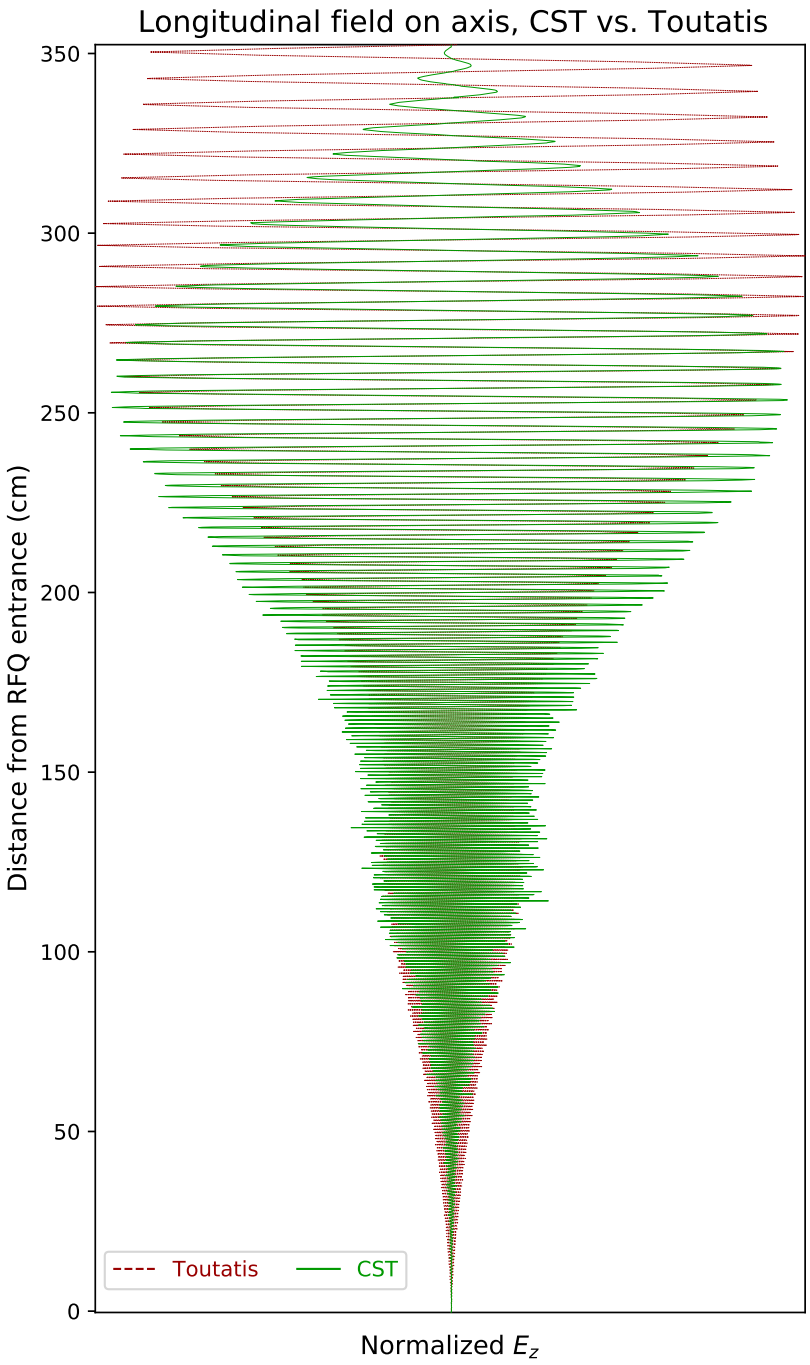

Figure 2.29. E_z on axis for the high-frequency simulation.

CHAPTER 3

ACCELERATING SECTION

3.1 Half-wave resonator principles

Superconducting accelerating cavities composed of niobium will increase the bunches' energy through three series of cavities to the final kinetic energy of 20 MeV per nucleon. The three series of cavities differ in that the first series that the beam passes through will have a peak accelerating efficiency around a relativistic beta of $\beta_1 = 0.11$ (i.e. a kinetic energy per nucleon of 5.7 MeV), the second series will have $\beta_2 = 0.19$ (i.e. a kinetic energy per nucleon of 17 MeV). This is the result of the three series of cavities having slightly different geometries. The use of three different geometries is for the purpose of attaining increased efficiency without unduly increasing the complexity of the overall design. With only one geometry of cavity, the design would be simpler, but the number of cavities required would increase. The most efficient design would of course entail a unique geometry for each cell, but that would be unnecessarily complex in terms of manufacturing cost and optimization time required. Thus, a combination of three ("low-beta," "medium-beta," and "high-beta") geometries is the most suitable choice.

Accelerating cavities can be designed in a variety of shapes depending on the particle type and energy. In my case, I used the single-spoke resonator design. The single-spoke cavity is a type of half-wave resonator. In a half-wave resonator, the electric fields in the two halves are opposite in phase. The resultant effect is that the particle bunch enters in the first half, where the field is accelerating whereas the field in the second half is decelerating, and then when the particle enters the second half, the fields have reversed in polarity so that the field is accelerating in the second half while decelerating in the first half. The excitation of the half-wave mode in a single-spoke cavity is facilitated by a spoke running in the transverse direction in the

center of the cavity; otherwise, the design is similar to that of an elliptical pillbox cavity.

3.2 Design software

As a starting point, I used a design formulated by Pal et al. in their 2021 description of single-spoke cavities for a proposed spallation research facility [16] and iterated on the design using CST Studio Suite. The authors of the aforementioned paper list geometric parameters of a 325 MHz cavity for several optimized designs, of which I used the geometrical beta $\beta_g = 0.11$ design as the basis for my designs. Since the cavity in the proposal was designed for H^- ions instead of deuterons, it needed to be optimized considerably.

In CST, I use the high-frequency project template to model and simulate my cavity. We must first choose the appropriate background and material of our model. I used a background of perfect electrical conductor (PEC) and used a material of vacuum to construct the cavity. In essence, this means I am constructing the interior of the cavity, which in reality would be indeed vacuum surrounded by superconducting niobium. Also we can choose the simulation frequency and boundaries. I used a frequency range of 0.30 GHz to 0.35 GHz as a starting point, since based on the proposal by Pal et al. the cavity is described as operating at 325 MHz with the stated design parameters. I set the boundary conditions to be zero electric field conditions in all directions. This is the expected behavior of a resonant cavity, which is bounded by a conductor in the x and y directions and is expected to have nodes along the z direction. Alternatively one can set the z boundary conditions to be zero magnetic field; this is basically equivalent.

The *Parameters* section in the interface can be used to store quantities symbolically, where they can be altered and used in calculations elsewhere in the software.

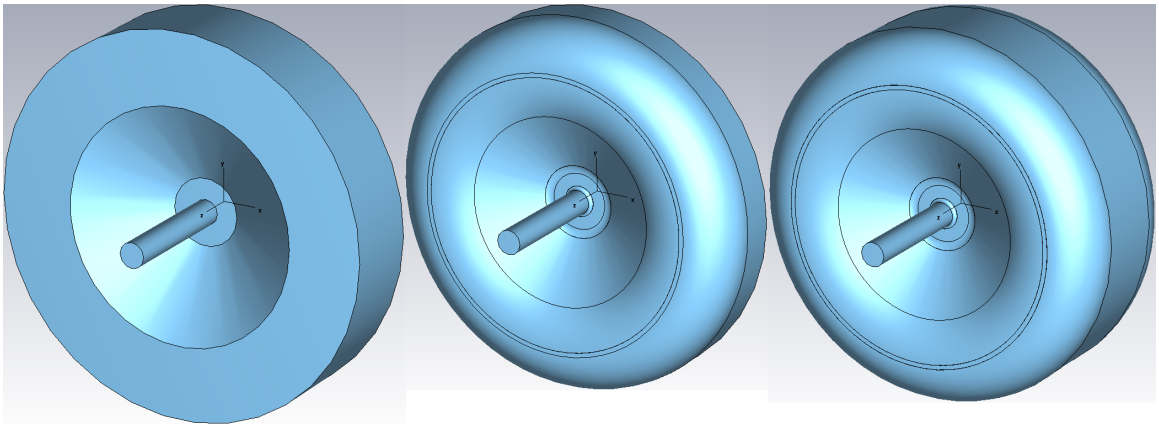

Figure 3.1. From left: the result of the rotation around the z axis of a list of points; the edges blended; the entire shape mirrored to create the pillbox.

For example, the quantity EWP (end wall position) denotes the distance between the $z = 0$ plane and the end wall of the cavity, i.e. half the width of the cavity at its widest.

To create the pillbox portion of the cavity, the *Draw Points* feature in CST can be used. The pillbox portion is rotationally symmetric about the z axis so a form can be drawn pointwise and then rotated to create the 3D shape (Figure 3.1). Next, the sharp edges are blended, and the entire pillbox is mirrored. What remains is then to subtract the spoke section from the pillbox.

The spoke is created by lofting the circular openings at the top and bottom with the racetrack aperture in the middle (Figure 3.2). After subtracting the spoke from the pillbox, the single-spoke cavity is complete.

3.3 Optimization of cavity geometry

If we consider a DC voltage gap across the length of a cavity, the amount of energy gained by an incoming particle would always be the same: the voltage difference multiplied by the particle charge. However for a time-varying field inside a cavity, the energy gain will be dependent on the particle's velocity. This dependence

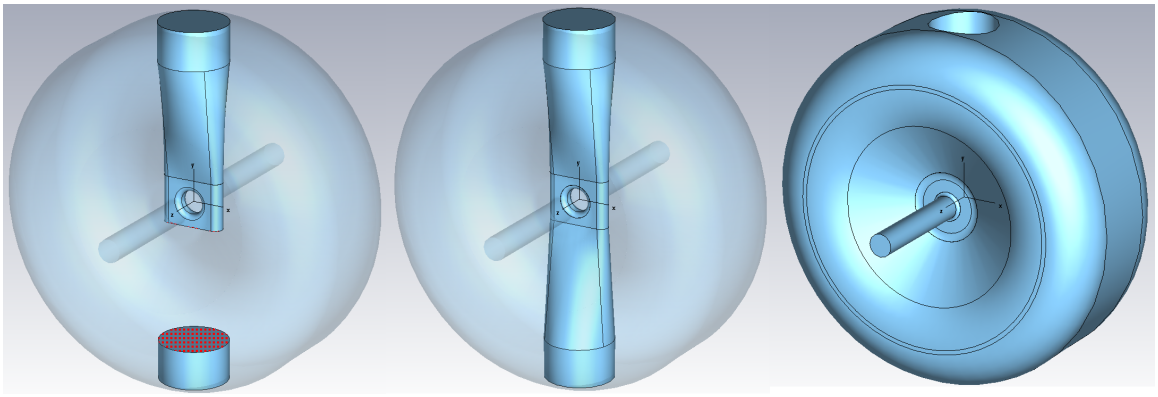

Figure 3.2. From left: the spoke is created by lofting together the top and bottom circular openings with the racetrack-shaped aperture section; the entire spoke is subtracted from the pillbox; the single-spoke cavity is complete.

is known as the "transit-time effect." [17] For a single cavity cell, the accelerating efficiency increases with relativistic beta (provided the initial velocity is greater than the length of the cavity times the cavity frequency i.e. the particle does not travel so slowly as to not make it out of the cavity before the field has switched polarity entirely). If the particle could be thought of as having infinite speed, it would have the most efficiency when traveling through the cavity when the field is maximal and accelerating. Figure F.1 shows how, above a certain velocity, the energy gain increases monotonically with higher particle velocity. However, a single-spoke cavity can be thought of a two-cell cavity, since its two halves are oppositely phased. Therefore, there exists a beta for which the energy gain throughout the entire cavity is maximal. This is because there is a trade-off between acceleration in the first half of the cell and acceleration in the second half (Figure 3.3). If the particle had infinite speed and traveled through the cavity when the field is maximal and accelerating in the first half, it would simultaneously travel through the second half when the field is maximal but decelerating, so it would in fact gain no net energy. Thus there is a particular speed at which the particle should travel through the cavity to gain the largest amount of energy.

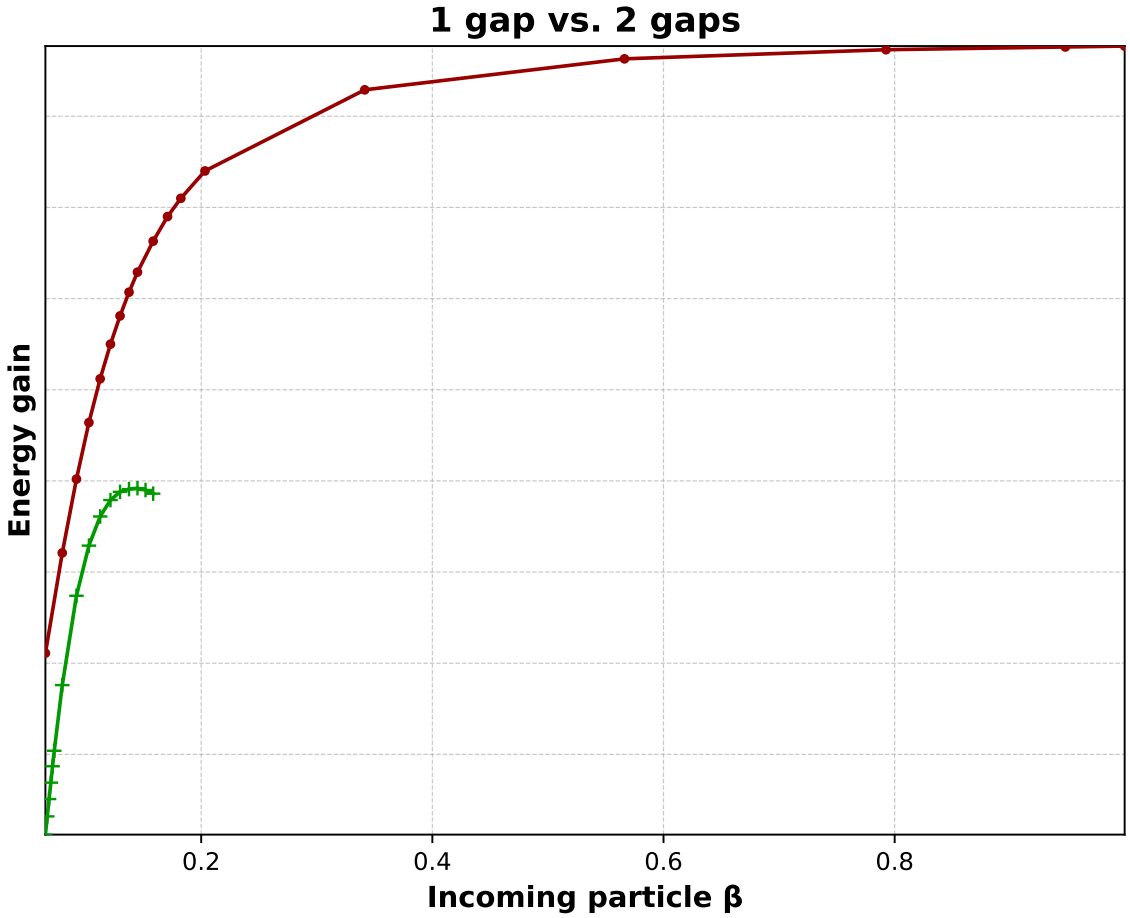

Figure 3.3. The beta curve of the first half of a two-gap cavity (red) compared with the beta curve of the entire two-gap cavity (green). The first half, containing a single RF gap, only has electric fields pointing in the same direction, while the entire cavity has its two halves opposite in phase (π mode). The result is that while a single gap will impart more energy to a particle the faster the particle travels, a two-gap cavity will have a speed at which the energy gain is maximal.

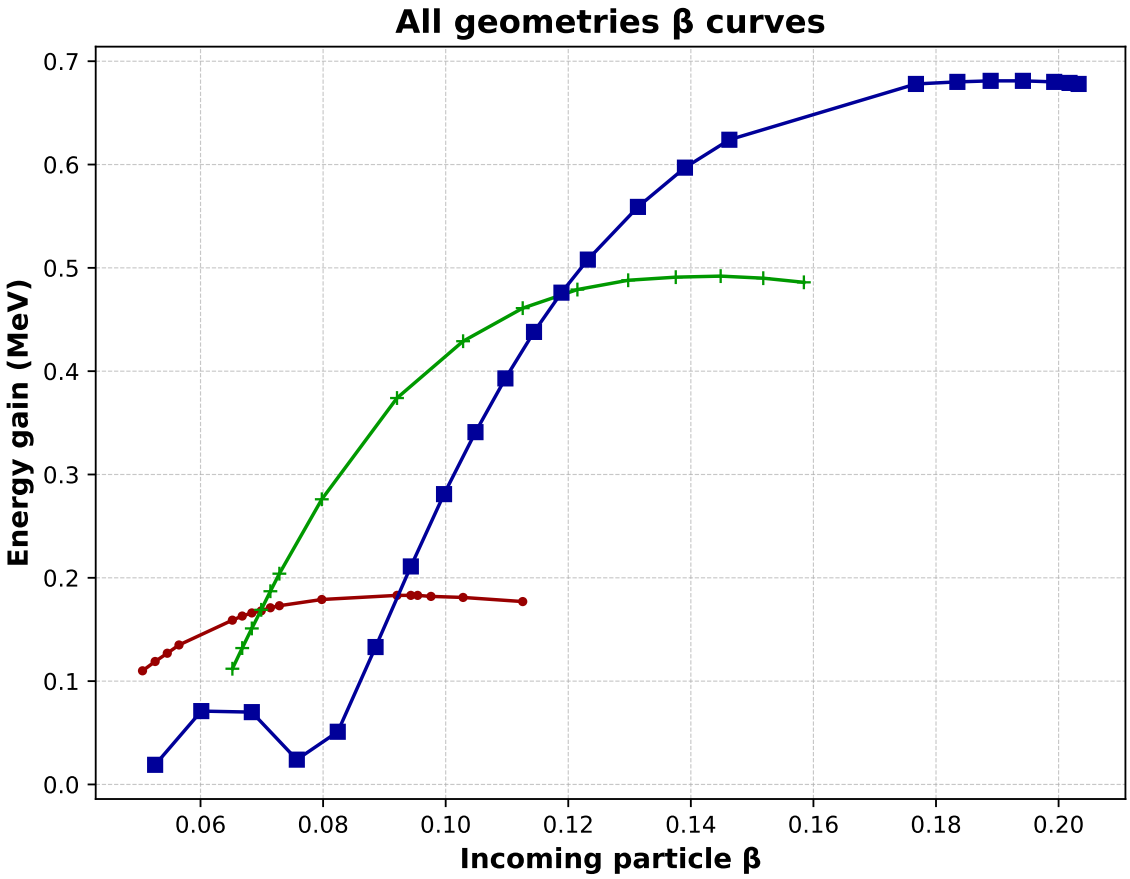

Figure 3.4. Combined beta curves for the three geometries. The intersections of the low-beta (red circles) and medium-beta (green crosses) curves and the medium-beta and high-beta (blue squares) curves are the two places where the geometries switch in the accelerating section, so that the geometry used is always the one with the highest energy gain for that beta.

This is all to say that a cell geometry that is efficient for low speeds may not be efficient for high speeds. For this reason, three geometries were used in the accelerating section. This reduces the number of cavities needed, and the overall length, compared to using only one or two geometries.

Table 3.1. Optimization of Q factor and fine-tuning frequency for the low-β cavity using the geometric parameters RW, EWP, and IOR. The peak surface electric field, peak surface magnetic field, resonant frequency, and cavity Q are displayed as calculated by CST simulation. The final row shows the result of having achieved the resonant frequency to within 100 kHz while having recovered a significant amount of Q factor.

RW	EWP	IOR	E_{Max} (MV/m)	H_{Max} (A/m)	f (MHz)	Q
100	60	180	28.9	142000	427.027	3961.45
200	60	180	23.1	145000	381.657	3757.84
300	60	180	22.3	143000	355.339	3673.24
100	80	140	31.5	39325	310.57	8300.25
100	80	156.48	31.5343	47865.2	325.047	7402.91

Table 3.2. Fine-tuning the high-β cavity for the desired resonant frequency of 325 MHz. Also shown is the number of tetrahedrons used in the CST simulations for each set of geometric parameters. In this case the results were achieved by only changing the IOR, due to a favorable set of values of peak surface fields and Q factor to begin with.

IOR	E_{Max} (MV/m)	H_{Max} (A/m)	f (MHz)	Q	tetrahedrons
150	16.5878	20048	321.279	15532.9	272931
163.5	16.8526	20929	325.055	15045.6	271902
163.49	16.9578	20938	325.052	15038	297360

In optimizing the cell geometries to create the most efficient cavity, the goals in mind were to minimize the peak electric field on the surface of the cavity and to maximize the $\frac{r}{Q}$ parameter. To minimize the peak surface field, I varied several parameters one by one and plotted the peak surface electric field as well as the resonant frequency (Figure 3.5). The reason for plotting the resonant frequency was

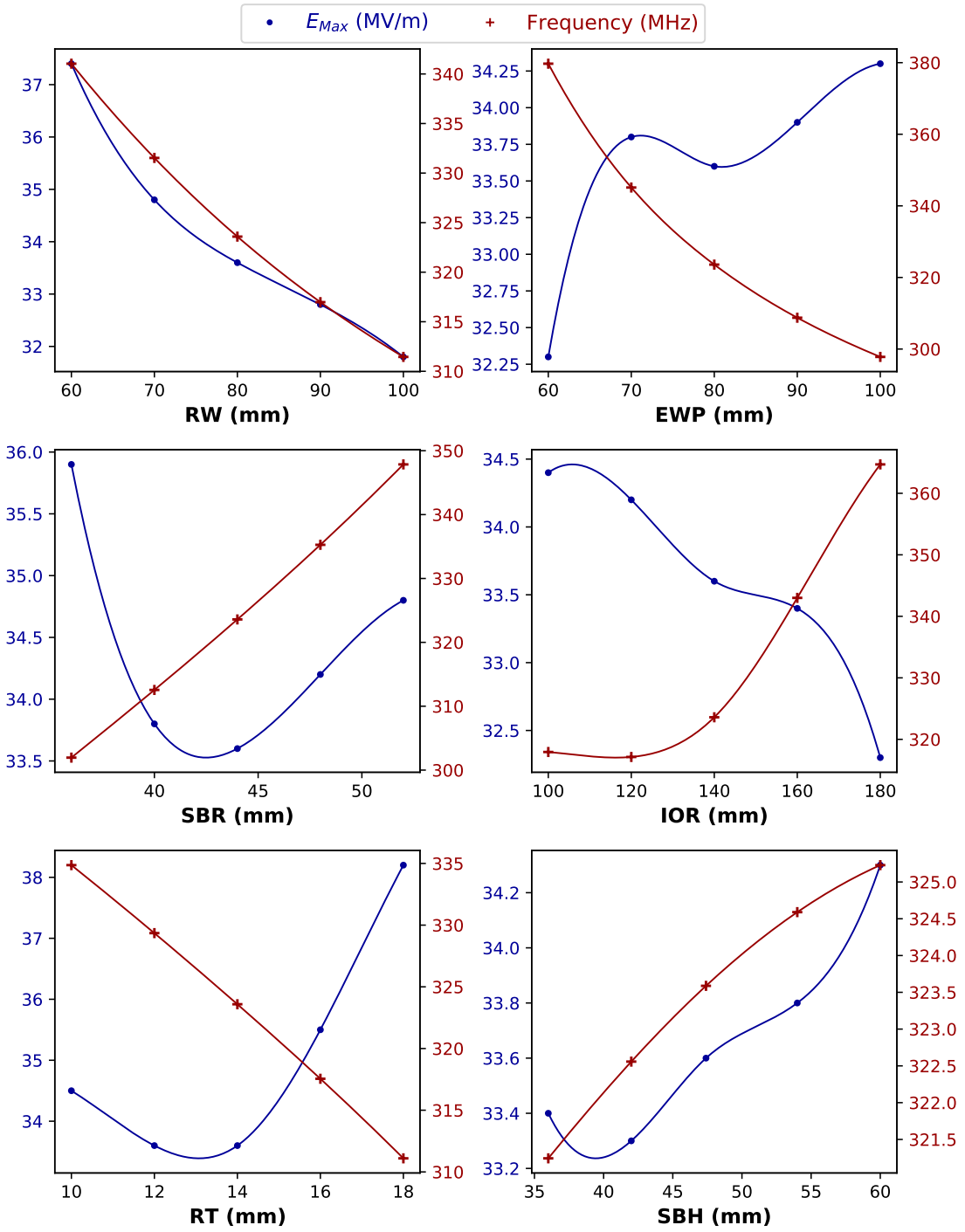

Figure 3.5. The peak surface electric field and resonant frequency for different values of certain parameters. The physical meanings of the parameters are depicted in the next two figures.

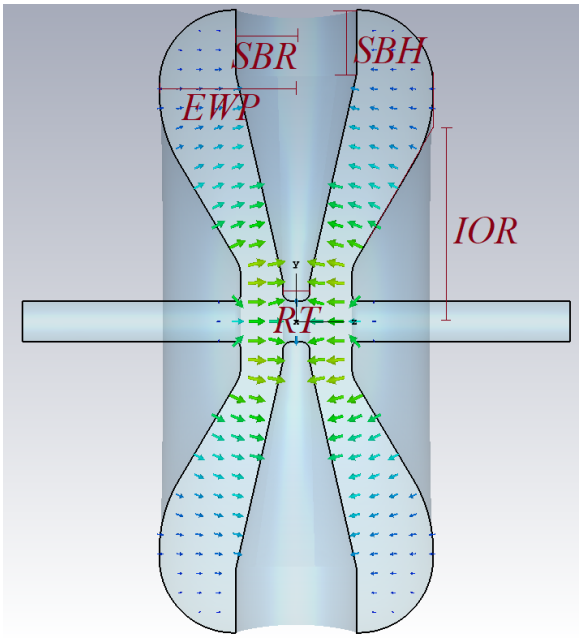

Figure 3.6. Some of the geometric parameters used in the optimization process: he spoke base radius (SBR), the spoke base height (SBH), the end wall position (EWP), the iris outer radius (IOR), and the racetrack thickness (RT).

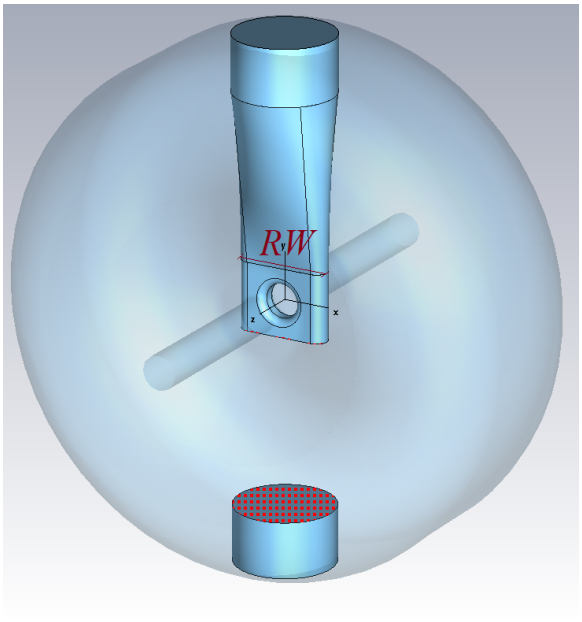

Figure 3.7. One of the geometric parameters used in the optimization process, the racetrack width (RW).

that the cavity needs to be resonant at 325 MHz, so plotting this quantity will tell me which quantities I can adjust and in which direction to tune the cavity back to resonance after I have adjusted some parameters to minimize the peak surface field. For example, increasing the quantity RW (racetrack width) both decreases the peak surface field and the resonant frequency, while increasing the quantity IOR (iris outer radius) decreases the peak surface field but increases the resonant frequency. Therefore, increasing both quantities at once could serve to reduce the peak surface field while simultaneously preserving the resonant frequency or at least changing it much less. On the contrary, the quantity SBR (spoke base radius) can be seen to have an effect on the resonant frequency that is outsized in comparison to its effect on the peak surface fields. Therefore this quantity can be used to adjust the resonant frequency as a final step.

Reducing the peak surface fields may come at a disproportionate cost to the geometric efficiency of the cavity. For example, we can see from Table 3.1 that while using a certain set of parameters can reduce the peak surface greatly, it also greatly reduces the Q factor of the cavity. Thus the best method is to strike somewhat of a balance between a low peak surface field and a high Q factor. It may be noted that a single-spoke cavity will have a lower Q factor than a comparably sized pillbox cavity, due to the extra surface area added by the spoke. The final resonant frequency should fall within 0.5 MHz of the design frequency, which was achieved in both the lower- and higher-beta cavities. The medium-beta cavity, having been reverse-engineered from the design specified in the proposal for the Indian Facility for Spallation Research, was already resonant at 325 MHz [16].

3.4 Cavity beam simulations

In order to actually see the cavity's properties like the peaks surface electric and magnetic fields and the Q factor, the cavity can be simulated in CST using the

eigenmode solver. The mesh properties can be viewed and changed in the *Global Properties* menu in the *Simulation* tab. Here, the mesh should be set to contain at least 250,000 tetrahedrons. This ensures a high enough precision for the simulation without requiring unnecessary amounts of time to simulate. The number of tetrahedrons will appear in the bottom-right of the screen when the simulation nears completion. If it is too low, the simulation will need to be restarted and the mesh regenerated with a higher number of cells. For instance, in the case of the final model for the low-beta cavity, I used 44 and 50 cells per max model box edge in the model and background respectively. This generated a mesh of 274,632 tetrahedrons.

After running the eigenmode solver, CST displays a 3D arrow-plot of the electric field in the *2D/3D Results* section of the *Navigation Tree*. It can be checked that the correct mode is being modeled by using the *Cutting plane* and *Fields on Plane* tools in the *2D/3D Plot* tab on the top toolbar. Using a cutting plane normal to the x axis, the fields should be opposite in polarity among the two halves of the cell. Otherwise, the mode shown is not the desired fundamental TEM mode. The scale on the right side of the display can be used to infer the maximum surface electric field, with the largest value displayed closely corresponding to the peak surface field. The precise value of the peak electric field on the surface of the cavity can be shown by selecting a surface chain containing any surface of the cavity and prompting the software to evaluate the maximum absolute value of the complex electric field on the selection via the *Post-Processing* tab; similar steps can be followed for the magnetic field on the cavity surface.

In the same *Results Templates* interface, the user can find calculations for the $\frac{r}{Q}$ value, a figure of merit for accelerating cavities. This is located in *3D Eigenmode Result* from the second drop-down menu. With this calculation, the user should check the *consider part. velocity* checkbox and enter the geometric beta of the cavity to see

the $\frac{r}{Q}$ for the design beta. The direction of integration should be chosen to be along the particle trajectory axis, in our case the z axis.

The energy gain was modeled using TRACK [18]. Using the electric field in the *2D/3D Results* section of the *Navigation Tree*, we can export the field by using the *Import/Export* tool in the *Post-Processing* tab as *Plot Data (ASCII)....* In the ensuing interface, we designate a subvolume (Figure 3.8), as we did in the RFQ case, and export the field using 25 points in the x and y directions and 201 points in the z direction. This allows us to easily use TRACK to see the energy gain. Now we must convert the file to the TRACK format. Using some Python code, I reformat the CST output file into the desired TRACK format. The most critical difference is the re-indexing of the variables to iterate first by z, then y, then x, as opposed to x, then y, then z as CST does. Also, the appropriate preamble must be generated for TRACK to function correctly, which includes the grid parameters (numbers of points and sizes). Once the TRACK field file has been generated, the appropriate *track.dat* and *sclinac.dat* files can be created to simulate a single cell. In the *track.dat* file, the initial energy of the particle bunch can be altered to see what the energy gain is at different beta. These results can be plotted to determine the geometric beta of the cell.

In total, 7 low-beta cavities, 13 medium-beta cavities, and 21 high-beta cavities accelerate the incoming bunch from 1.3 MeV/u to 20 MeV/u. The energy gain in each cavity can be seen in Tables 3.3 and 3.4.

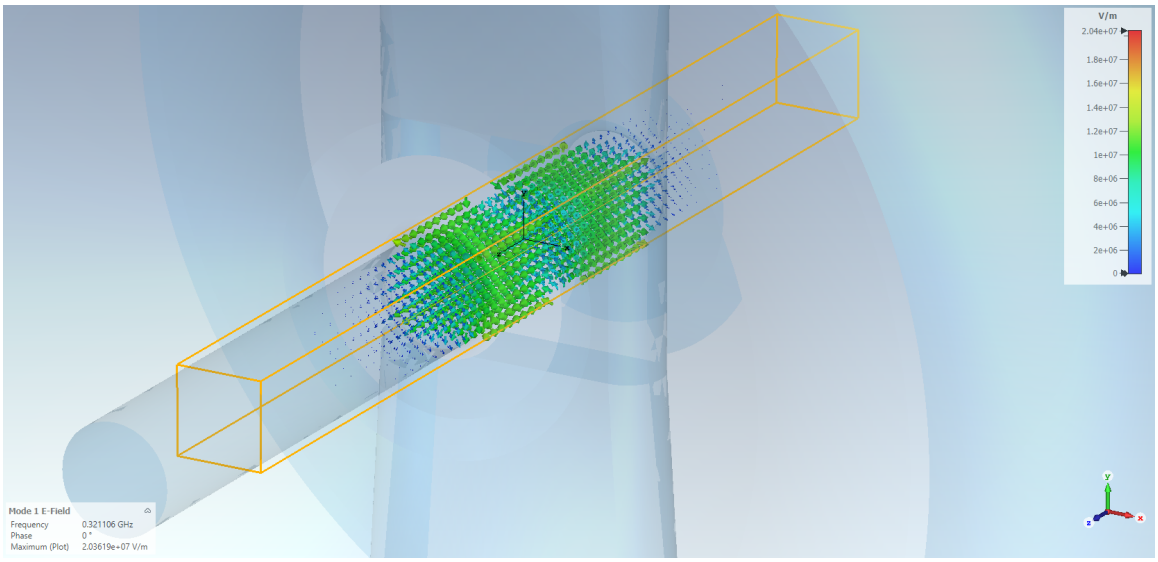

Figure 3.8. Exporting a subvolume of the cavity for TRACK simulation, shown with the medium-beta cavity.

Table 3.3. Table of energy gains for the first 20 cavities, comprising all the low- and medium-beta geometry cavities. The geometry switches at the point where the left and middle curves intersect in Figure 3.4.

Incoming energy (MeV)	Incoming beta	Energy gain (MeV)	Outgoing energy (MeV)	Outgoing beta	Cavity geometry	Cavity number
1.300	0.053	0.119	1.419	0.055	low-beta	1
1.419	0.055	0.129	1.548	0.057	low-beta	2
1.548	0.057	0.138	1.686	0.060	low-beta	3
1.686	0.060	0.146	1.832	0.062	low-beta	4
1.832	0.062	0.153	1.985	0.065	low-beta	5
1.985	0.065	0.159	2.144	0.067	low-beta	6
2.144	0.067	0.164	2.308	0.070	low-beta	7
2.308	0.070	0.171	2.479	0.073	medium-beta	8
2.479	0.073	0.200	2.679	0.075	medium-beta	9
2.679	0.075	0.232	2.911	0.079	medium-beta	10
2.911	0.079	0.265	3.176	0.082	medium-beta	11
3.176	0.082	0.298	3.474	0.086	medium-beta	12
3.474	0.086	0.329	3.803	0.090	medium-beta	13
3.803	0.090	0.359	4.162	0.094	medium-beta	14
4.162	0.094	0.385	4.547	0.098	medium-beta	15
4.547	0.098	0.408	4.955	0.102	medium-beta	16
4.955	0.102	0.427	5.382	0.107	medium-beta	17
5.382	0.107	0.443	5.825	0.111	medium-beta	18
5.825	0.111	0.457	6.282	0.115	medium-beta	19
6.282	0.115	0.467	6.749	0.119	medium-beta	20

Table 3.4. Table of energy gains for the next 21 cavities, comprising all of the high-beta geometry cavities. The geometry switches at the point where the middle and right curves intersect in Figure 3.4.

Incoming energy (MeV)	Incoming beta	Energy gain (MeV)	Outgoing energy (MeV)	Outgoing beta	Cavity geometry	Cavity number
6.749	0.119	0.479	7.228	0.123	high-beta	21
7.228	0.123	0.510	7.738	0.128	high-beta	22
7.738	0.128	0.538	8.276	0.132	high-beta	23
8.276	0.132	0.563	8.839	0.136	high-beta	24
8.839	0.136	0.584	9.423	0.141	high-beta	25
9.423	0.141	0.603	10.026	0.145	high-beta	26
10.026	0.145	0.620	10.646	0.149	high-beta	27
10.646	0.149	0.633	11.279	0.154	high-beta	28
11.279	0.154	0.645	11.924	0.158	high-beta	29
11.924	0.158	0.654	12.578	0.162	high-beta	30
12.578	0.162	0.662	13.240	0.166	high-beta	31
13.240	0.166	0.668	13.908	0.170	high-beta	32
13.908	0.170	0.672	14.580	0.174	high-beta	33
14.580	0.174	0.676	15.256	0.178	high-beta	34
15.256	0.178	0.678	15.934	0.182	high-beta	35
15.934	0.182	0.680	16.614	0.186	high-beta	36
16.614	0.186	0.681	17.295	0.189	high-beta	37
17.295	0.189	0.681	17.976	0.193	high-beta	38
17.976	0.193	0.681	18.657	0.197	high-beta	39
18.657	0.197	0.680	19.337	0.200	high-beta	40
19.337	0.200	0.679	20.016	0.203	high-beta	41

CHAPTER 4

CONCLUSION

Using the CEA DACM software RFQ Designer, I was able to generate a deuteron RFQ at 162.5 MHz with high (94.20%) transmission within 2.5% of the design energy (1.3 MeV/u), for incoming beams with parameters appropriate for existing RFQ linacs [3]. The design was simulated using the CEA DACM software Toutatis and confirmed using the electrostatic solver of CST Studio Suite 2022. This showed the viability of converting an RFQ Designer output file into 3D modeled vanetips using Python and VBA. Superconducting accelerating cavities of the single-spoke type were adapted from a design proposed for the Indian Facility for Spallation Research [16] into lower geometric beta and higher geometric beta configurations. The designs were optimized along several geometric variables to reduce the peak surface fields while sacrificing as little Q factor as possible, while maintaining resonant frequency at 325 MHz. The energy gains of these cavities were simulated using the Argonne National Lab code TRACK, enabling me to calculate the peak betas of these cavities and find the optimal series of cavities for maximizing energy gain towards the goal of 20 MeV/u.

APPENDIX A

SCREENSHOTS OF TOUTATIS INTERFACES

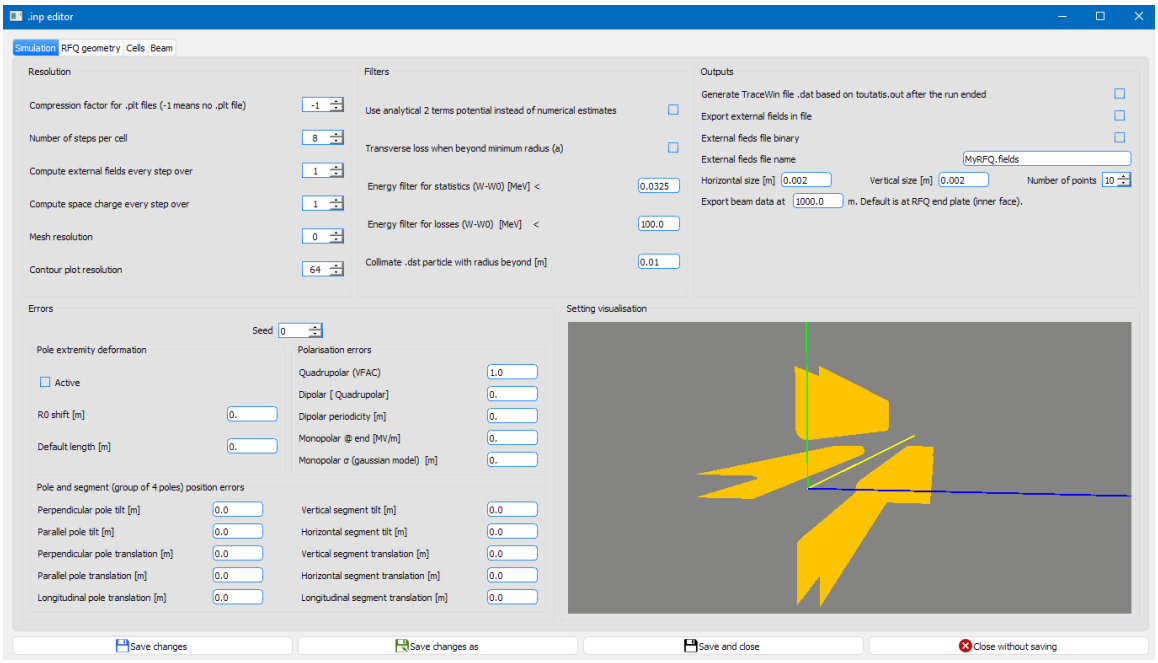

Figure A.1. A screenshot of the "Simulation" tab in Toutatis.

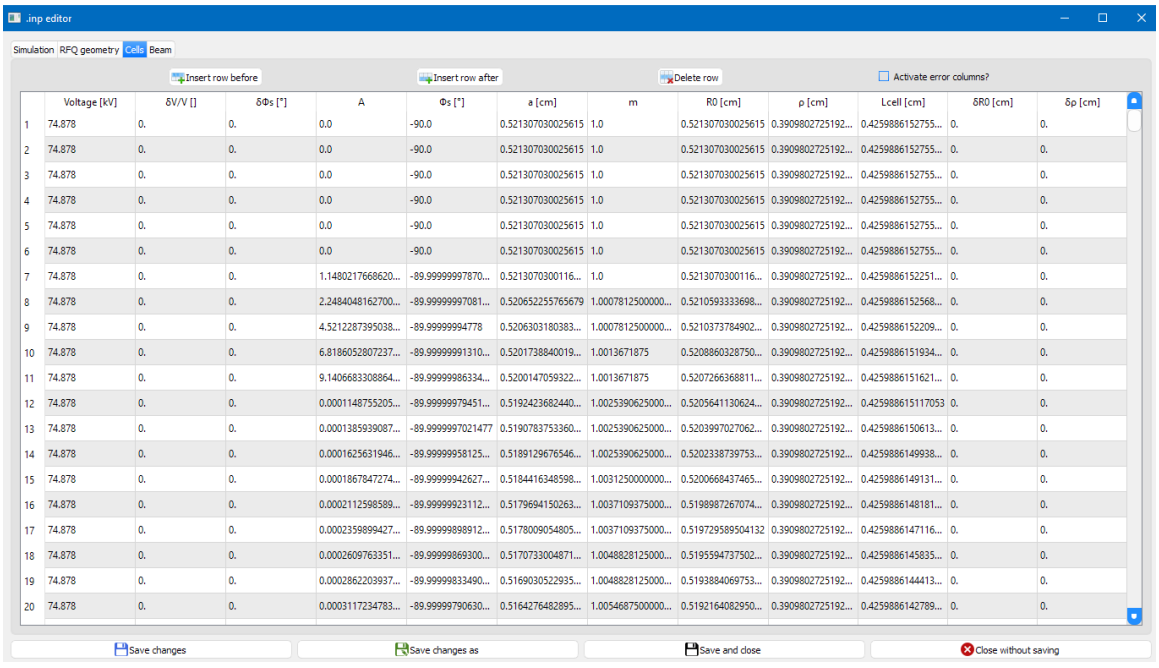

	Voltage [kV]	δV/V []	δΦs [°]	A	Φs [°]	a [cm]	m	R0 [cm]	ρ [cm]	Lcell [cm]	δR0 [cm]	δρ [cm]
1	74.878	0.	0.	0.0	-90.0	0.521307030025615	1.0	0.521307030025615	0.3909802725192...	0.4259886152755...	0.	0.
2	74.878	0.	0.	0.0	-90.0	0.521307030025615	1.0	0.521307030025615	0.3909802725192...	0.4259886152755...	0.	0.
3	74.878	0.	0.	0.0	-90.0	0.521307030025615	1.0	0.521307030025615	0.3909802725192...	0.4259886152755...	0.	0.
4	74.878	0.	0.	0.0	-90.0	0.521307030025615	1.0	0.521307030025615	0.3909802725192...	0.4259886152755...	0.	0.
5	74.878	0.	0.	0.0	-90.0	0.521307030025615	1.0	0.521307030025615	0.3909802725192...	0.4259886152755...	0.	0.
6	74.878	0.	0.	0.0	-90.0	0.521307030025615	1.0	0.521307030025615	0.3909802725192...	0.4259886152755...	0.	0.
7	74.878	0.	0.	1.1480217668620...	-89.99999997870...	0.5213070300116...	1.0	0.5213070300116...	0.3909802725192...	0.4259886152251...	0.	0.
8	74.878	0.	0.	2.2484048162700...	-89.99999997081...	0.520652255765679	1.0007812500000...	0.5210593333698...	0.3909802725192...	0.4259886152568...	0.	0.
9	74.878	0.	0.	4.5212287395038...	-89.99999994778	0.5206303180383...	1.0007812500000...	0.5210373784902...	0.3909802725192...	0.4259886152209...	0.	0.
10	74.878	0.	0.	6.8186052807237...	-89.99999991310...	0.5201738840019...	1.0013671875	0.5208860328750...	0.3909802725192...	0.4259886151934...	0.	0.
11	74.878	0.	0.	9.1406683308864...	-89.99999986334...	0.5200147059322...	1.0013671875	0.5207266368811...	0.3909802725192...	0.4259886151621...	0.	0.
12	74.878	0.	0.	0.0001148755205...	-89.99999979451...	0.5192423682440...	1.0025390625000...	0.5205641130624...	0.3909802725192...	0.4259886151170 53	0.	0.
13	74.878	0.	0.	0.0001385939087...	-89.9999997021477	0.5190783753360...	1.0025390625000...	0.5203997027062...	0.3909802725192...	0.4259886150613...	0.	0.
14	74.878	0.	0.	0.0001625631946...	-89.99999958125...	0.5189129676546...	1.0025390625000...	0.5202338739753...	0.3909802725192...	0.4259886149938...	0.	0.
15	74.878	0.	0.	0.0001867847274...	-89.99999942627...	0.5184416348598...	1.0031250000000...	0.5200668437465...	0.3909802725192...	0.4259886149131...	0.	0.
16	74.878	0.	0.	0.0002112598589...	-89.99999923112...	0.5179694150263...	1.0037109375000...	0.5198987267074...	0.3909802725192...	0.4259886148181...	0.	0.
17	74.878	0.	0.	0.0002359899427...	-89.99999898912...	0.5178009054805...	1.0037109375000...	0.5197295895041 32	0.3909802725192...	0.4259886147116...	0.	0.
18	74.878	0.	0.	0.0002609763351...	-89.99999869300...	0.5170733004871...	1.0048828125000...	0.5195594737502...	0.3909802725192...	0.4259886145835...	0.	0.
19	74.878	0.	0.	0.0002862203937...	-89.99999833490...	0.5169030522935...	1.0048828125000...	0.5193884069753...	0.3909802725192...	0.4259886144413...	0.	0.
20	74.878	0.	0.	0.0003117234783...	-89.99999790630...	0.5164276482895...	1.0054687500000...	0.5192164082950...	0.3909802725192...	0.4259886142789...	0.	0.

Figure A.2. A screenshot of the "Cells" tab in Toutatis.

APPENDIX B

VBA MACRO USED FOR GENERATION OF RFQ CELLS IN CST STUDIO

```
Sub Main ()

For I = 498 To 0 STEP -2

        '## y vanetip, moving in:
        With AnalyticalFace
             .Reset
             .Name "solid1"
             .Component "component1"
             .Material "PEC"
             .LawX "u"
             .LawY "a" & CStr(I+1) & "*(((a" & CStr(I) & "/a" & CStr(I
                +1) & ")*m" & CStr(I) & "-1)/2 * (1 + cos((pi*(v-
                zoffset" & CStr(I) & "))/lcell" & CStr(I) & "))+1) -
                sqrt(rho^2 - u^2) + rho"
             .LawZ "v"
             .ParameterRangeU "-rho", "rho"
             .ParameterRangeV "zoffset" & CStr(I) & "", "zoffset" & CStr
                (I) & "+lcell" & CStr(I) & ""
             .Create
        End With

        '## y vanebody, moving in:
        With AnalyticalFace
             .Reset
             .Name "solid2"
             .Component "component1"
             .Material "PEC"
             .LawX "u"
             .LawY "rho + vane_rad"
             .LawZ "v"
             .ParameterRangeU "-rho", "rho"
```

```
     .ParameterRangeV "zoffset" & CStr(I) & "", "zoffset" & CStr
        (I) & "+lcell" & CStr(I) & ""
     .Create
End With

'## Merged Block - pick face
Pick.PickFaceFromId "component1:solid2", "1"

'## Merged Block - pick face
Pick.PickFaceFromId "component1:solid1", "1"

'## Merged Block - define loft: component1:
With Loft
     .Reset
     .Name "cell" & CStr(I) & ""
     .Component "component1"
     .Material "PEC"
     .Tangency "0.000000"
     .Minimizetwist "true"
     .CreateNew
End With

'## Merged Block - clear picks
Pick.ClearAllPicks

'## y vanetip, moving out:
With AnalyticalFace
     .Reset
     .Name "solid4"
     .Component "component1"
     .Material "PEC"
     .LawX "u"
```

```
        .LawY "a" & CStr(I+1) & "*(((a" & CStr(I+2) & "/a" & CStr(I
           +1) & ")*m" & CStr(I+2) & "-1)/2 * (1 - cos((pi*(v-
           zoffset" & CStr(I+1) & "))/lcell" & CStr(I+1) & "))+1)
           - sqrt(rho^2 - u^2) + rho"
        .LawZ "v"
        .ParameterRangeU "-rho", "rho"
        .ParameterRangeV "zoffset" & CStr(I+1) & "", "zoffset" &
           CStr(I+1) & "+lcell" & CStr(I+1) & ""
        .Create
End With

'## y vanebody, moving out:
With AnalyticalFace
        .Reset
        .Name "solid5"
        .Component "component1"
        .Material "PEC"
        .LawX "u"
        .LawY "rho + vane_rad"
        .LawZ "v"
        .ParameterRangeU "-rho", "rho"
        .ParameterRangeV "zoffset" & CStr(I+1) & "", "zoffset" &
           CStr(I+1) & "+lcell" & CStr(I+1) & ""
        .Create
End With

'## Merged Block - clear picks
Pick.ClearAllPicks

'## Merged Block - pick face
Pick.PickFaceFromId "component1:solid5", "1"
```

```
'## Merged Block - pick face
Pick.PickFaceFromId "component1:solid4", "1"

'## Merged Block - define loft: component1:
With Loft
     .Reset
     .Name "cell" & CStr(I+1) & ""
     .Component "component1"
     .Material "PEC"
     .Tangency "0.0"
     .Minimizetwist "true"
     .CreateNew
End With

'## Merged Block - delete shapes
Solid.Delete "component1:solid1"
Solid.Delete "component1:solid2"
Solid.Delete "component1:solid4"
Solid.Delete "component1:solid5"

'## Create vanes in orthogonal direction

'## x vanetip, moving out

With AnalyticalFace
     .Reset
     .Name "solid1"
     .Component "component1"
     .Material "PEC"
     .LawX "a" & CStr(I) & "*(((a" & CStr(I+1) & "/a" & CStr(I)
        & ")*m" & CStr(I+1) & "-1)/2 * (1 - cos((pi*(v-zoffset"
         & CStr(I) & "))/lcell" & CStr(I) & "))+1) - sqrt(rho^2
```

```
          - u^2) + rho"
     .LawY "u"
     .LawZ "v"
     .ParameterRangeU "-rho", "rho"
     .ParameterRangeV "zoffset" & CStr(I) & "", "zoffset" & CStr
        (I) & "+lcell" & CStr(I) & ""
     .Create
End With

'## x vanebody, moving out
With AnalyticalFace
     .Reset
     .Name "solid2"
     .Component "component1"
     .Material "PEC"
     .LawX "rho + vane_rad"
     .LawY "u"
     .LawZ "v"
     .ParameterRangeU "-rho", "rho"
     .ParameterRangeV "zoffset" & CStr(I) & "", "zoffset" & CStr
        (I) & "+lcell" & CStr(I) & ""
     .Create
End With

'## Merged Block - pick face
Pick.PickFaceFromId "component1:solid2", "1"

'## Merged Block - pick face
Pick.PickFaceFromId "component1:solid1", "1"

'## Merged Block - define loft: component1:
With Loft
```

```
        .Reset
        .Name "cell" & CStr(I) & "o"
        .Component "component1"
        .Material "PEC"
        .Tangency "0.000000"
        .Minimizetwist "true"
        .CreateNew
End With

'## Merged Block - clear picks
Pick.ClearAllPicks

'## x vanetip, moving in
With AnalyticalFace
        .Reset
        .Name "solid4"
        .Component "component1"
        .Material "PEC"
        .LawX "a" & CStr(I+2) & "*(((a" & CStr(I+1) & "/a" & CStr(I
           +2) & ")*m" & CStr(I+1) & "-1)/2 * (1 + cos((pi*(v-
           zoffset" & CStr(I+1) & "))/lcell" & CStr(I+1) & "))+1)
           - sqrt(rho^2 - u^2) + rho"
        .LawY "u"
        .LawZ "v"
        .ParameterRangeU "-rho", "rho"
        .ParameterRangeV "zoffset" & CStr(I+1) & "", "zoffset" &
           CStr(I+1) & "+lcell" & CStr(I+1) & ""
        .Create
End With

'## x vanebody, moving in
With AnalyticalFace
```

```
     .Reset
     .Name "solid5"
     .Component "component1"
     .Material "PEC"
     .LawX "rho + vane_rad"
     .LawY "u"
     .LawZ "v"
     .ParameterRangeU "-rho", "rho"
     .ParameterRangeV "zoffset" & CStr(I+1) & "", "zoffset" &
        CStr(I+1) & "+lcell" & CStr(I+1) & ""
     .Create
End With

'## Merged Block - clear picks
Pick.ClearAllPicks

'## Merged Block - pick face
Pick.PickFaceFromId "component1:solid5", "1"

'## Merged Block - pick face
Pick.PickFaceFromId "component1:solid4", "1"

'## Merged Block - define loft: component1:
With Loft
     .Reset
     .Name "cell" & CStr(I+1) & "o"
     .Component "component1"
     .Material "PEC"
     .Tangency "0.0"
     .Minimizetwist "true"
     .CreateNew
End With
```

```
        '## Merged Block - delete shapes
        Solid.Delete "component1:solid1"
        Solid.Delete "component1:solid2"
        Solid.Delete "component1:solid4"
        Solid.Delete "component1:solid5"


Next I
End Sub
```

APPENDIX C

DETAILS OF RFQ MODELS FROM CST STUDIO SUITE

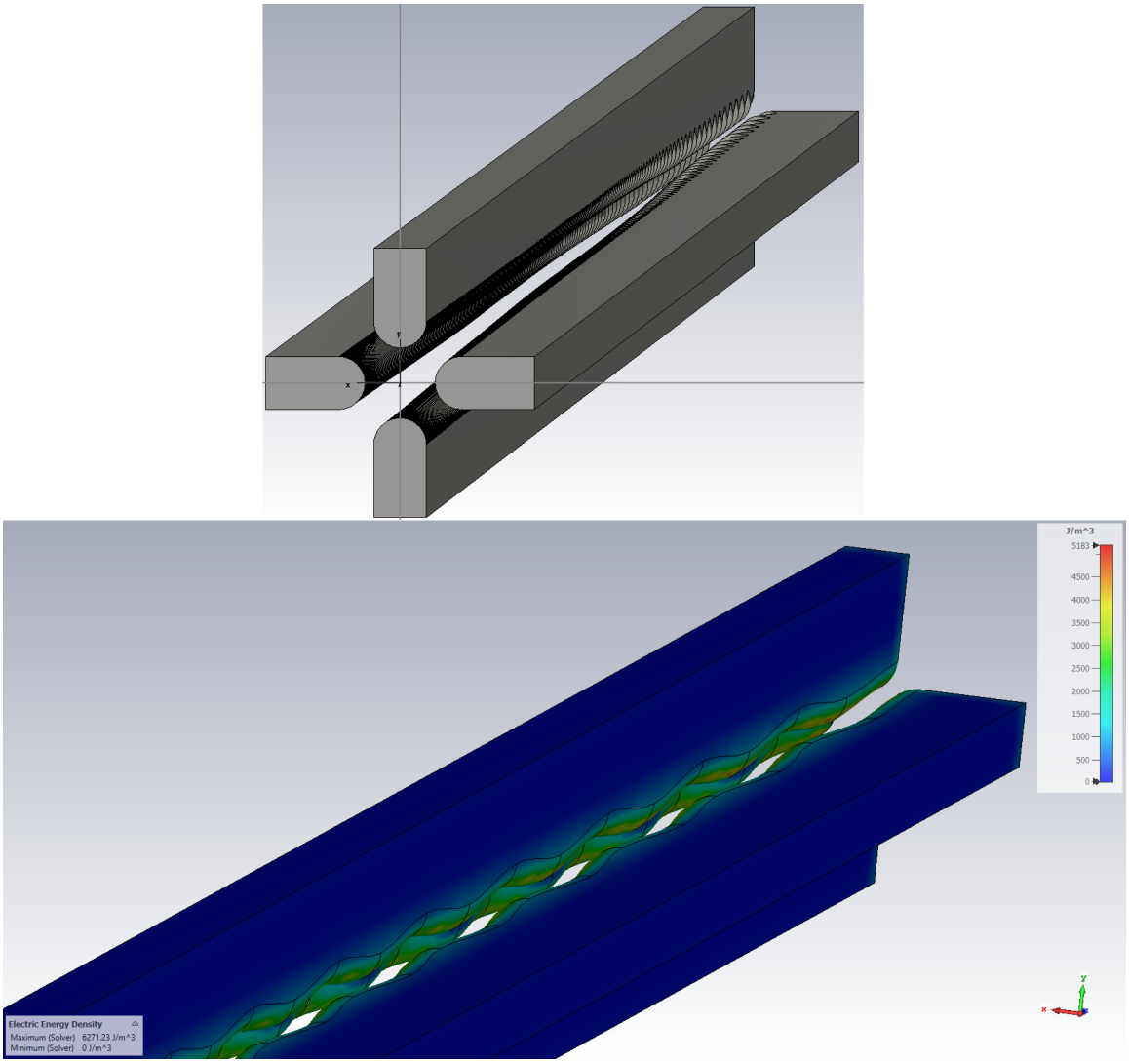

Figure C.1. Top: full RFQ 3D model in the electrostatic solver. Bottom: energy density near the exit. The peak energy density on the RFQ is 6271.23 $\mathrm{J/m^3}$.

APPENDIX D

DETAIL OF CAVITY MODELS FROM CST STUDIO SUITE

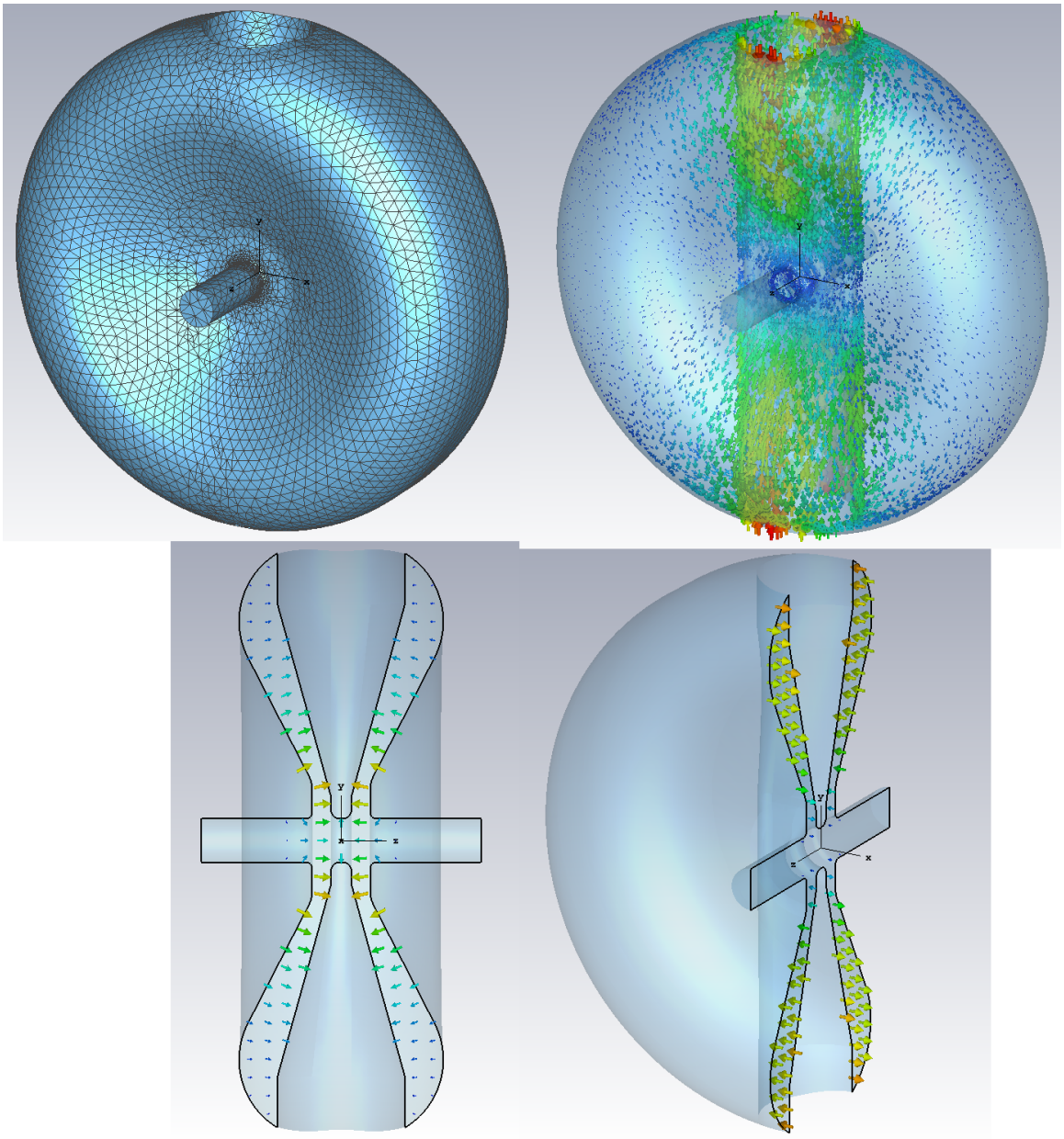

Figure D.1. Detail of low-beta cavity in CST. Top-left: 274,632 tetrahedrons mesh. Top-right: Peak surface currents, occurring at $\frac{n\pi}{2}$ phase. The resonant frequency is 325.047 MHz and the maximum surface current on the cavity is 48 kA/m (red, near the top and bottom). Bottom-left: yz plane cutaway showing the peak electric fields, occurring at $n\pi$ phase. Bottom-right: yz plane cutaway showing the peak H-fields, occurring at $\frac{n\pi}{2}$ phase.

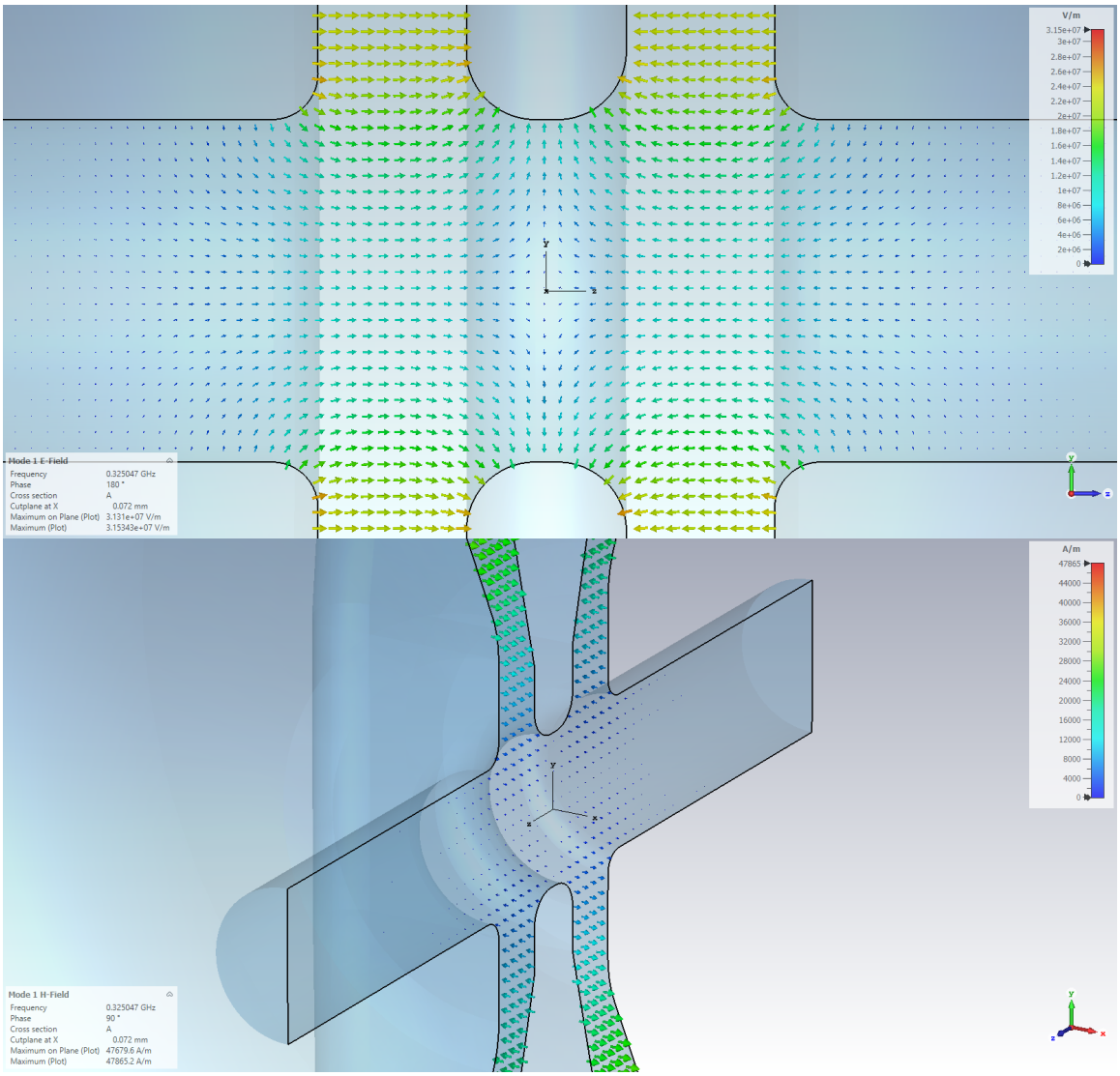

Figure D.2. Low-beta cavity close-up of electric (top) and magnetic (bottom) fields at peaks on yz plane. The maximum electric field on the cavity is 31.5 MV/m and the maximum H-field on the cavity is 48 kA/m, corresponding to the maximum surface current. Both the maximum electric and maximum magnetic fields occur outside of the depicted cutaway plane.

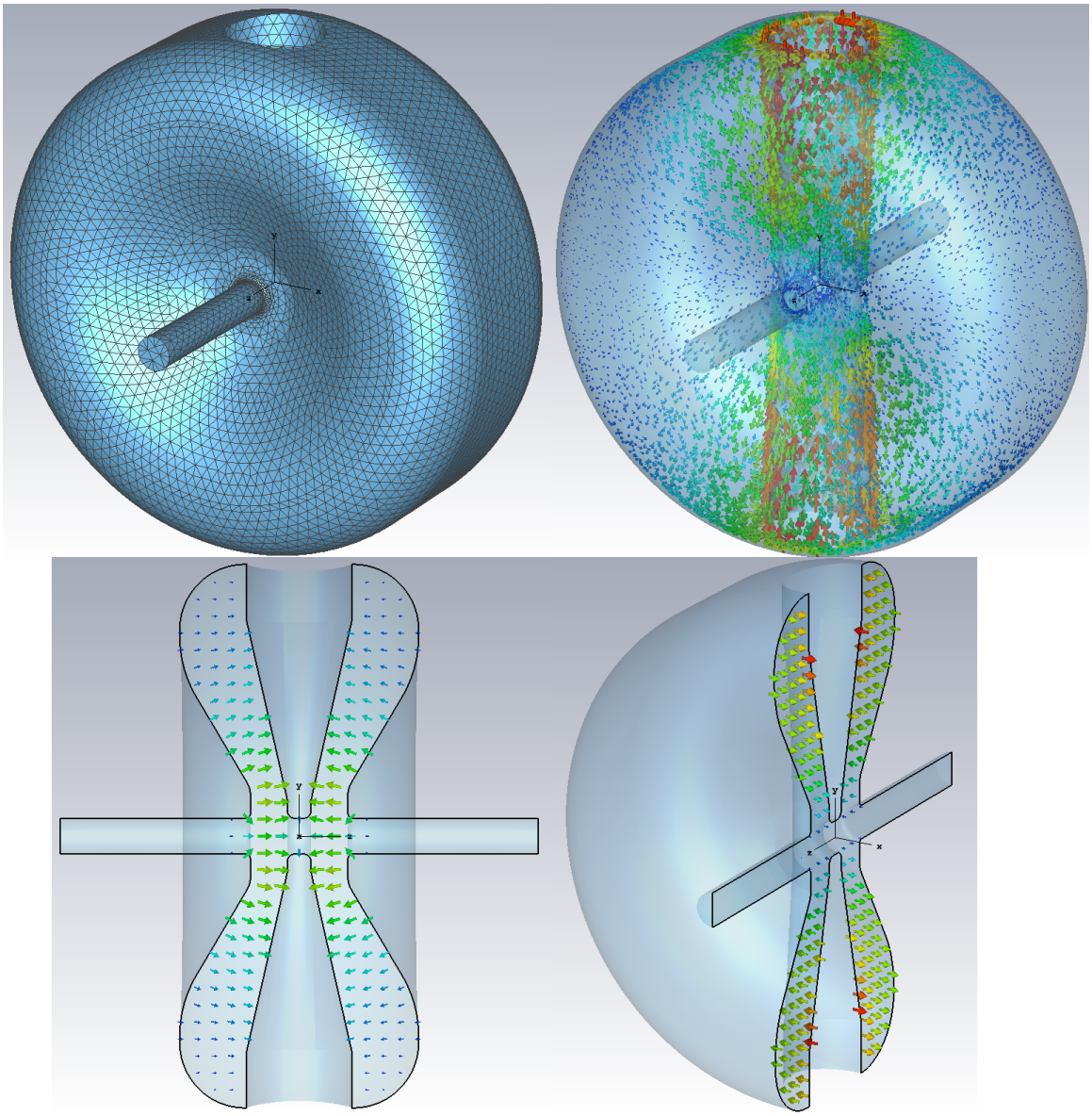

Figure D.3. Detail of medium-beta cavity in CST. Top-left: 254,633 tetrahedrons mesh. Top-right: Peak surface currents, occurring at $\frac{n\pi}{2}$ phase. The resonant frequency is 321.11 MHz and the maximum surface current on the cavity is 25 kA/m (red, near the top and bottom). Bottom-left: yz plane cutaway showing the peak electric fields, occurring at $n\pi$ phase. Bottom-right: yz plane cutaway showing the peak H-fields, occurring at $\frac{n\pi}{2}$ phase.

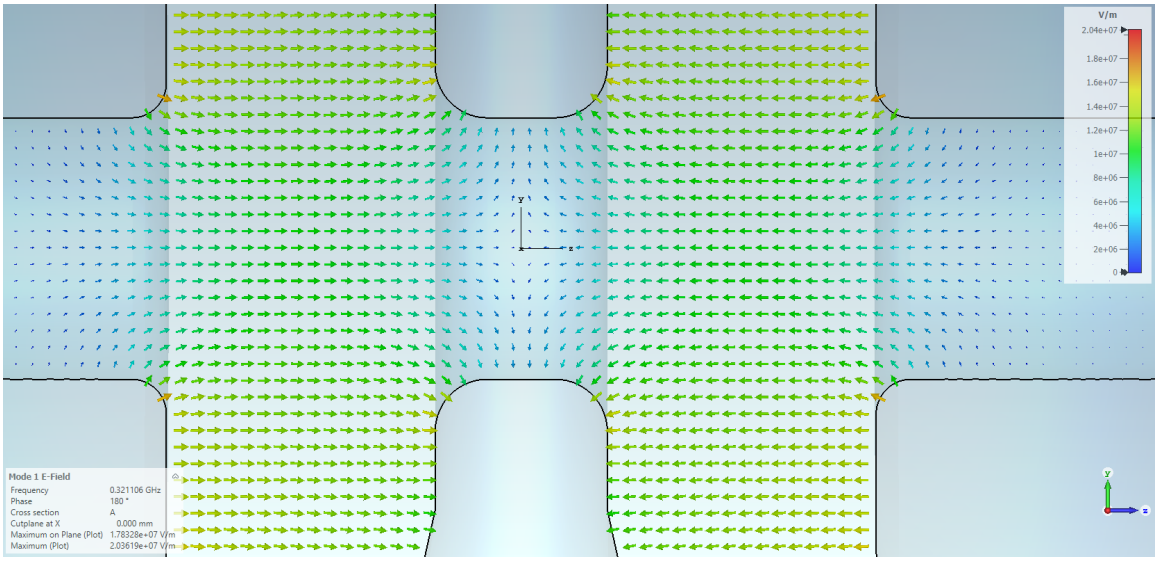

Figure D.4. Medium-beta cavity close-up of electric fields at peaks on yz plane. The maximum electric field on the cavity is 20.4 MV/m (occurs outside of the depicted plane).

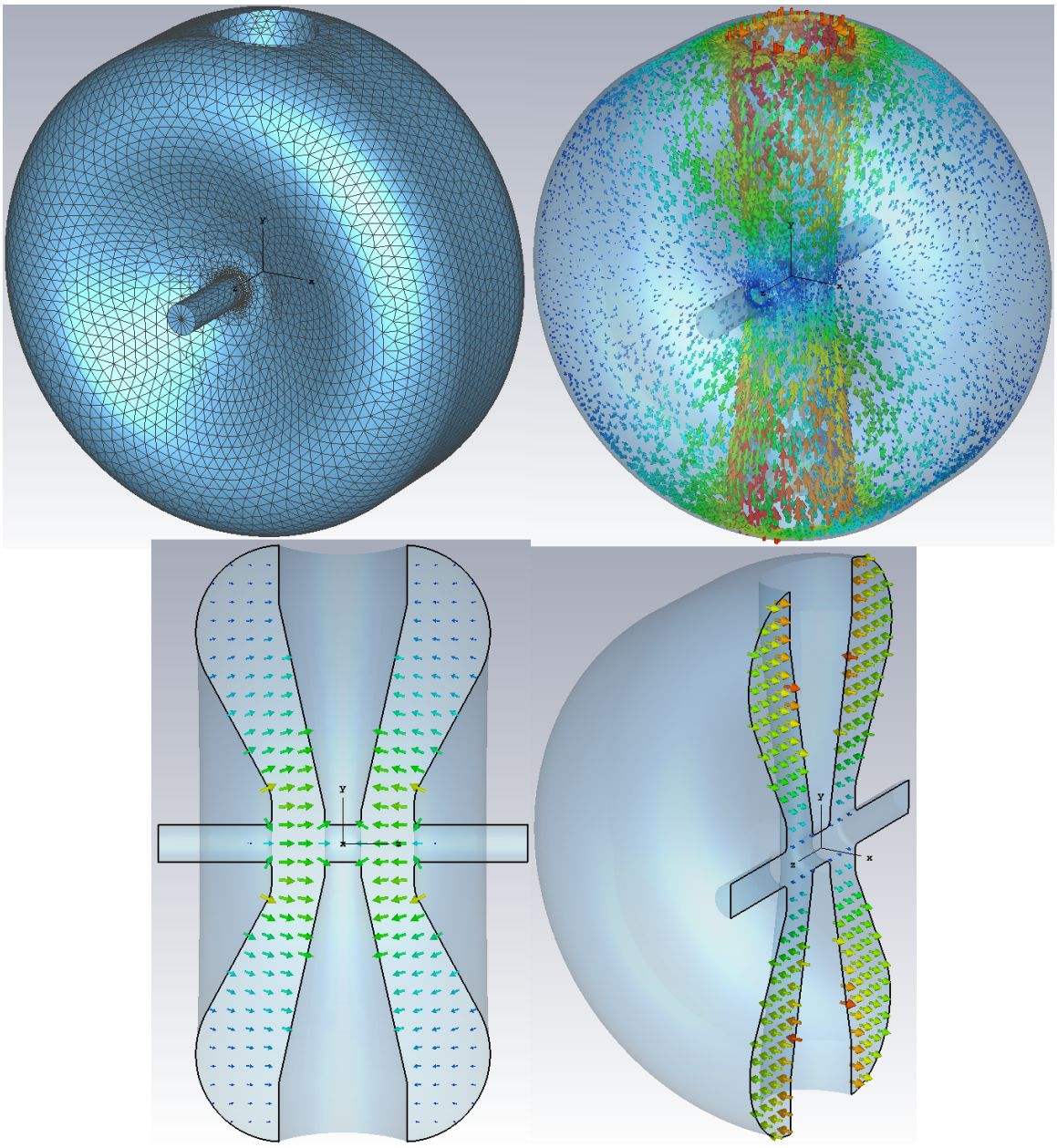

Figure D.5. Detail of high-beta cavity in CST. Top-left: 297,360 tetrahedrons mesh. Top-right: Peak surface currents, occurring at $\frac{n\pi}{2}$ phase. The resonant frequency is 325.052 MHz and the maximum surface current on the cavity is 21 kA/m (red, near the top and bottom). Bottom-left: yz plane cutaway showing the peak electric fields, occurring at $n\pi$ phase. Bottom-right: yz plane cutaway showing the peak H-fields, occurring at $\frac{n\pi}{2}$ phase.

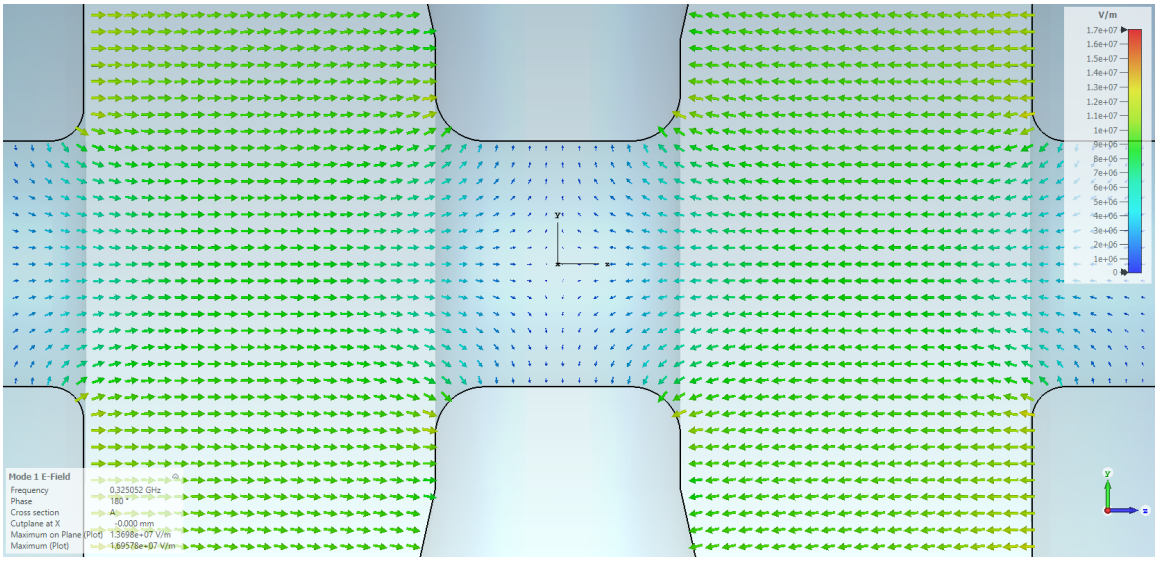

Figure D.6. High-beta cavity close-up of electric fields at peaks on yz plane. The maximum electric field on the cavity is 17.0 MV/m (occurs outside of the depicted plane).

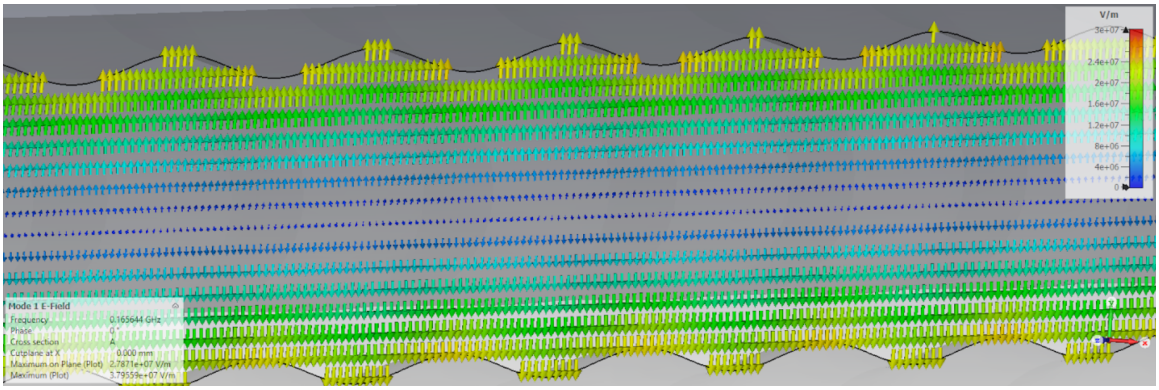

Figure D.7. Electric fields on the xy plane at phase zero in the high-frequency simulation (at 165.644 MHz) at cells near the exit.

APPENDIX E

TRACK.DAT FILE FOR CAVITY ENERGY GAIN SIMULATION

```
&TRAN

 Win = 1.300D06 ![eV/u]
 freqb = 162.5D06,part = 0.995

 nqtot=1
 qq=1
 amass= 2.0135
 npat= 10000
 current=0.0

 Qdesign=1,Adesign=2.0135, db_b=0.00001,df_4D=180.

 epsnx = 0.001,alfax = 0.590405,betax = 3.753289 ![cm*mrad] , [unitless]
     [cm/rad]
 epsny = 0.001,alfay = 0.590405,betay = 3.753289
 epsnz = 0.001,alfaz = 0,betaz = 1 ![deg*%] ,[unitless] , [deg/%]

 phmax=90., dwwmax=1.0

 dWWacc=1.0
 x00=0., xp00=0., y00=0., yp00=0.,
 ph00=-0., dww00=0.,phi0=-0.

&END

&INDEX

 NRZ=1, igraph=1, iaccep=0, iflag_dis=1, iflag2D=0, iflag_qq=1, !
    iflag_dis=0 for continuous beam
 iflag_rms=0, iint=100, nstep_cav=50
 iflag_env=1, iflag_cav=1, iflag_ell=1, iflag_fenv=1
```

```
 iflag_halo=0, iflag_lev=0, isrf=100, iflag_bc=1
 iread_dis=0, iwrite_dis=0, iflag_corr=0, iflag_match=0, iwrite_step=1 !
     will output step.out for each step

&END

&MATCH

 match_typ=1, fit_typ=1, fit_opt=1, min_opt=1, man_max=1000, fit_bnd=1
 bnd_fac=10., fit_err=.01

&END
```

APPENDIX F

BETA CURVES OF INDIVIDUAL CAVITIES

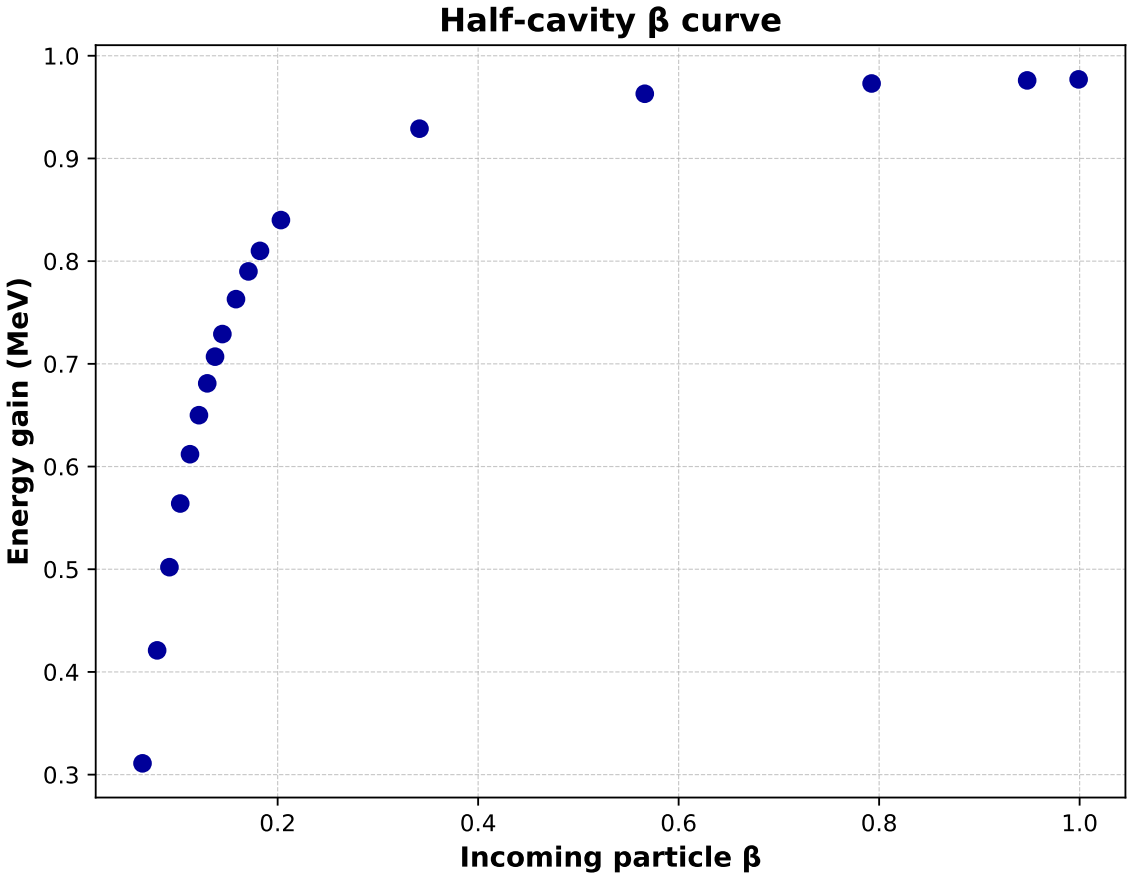

Figure F.1. Beta curve for the first half of a single-spoke cavity. It can be seen that any increase in the particle's incoming speed, above a certain point, will always result in a greater energy gain from the cavity.

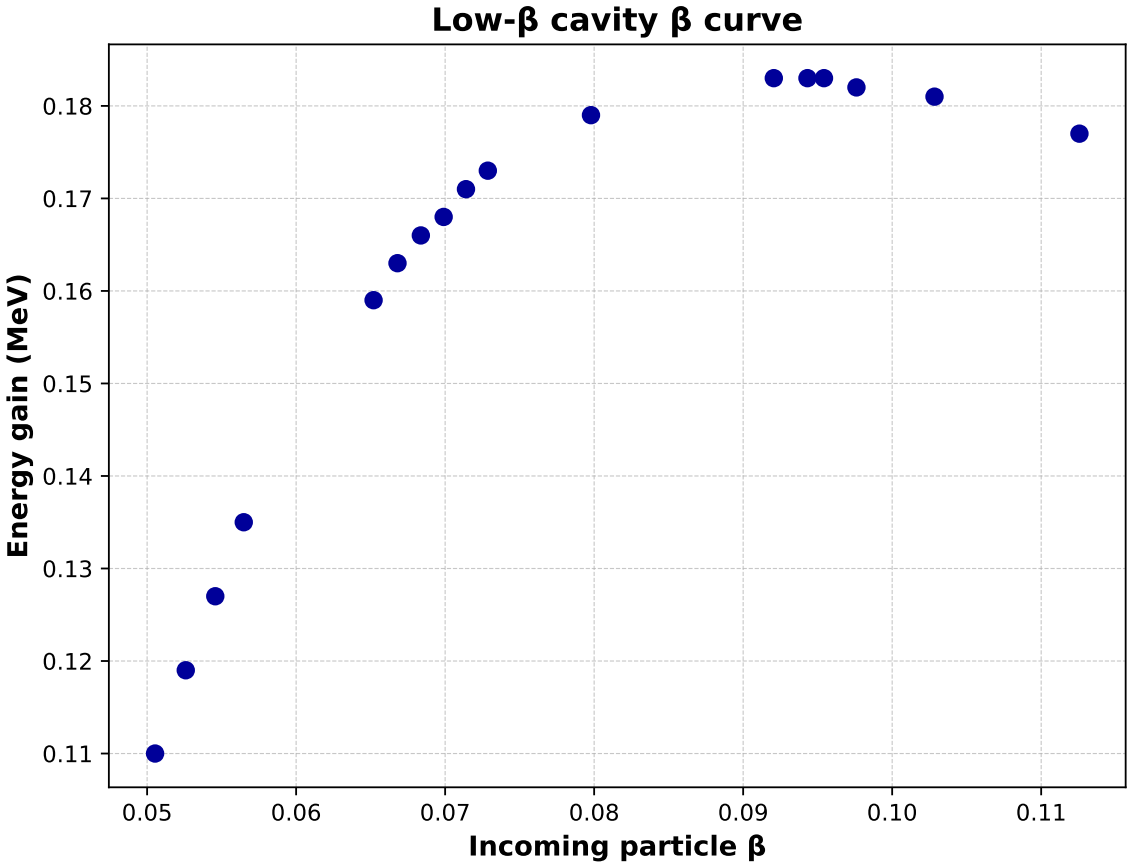

Figure F.2. Beta curve for the low-beta cavity, the first geometry of cavity in the accelerating section. The peak efficiency is around $\beta = 0.094$.

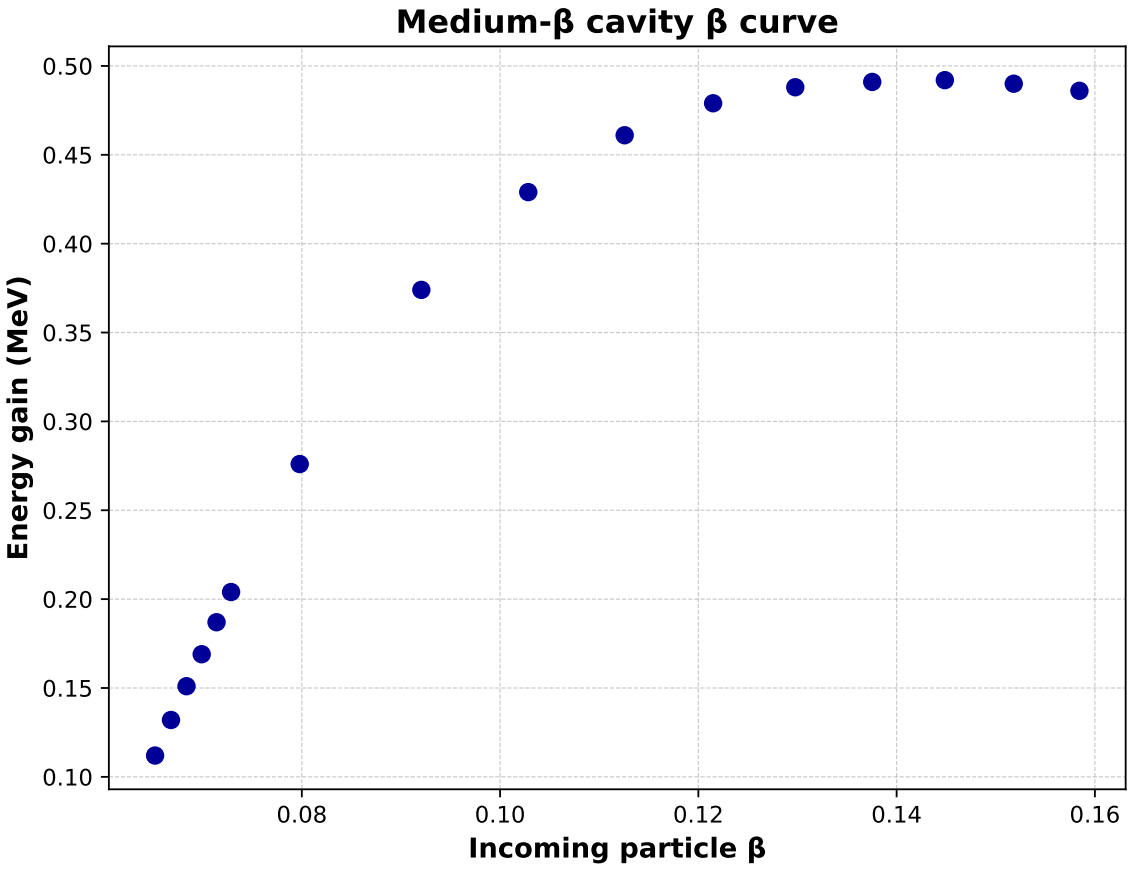

Figure F.3. Beta curve for the medium-beta cavity, the second geometry of cavity in the accelerating section. The peak efficiency is around $\beta = 0.145$.

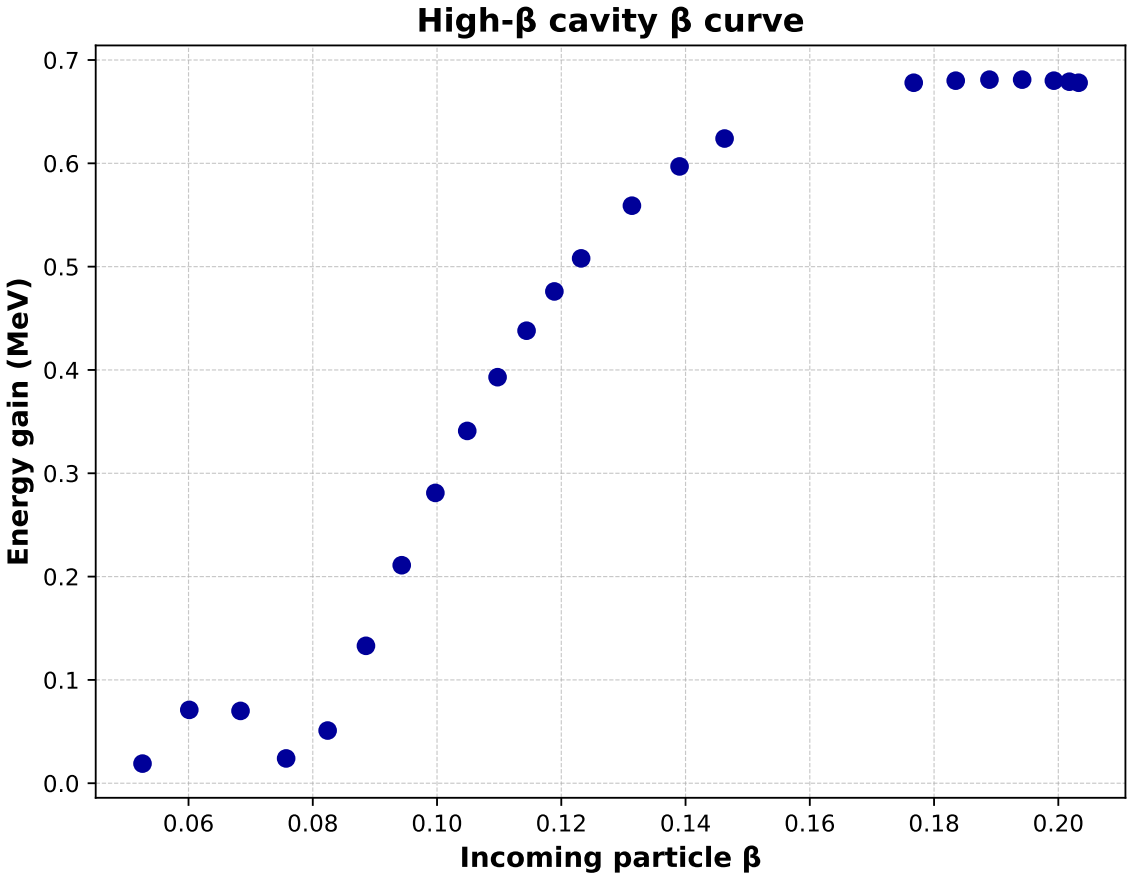

Figure F.4. Beta curve for the high-beta cavity, the third and final geometry of cavity in the accelerating section. The peak efficiency is around $\beta = 0.189$.

BIBLIOGRAPHY

[1] Y. J. et al., "High-current deuteron accelerator for neutron production," in *Proc. 15th International Particle Accelerator Conference*, no. 15 in IPAC'24 - 15th International Particle Accelerator Conference, Nashville, Tennessee, pp. 1071–1073, JACoW Publishing, Geneva, Switzerland, May 2024.

[2] E. López-Melero, F. García-Infantes, F. Arias de Saavedra, L. Fernández-Maza, I. Porras, A. Roldán, and J. Praena, "Study of the production of radioisotopes at IFMIF-DONES: ^{177}Lu with deuterons," *Radiation Physics and Chemistry*, vol. 220, p. 111687, 2024.

[3] P. Ostroumov, Z. Conway, M. Kelly, A. Kolomiets, S. Kutsaev, B. Mustapha, and J. Rodnizki, "SARAF phase II p/d 40 MeV linac design studies," *Proceedings of LINAC2012, Tel-Aviv, Israel*, 2012.

[4] T. P. Wangler, *RF Linear Accelerators*, pp. 232–248. Weinheim, Germany: Wiley-VCH Verlag, 2 ed., Jan. 2008.

[5] I. M. Kapchinskii and V. A. Teplyakov, "A linear ion accelerator with spatially uniform hard focusing," *Prib. Tekh. Eksp.*, vol. 1970, no. 2, pp. 19–22, 1970.

[6] K. R. Crandall and T. P. Wangler, "PARMTEQ: A beam-dynamics code fo the RFQ linear accelerator," *AIP Conf. Proc.*, vol. 177, pp. 22–28, 1988.

[7] A. A. Kolomiets et al., "The RFQ design software DesRFQ." ITEP/ANL Technical Note, 2005.

[8] O. Cakir, E. Celebi, H. Cetinkaya, H. Kolenoglu, G. Turemen, Z. Uysal, and G. Unel, "Demircipro's tools for completing the linac: Ion source and lebt line," 2021.

[9] R. Duperrier, *RFQ Designer Release 0.7*. CEA/DACM. `https://www.dacm-logiciels.fr/rfqdesigner`.

[10] R. Duperrier, *Toutatis Release 2.0*. CEA/DACM. `https://www.dacm-logiciels.fr/toutatis`.

[11] R. Duperrier, "Toutatis: A radio frequency quadrupole code," *Phys. Rev. ST Accel. Beams*, vol. 3, p. 124201, Dec 2000.

[12] T. P. Wangler, *RF Linear Accelerators*, pp. 386–389. Weinheim, Germany: Wiley-VCH Verlag, 2 ed., Jan. 2008.

[13] Dassault Systèmes Simulia, "CST Studio Suite," 2022. `https://www.3ds.com/products/simulia/cst-studio-suite`.

[14] B. Mustapha, A. A. Kolomiets, and P. N. Ostroumov, "Full three-dimensional approach to the design and simulation of a radio-frequency quadrupole," *Phys. Rev. ST Accel. Beams*, vol. 16, p. 120101, Dec 2013.

[15] T. P. Wangler, *RF Linear Accelerators*, pp. 249–251. Weinheim, Germany: Wiley-VCH Verlag, 2 ed., Jan. 2008.

[16] M. K. Pal, R. Gaur, and V. Kumar, "Electromagnetic design of 325 MHz superconducting single-spoke resonators for Indian Facility for Spallation Research," *Pramana*, vol. 96, June 2022.

[17] T. P. Wangler, *RF Linear Accelerators*, pp. 32–44. Weinheim, Germany: Wiley-VCH Verlag, 2 ed., Jan. 2008.

[18] P. Ostroumov, V. Aseev, and B. Mustapha, *TRACK—a Code for Beam Dynamics Simulation in Accelerators and Transport Lines with 3D Electric and Magnetic Fields.* Argonne National Laboratory. `https://www.phy.anl.gov/atlas/TRACK/Copyright/copyright.txt`.